University of South Florida

DIGITAL COMMONS
@ UNIVERSITY OF SOUTH FLORIDA

Digital Commons @ University of South Florida

USF Tampa Graduate Theses and Dissertations

USF Graduate Theses and Dissertations

January 2012

Model and Validation of Static and Dynamic Behavior of Passive Diamagnetic Levitation for Energy Harvesting

Chamila Shyamalee Siyambalapitiya
University of South Florida, csiyamba@mail.usf.edu

Follow this and additional works at: https://digitalcommons.usf.edu/etd

 Part of the Electrical and Computer Engineering Commons, and the Mechanical Engineering Commons

Scholar Commons Citation

Siyambalapitiya, Chamila Shyamalee, "Model and Validation of Static and Dynamic Behavior of Passive Diamagnetic Levitation for Energy Harvesting" (2012). *USF Tampa Graduate Theses and Dissertations.*
https://digitalcommons.usf.edu/etd/4406

This Dissertation is brought to you for free and open access by the USF Graduate Theses and Dissertations at Digital Commons @ University of South Florida. It has been accepted for inclusion in USF Tampa Graduate Theses and Dissertations by an authorized administrator of Digital Commons @ University of South Florida. For more information, please contact digitalcommons@usf.edu.

Model and Validation of Static and Dynamic Behavior of

Passive Diamagnetic Levitation for Energy Harvesting

by

Chamila S. Siyambalapitiya

A dissertation submitted in partial fulfillment
of the requirements for the degree of
Doctor of Philosophy
Department of Electrical Engineering
College of Engineering
University of South Florida

Co-Major Professor: Sanjukta Bhanja, Ph.D.
Co-Major Professor: Aurelio Somà, Ph.D.
Timothy J. Fawcett, Ph.D.
Wilfrido Moreno, Ph.D.
Paris Wiley, Ph.D.

Date of Approval:
November 14, 2012

Keywords: Magnetic Levitation, NdFeB, Pyrolytic Graphite, Resonator, COMSOL

Copyright © 2012, Chamila S. Siyambalapitiya

DEDICATION

I dedicate this dissertation to my grandmother, mother and aunts who loved and supported me though out my life and believe in the importance of girls' education.

ACKNOWLEDGMENTS

This dissertation is the result of years of work whereby I have been accompanied and supported by many people. I would like to convey my heartfelt gratitude to my co-major professors, Dr. Aurelio Soma` who sponsored and guided me to initiate this research in Italy, and Dr. Sanjukta Bhanja who took me under her wing and supported me to continue my passion. Without their support, this work would have been only a dream. I would like to express my appreciation to my committee members, Dr. Paris Wiley, Dr. Timothy Fawcett and Dr. Wilfrido Moreno each of whom were always there for me in my difficult time helping in every possible way and are the corner stones of the work. I would like to extend thanks to Dr. Giorgio Depasquale for his invaluable support.

I specially would like to thank Dr. Hyde, Dr. Kramer, Dr. Fefilatyev, Matthew Shreve, Johan Sosa and James Lyon for their support throughout these years and specially for being true friends. Also I would like to thank my wonderful friends Kumi, Ken, Natasha, Natalia and friends from University of Peradeniya for their encouraging words and being there during difficult times. Also I would like to acknowledge the support of my lab mates and the EE department. Thanks and gratitude goes to Dr. Hari Srikanth, Dr. Shekhar Bhansali and their groups for equipment support.

I pleasantly remember with utmost gratitude all my teachers from grade school till today throughout this journey. It is a pleasant aspect that I have now the opportunity to express my gratitude for all of them. Lastly, but mostly I would like to thank my family and relatives who gave unlimited love, support and care throughout my life.

TABLE OF CONTENTS

LIST OF TABLES iv

LIST OF FIGURES vi

ABSTRACT xi

CHAPTER 1: INTRODUCTION 1
- 1.1 Motivation 1
- 1.2 Objective 4
- 1.3 Contribution 5
  - 1.3.1 Experimental Investigation of Static Behavior of the Levitating System 5
  - 1.3.2 Resonance Frequency Characteristics of Diamagnetic Levitating Systems 6
  - 1.3.3 Development of a FEM Model for Design and Optimization of the Magnetic Levitation Devices 7
  - 1.3.4 Utilization in Energy Harvesters 7
- 1.4 Organization of this Dissertation 8

CHAPTER 2: LITERATURE REVIEW 10
- 2.1 History and Milestones of Magnetic Levitation 10
- 2.2 Different Methods of Magnetic Levitation 12
  - 2.2.1 Electromagnetic Levitation 13
  - 2.2.2 Superconductor Levitation 14
  - 2.2.3 Permanent Magnet Levitation 15
    - 2.2.3.1 Permanent Magnetically Levitated MEMS Devices 16
- 2.3 Levitation Advantages 19
- 2.4 Energy Harvesters 20
  - 2.4.1 Piezoelectric 21
  - 2.4.2 Electromagnetic 22
  - 2.4.3 Electrostatic 22

CHAPTER 3: THEORETICAL BACKGROUND 24
- 3.1 Important Definitions 24
- 3.2 Quantum Interpretation of Magnetism 26
- 3.3 Magnetic Hysteresis Curve 27
- 3.4 Magnetic Material 30
- 3.5 Diamagnetism 31
  - 3.5.1 Pyrolytic Graphite 32

3.6 Permanent Magnets 32
3.7 Mathematical Model for Calculating the Magnetic Field Space above Permanent Magnets 34
3.8 Magnetic Levitation Phenomena 35
3.8.1 Analytical Models for Static Levitation 36
3.8.1.1 Magnetic Force from Current Model 38
3.8.1.2 Magnetic Force from Charge Model 39
3.8.2 The Analytical Model for the Dynamic Behavior 39

CHAPTER 4: EXPERIMENTAL DATA 42
4.1 Static and Dynamic Experiment Organization 42
4.2 Experiment Setup 44
4.3 Static Behavior of the Diamagnetic Levitation System 46
4.4 Dynamic Levitating System 50
4.5 System Consisting of Fixed Thickness (t) and Variable Length (l) of Pyrolytic Graphite Proof Masses 53
4.6 System Consisting of Fixed Length and Variable Thicknesses of Pyrolytic Graphite Proof Masses 60
4.7 Qualitative Study on 5mm Magnets 63
4.8 The Study of Experimentally Derived Motion-dependent Magnetic Forces 64

CHAPTER 5: FINITE ELEMENT MODEL FOR PERMANENT MAGNETS 73
5.1 Finite Element Method (FEM) 73
5.2 COMSOL AC/DC Module 74
5.3 One Magnet Simulation and Verification of the Model 74
5.3.1 Partial Differential Equations (PDEs) 75
5.3.2 Geometry 75
5.3.3 Domain Properties 76
5.3.4 Boundary Conditions 78
5.4 Simulation Model Results for One Magnet 81
5.4.1 Comparison of Simulation and Measured Results 83
5.5 μ_{xx} and μ_{yy} Dependance on B_z Magnetic Flux Distribution 85
5.6 Simulation and Verification of the ONP Model 88
5.6.1 Model Construction 88
5.6.2 Simulation Results of ONP Configured Four Magnets 89
5.7 Magnetic Flux Density Measurement 90
5.8 Comparison with Experimental Results 92

CHAPTER 6: STATIC LEVITATION MODEL AND MAGNETO-MECHANICAL COUPLING 94
6.1 M-H Measurements for Pyrolytic Graphite 94
6.2 Static Levitation Model 96
6.3 Magnetic Force Simulation 100
6.3.1 Static Levitation Height and Maximum Levitable Size Obtained from Simulation 104
6.3.2 Magnetic Potential Simulations 107

CHAPTER 7: APPLICATIONS 110
7.1 Energy Harvester 110
7.1.1 Electrostatic Harvester 112
7.1.2 Piezoelectric and Capacitive Hybrid Harvester 114
7.2 Other Applications 115
7.2.1 Lab on a Chip 115
7.2.2 Carbon Nano Tube Aligning and Graphene Devices 117

CHAPTER 8: CONCLUSIONS 118
8.1 Summary 118
8.2 Mathematical Relation for Static and Dynamic Levitation 119
8.3 Experimental Observation, Measurements and Derivation 119
8.4 Finite Element Modeling 121

REFERENCES 123

APPENDICES 131
Appendix A: List of Symbols and Acronyms 132
Appendix B: Maglev Trains 134
Appendix C: Sintered Magnets 135
Appendix D: Bonded Magnets 136
Appendix E: Copyright and Permissions 137
E1: Permissions for Figure 2.1 137

LIST OF TABLES

Table 2.1 Milestones of diamagnetic levitation. 12

Table 2.2 Review of the current *state of the art*..... 18

Table 2.3 Advantage and disadvantage of levitation using the permanent magnet method. 19

Table 2.4 Advantages and disadvantages of levitating and attached systems. 20

Table 2.5 Acceleration and resonance frequency of fundamental vibration mode for various sources. 21

Table 3.1 Definition and notation of some magnetic parameters. 25

Table 3.2 The cgs and SI units of some magnetic parameters and their conversions. 25

Table 4.1 Properties of the magnetic levitation system. 44

Table 4.2 Resonance frequency and stiffness of graphite proof masses (l = 9-20 mm). 58

Table 4.3 Resonance frequency and stiffness of graphite proof masses (l =9-14 mm). 58

Table 4.4 Resonance frequency and stiffness of graphite proof masses (t = 0.3-1.0 mm)..... 62

Table 4.5 Comparison between ONP systems of two different magnet sizes. 63

Table 4.6 Equilibrium levitation height and configurations of graphite proof masses on ONP nine magnets system. 64

Table 4.7 Calculation of force F_{tot} -F_g by analytical equation for l = 15 mm proof mass at f = 15 Hz. 67

Table 5.1 Error analysis of the B_z between simulation with nominal B_r and measurement data of *Magnet 1* and *Magnet 2* samples. 85

Table 6.1 Values of χ for some diamagnetic materials 95

Table 6.2 The model parameters used to produce Figure 6.3 and Figure 6.4. 98

Table 6.3 Measured air gaps of proof masses with various lengths and same thickness 101

Table 6.4 Measured air gaps of proof masses with various thickness and same length. 101

Table 6.5 Comparison of measured and simulated air gap at static equilibrium levitation obtained for N =1, 2 and 3 layers of magnets 106

Table 7.1 Comparison of f_0 and k of proof masses with varied lengths when utilized in cantilever form and magnetic levitating (maglev) form 112

Table 7.2 Comparison of f_0 and k of proof-masses with varied thicknesses when utilized in cantilever form and magnetic levitating form 112

LIST OF FIGURES

Figure 2.1 Different types of magnetic levitation. 13

Figure 3.1 Magnetism formation in a free atom. 26

Figure 3.2 ***M*** vs. ***H*** and ***B*** vs. ***H*** curves. 27

Figure 3.3 Single DOF model of levitating magnetic suspension 39

Figure 4.1 Graphical representation of the two systems that test both the static and dynamic behavior of the levitating systems. 43

Figure 4.2 (a) Experimental set up for dynamic measurements of the levitating system 45

Figure 4.3 Levitation heights(Solid lines) and air gap(dotted lines) for various thicknesses of the proof mass and with one (●), two (■) and three (▲) layers of NdFeB permanent magnets. 47

Figure 4.4 Levitating height (Solid lines) and air gap (dotted lines) of graphite vs. variable side lengths for one (●), two (■) and three (▲) layers of NdFeB permanent magnets. 48

Figure 4.5 Levitation height vs. length of the PG mass for N=1 (●) and N=2 (■) layers of NdFeB permanent magnets. 49

Figure 4.6 Forces acting on the levitating system during vibration. 51

Figure 4.7 Time domain displacement of base and proof mass (9mm) for 13 Hz driving frequency. 52

Figure 4.8 Time domain displacement of the base and the proof mass (9 mm) for 17.4 Hz driving frequency (note that the resonance frequency for a 9 mm proof mass is also 17.4 Hz). 53

Figure 4.9 Frequency domain amplitude curves for pyrolytic graphite with variable length (l) under the influence of a single layer of magnets (N =1). 54

Figure 4.10 Frequency domain amplitude curves for pyrolytic graphite with variable length (l) under the influence of two layers of magnets (N = 2). 54

Figure 4.11 Frequency domain amplitude curves for pyrolytic graphite with variable length (l) under the influence of three layers of magnets (N = 3) 55

Figure 4.12 Amplitude curves for 15 mm Pyrolytic graphite under the influence of single (N=1), double (N=2) and triple (N=3) layers of magnets. 57

Figure 4.13 The 15 mm proof mass position on the ONP magnet arrangement. 57

Figure 4.14 Resonance frequency (solid line) and spring value variation (dotted lines) for one (●), two (■) and three (▲) layers of NdFeB permanent magnets. 59

Figure 4.15 Damping ratio values obtained for vibration of different graphite size for influence of one (●), two (■) and three (▲) layers of NdFeB permanent magnets. 59

Figure 4.16 Frequency domain amplitude curves for pyrolytic graphite with various thicknesses under the influence of a single magnet layer (N=1). 60

Figure 4.17 Frequency domain amplitude curves for pyrolytic graphite with various thicknesses under the influence of two layers of magnets (N=2). 61

Figure 4.18 Frequency domain amplitude curves for pyrolytic graphite with various thicknesses under the influence of three layers of magnets (N=3). 61

Figure 4.19 Resonance frequency (solid lines) and spring value variation (dotted lines) for one (●), two (■) and three (▲) layers of NdFeB permanent magnets. 62

Figure 4.20 Frequency response graph of damped linear oscillator. 66

Figure 4.21 The displacement-time graph of a 15 mm pyrolytic graphite proof mass at f = 10 Hz and 15 Hz driving frequencies reconstructed by analytical equations using experimental parameters. 68

Figure 4.22 Frequency response of a 15 mm proof mass obtained by analytical method and experimental method. 69

Figure 4.23 Force ($F_{tot} - F_g$) variation with frequency for l = 9 mm (top) and l = 13 mm (bottom) proof masses. 70

Figure 4.24 Force ($F_{tot} - F_g$) variation with frequency for l = 15 mm (top) and l = 19 mm (bottom) proof masses. 71

Figure 4.25 Force variation with frequency for l = 9, 13, 15 and 19 mm. 72

Figure 5.1 The 2D representation of the model geometry: 1) NdFeB magnet, 2) Measurement air box, 3) Inner air sphere and 4) Outer air sphere. 76

Figure 5.2 Comparison between the results of the model with infinite elements (*inf*) and without infinite elements (*noninf*). 80

Figure 5.3 2D representation of the z-component of the magnetic flux density (B_z) distribution of the Grade 45 NdFeB magnet at 0.6 mm above the surface of the magnet. 82

Figure 5.4 Simulated results of the distribution of B_z along the line *AB* at *d* distance above the surface of the magnet. 82

Figure 5.5 Measured (markers) and simulated (solid lines) distributions of B_z along *AB* at 0.6 mm above the surface of the magnet. 83

Figure 5.6 Measured (markers) and simulated (solid lines) distributions of B_z along *CD* (x at y = 1 mm) at 0.6 mm above the surface of the magnet. 84

Figure 5.7 Measured (markers) and simulated (solid lines) distribution B_z along *EF* (along y, at x = 1 mm) at 0.6 mm above the surface of the magnet. 84

Figure 5.8 Simulated B_z for various μ_{xx} and μ_{yy}, along the line *AB* at *d* distance (d = 0.6, 2, 3, 5, 8 mm) above the surface of the magnet. 87

Figure 5.9 Simulated B_z for various μ_{xx} and μ_{yy}, along the line *CD* at *d* distance (d = 0.6, 2, 3, 5, 8 mm) above the surface of the magnet. 87

Figure 5.10 The four magnet model consists of 1) Four NdFeB magnets, 2) Measurement air box, 3) Inner air sphere and 4) Outer air sphere. 88

Figure 5.11 B_z distribution at d=0.6 mm 89

Figure 5.12 Simulated results of the distribution of B_z along the line *AB* at *d* distance above the surface of the magnets. 90

Figure 5.13 Experimental setup for magnetic flux density measurements. 91

Figure 5.14 Magnetic flux surface plots obtained from measurements. 91

Figure 5.15 Measured (markers) and simulated (solid lines) distributions of B_z along the diagonal line of the ONP configured four magnets at d mm above the surface of the magnets. 92

Figure 5.16 Simulated results of the distribution of B_z along the diagonal line at d=0.6mm distance above the surface of the magnets for N = 1, 2 and 3 layers of magnets arranged in ONP configuration. 93

Figure 6.1 M-H measurements of the pyrolytic graphite: Perpendicular axis (○) and parallel axis (-). 96

Figure 6.2 The model geometry for the levitation model: the model consist of, 1) Two layers of NdFeB magnets, 2) Measurement air box, 3) Pyrolytic graphite, 4) Inner air sphere and 5) Outer air sphere. 97

Figure 6.3 *z*- component of magnetic flux density, B_z distribution of N=3 layers of magnets at d = 1 mm. 99

Figure 6.4 Induced magnetization, M_z of graphite layer at d = 1 mm distance under the influence of N = 3 layers of magnets. 99

Figure 6.5 Measured and simulated forces (using *current model*) of various t of PG proof masses with influence of N = 1, 2 and 3 layers of magnets in static levitation..... 102

Figure 6.6 Measured and simulated forces (using *current model)* of various l of PG proof masses with influence of N = 1, 2 and 3 layers of magnets in static levitation..... 102

Figure 6.7 Comparison of the forces derived from the *current model* and the *charge model* against the weights of the proof masses..... 104

Figure 6.8 Simulated forces (dotted lines) for graphite masses with t=1 mm and various l (= 4 to 20 mm) at d_a (air gap) distance above the N=1 layer of magnets. 105

Figure 6.9 Simulated air gaps of various length of proof masses at static equilibrium levitation (N =1, 2 and 3 layers)..... 107

Figure 6.10 Simulation B_z^2 at d=0.6mm above the magnets for ONP configured N=1 layer of magnets. 108

Figure 6.11 Simulated potential energy for l=10 mm, t= 1.0 mm graphite proof mass at d_a= .4952mm (air gap) by rotating angle from 0 to 90 under N=1 magnet layer influence. 109

Figure 6.12 Simulated x direction torque of l=10 mm, t= 1.0 mm graphite proof mass at d =0.4952 mm (air gap) by rotating angle from 0 to 90 under N=1 magnet layer influence. 109

Figure 7.1 Magnetically suspended electret capacitive energy harvester based on out of plane kinematic strategy. 113

Figure 7.2 Hybrid harvester..... 115

ABSTRACT

This dissertation reports the investigation conducted on the static and dynamic behavior of the passive diamagnetic levitation systems.

Attachment of a device to a substrate hinders the optimum performance ability of vibrating devices by altering the dynamic behavior of the moving part whilst introducing higher overall stiffness. The significance of this effect is prominent especially in vibration based energy harvesters as higher stiffness elevates the resonance frequency of the system, making it difficult to tune into ambient low frequencies. Other advantages of the proposed method are given by the removal of mechanical bending elements, which are often the source of energy dissipation through thermo-elastic damping and affects device reliability and durability. In this research, diamagnetically levitated resonators that can be utilized in energy harvesting were proposed and investigated as a possible solution to overcome these problems. Permanent magnets in an *opposite neighboring poles* (ONP) configuration were used to provide the magnetic field required for levitation. Pyrolytic graphite (PG), which is the known highest diamagnetic material, serves as the levitating proof mass.

Experimental results show that the static levitation height has a linear dependence on the thickness and a nonlinear dependence on the area of the levitating proof mass that can be approximated to a third order polynomial equation. Also, the study proved that a thinner proof mass provides a higher air gap while length of the proof mass beyond a certain value (l >10 mm for the experimental system considered in this dissertation) has

no significant effect on increasing the air gap. It was also observed that levitation can slightly increase by attaching magnets to a sheet of steel (ferromagnetic material).

To the best of my knowledge, this dissertation is the first to address the parameterized studies in the dynamics of diamagnetic levitated objects by permanent magnets. Measurements performed on a diamagnetic levitating prototype system show that the resonance frequencies are lowered by approximately 3- 4 orders of magnitude in levitated systems compared to the attached systems demonstrating the feasibility of using levitating techniques for micro to meso scale energy harvester applications. Also, there is a significant dissimilarity observed in this study compared to the mechanically attached systems: The resonance frequency has a dependence on magnetic field strength, and is shifting towards lower values when increasing the strength of the magnetic field. This indicates that the virtual spring of a levitated proof mass is not a constant and therefore, the resonance frequency of the diamagnetic levitated systems is able to be fine-tuned by varying the magnetic field.

Finite Element Method (FEM) models were developed using COMSOL software that can simulate 3D magnetic flux formation of an array of permanent magnets and the diamagnetic levitation. The appropriate magnetic force equation from the two force equations that exist in the literature was established for the static levitation with the help of experimental and simulation results. Moreover, these models are able to provide the magnetic force exerted on diamagnetic objects at different heights, stable levitation height and position and also an indication of the maximum stably levitated size of the diamagnetic material.

Future endeavor of this study is to realize the diamagnetic levitation in energy harvesters. The results obtained from this research will not be limited to harvester applications but will also be beneficial to other diamagnetic levitation related systems, as these parameters are fundamental and necessary for the foundation of the research in the field of interest.

CHAPTER 1

INTRODUCTION

1.1 Motivation

The technological advancement towards lower power consumption in current integrated circuits has opened up the doors to employing systems powered by harvesting ambient energy. Self-powered systems are particularly interesting in areas such as automotive, industrial, building and home automation, environment monitoring, military and aerospace, and medical and consumer electronics. Vital applications can be found in places that are difficult for electrical wiring, hard to access, or are difficult to replacing batteries such as powering of the densely populated sensor nodes in a network, implantable devices, structural health monitoring systems and devices placed in remote areas and war zones are some examples. Additionally, the daily life of an average person today is highly dependable on wireless hand-held or portable devices and the requirement of a bulky battery or wired power supply to power these devices is a cumbersome constraint, reducing the convenience in portability. These circumstances have encouraged researchers to exploit renewable energy sources.

Vibration based devices are a major area of interest in harvesting energy from the ambient environment due to their ability to integrate with electronic devices. A major obstacle the vibration-based energy harvesting field faces today is lowering the frequency of the harvesting system down to the range of environmental natural vibrations while reducing the device size. Researchers are working on Micro-electro-mechanical systems

(MEMS) approaches for energy harvesting and are appealing for most applications due to smaller size. However, environmental vibrations are in the range of 1-500 Hz while resonance frequencies of most MEMS resonators are in the range of above 10 KHz. This has limited the use of MEMS harvesters in practical purposes and the field is still relying on quite large devices for energy harvesting. One reason for the higher resonance frequency of a device is the mechanical attachments. Device attachments to a substrate increase global stiffness, and hence increase the resonance frequency. We suggest magnetic levitation, a contactless method to suspend the vibrating part of the device, as a possible solution for this problem.

Magnetic levitation can be achieved by three principle methods, namely, using 1) electromagnets, 2) permanent magnets and 3) superconductors [Azukizawa 1989, Mann 2009, Simon 2001, Pelrine 1995, Garmire 2007, Arkadiev 1945, Livingston 2011]. Most well-known levitation experiments and applications have been done by electromagnetic (active levitation) methods (e.g. frog levitation [High field magnetic laboratory 2009], Maglev trains [Bonsor 2009], etc.). The attractive part of active levitation is that the user has control over the induced magnetic field, and hence, control of the levitation. However, electromagnetic active levitation consumes massive power, is expensive and requires complex feedback systems. For example, to activate the 'bitter' magnet used in frog levitating experiments consumes 4MW of power and a new system that can create 32 T magnetic fields consumes over 20 MW of power, which is adequate to give electricity to a small town [Berry 1997, Geim 2009]. In this investigation, we focus on passive diamagnetic levitation in which the diamagnetic material is levitated by permanent magnets arranged in an *opposite neighboring poles* (ONP) configuration. In

ONP configuration, each magnet is opposite in polarity to its adjacent. This method was first patented by Pelrine in 1995 [Pelrine 1995]. The benefits of a passive diamagnetic levitation system using permanent magnets lies in minuscule power consumption, room temperature applicability, self-stabilization and ease in miniaturization over its state of the art counterparts.

The possibility of applying a permanent magnetic levitation method is being investigated on MEMS applications such as accelerometers [Garmire 2007], gyroscopes [Damrongsak 2009], biosensors [Cugat 2006] and micro robotics [Caglar 2009, Verma 2004]. In this investigation, we focus on the use of diamagnetic levitation of resonators that has possible applications in energy harvesters. As magnetic levitation using permanent magnets is a relatively new concept to apply in devices, there is plenty of work to be done, relations to be established, and theory to be developed. The featured article published in 2004 by Ronald Pelrine provides worthy insight of the present state of diamagnetic levitation.

> "Diamagnetic levitation is a striking physical phenomenon, one that has been studied for many decades now. Yet surprisingly few people, even scientists and engineers, are familiar with it. One reason is that, with the exception of some kits being sold as scientific novelties, diamagnetic levitation has not yet been exploited commercially—although various possibilities, including useful sensors and frictionless transport systems, have been fashioned in academic and industrial labs. Why did so many decades pass between the first demonstration of diamagnetic levitation in 1939 and the development of useful devices based on this principle? The chief reason is that powerful neodymium–iron magnets, which make diamagnetic levitation quite easy today, were discovered only in the 1980s and didn't become widely available until the 1990s. In that sense, diamagnetic levitation was invented long before its time. The bearing pressure that can currently be obtained is too low for most mechanical applications. However, there is no fundamental reason why the diamagnetism of specially designed materials could not be 10 or even 100 times greater than what's available now. If such substances could be identified and developed, diamagnetic levitation would be instantly catapulted from a little–known curiosity to a major technology". ~Pelrine, American Scientist, 2004.

1.2 Objective

The overall objective of this research is to build the foundations of theory, experiment and finite element modeling to investigate the potential of diamagnetic levitation in energy harvesting application. The parameterized studies are performed using a macro scale prototype to establish parameter dependence on both the static and dynamic behavior of the system. The experimental data is utilized to establish a finite element model that can be employed in diamagnetic levitation device designs and optimization. The essential segments addressed in this doctoral research work are,

(1) Static analysis: The area, the thickness of the diamagnetic material and the magnetic field strength dependence on static levitation.

(2) Dynamic analysis: The frequency response characterization of diamagnetic levitating systems.

(3) Supplementary measurements: Finding the diamagnetic susceptibility (χ) of low cost commercially available pyrolytic graphite by M-H measurements using the *Physical Property Measurement System* (PPMS). Mapping of the magnetic field distribution in the space above the Opposite Neighboring Poles (ONP) configuration.

(4) An experimentally verified COMSOL FEM model for one magnet and an array of magnets in ONP configuration.

(5) An experimentally verified FEM model for diamagnetic levitation. Verification of the magnetic force equation for diamagnetic levitation.

(6) Investigation and evaluation of diamagnetic levitation to utilize in energy harvesters.

1.3 Contribution

This work provides the following contribution to the field of diamagnetic levitation.

1.3.1 Experimental Investigation of Static Behavior of the Levitating System

Static experimental results reveal that the levitation height has a linear dependence on the thickness of the levitating object and a nonlinear dependence on the area of the object that can be approximated to a third order polynomial equation (4.3). Furthermore, when the size of the diamagnetic levitating object increases, the increment of the magnetic force (ΔF_m) equals or exceeds to the increment in its gravitational force (i.e. $\Delta F_m \geq \Delta F_g$). This can be observed by the elevation of the center of mass of the PG. In other words, the levitation height increases or stays at the same value. This is a key finding, as the maximum stable levitable size of the levitating proof mass can be obtained from simulation, with the help of this information (5.9.2).

It was observed that the increasing the size of the proof mass beyond 10 mm (l >10) has no effect on increasing levitating height. Moreover, this study proved that a thinner proof mass should be chosen for longer dynamic range as a higher air gap is given by a thinner proof mass.

It was also observed that the levitation height and the maximum size of the object that can be levitated can be slightly increased by attaching the magnets to a steel plate. Attaching the magnets to a steel base gives the added advantage of easy and secure maneuverability of magnets.

1.3.2 Resonance Frequency Characteristics of Diamagnetic Levitating Systems

Parameterized studies on variable parameters of the ONP levitation system were established on dynamic behavior for the first time to the best of my knowledge. Similarly to mechanically attached systems, the resonance frequency decreases with an increasing floating mass. However, it was observed that the resonance frequency also depends on the magnetic field strength in magnetically levitated systems. It is evident that the virtual spring of a levitated proof mass is not a constant, in contrast to the constant spring seen in mechanically attached systems (4.4). This shows the ability to fine tune the resonance frequency in magnetic levitated system by varying the magnetic field.

The resonance frequencies obtained by levitating proof masses show considerably lower frequencies compared to the attached systems. We observed 3-4 orders of magnitude lower resonance frequency for the levitating proof mass compared to a similar sized cantilever.

This suggests that there is an optimum value for the length ratio between the proof mass and the magnets to achieve the maximum amplitude of vibration of the system. This observation is quite interesting and differs from the mechanically attached system where the frequency depends only on the mass and the spring constant of the system. This result shows that the virtual spring value is a function of the magnetic field in a magnetic levitation system and cannot be considered a constant like in mechanically attached non-magnetic systems.

1.3.3 Development of a FEM Model for Design and Optimization of the Magnetic Levitation Devices

In the literature, diamagnetic levitation experimental results have been compared to FEM models or analytical models results using material parameters that are meaningful but arbitrarily selected for verification purposes; Models have not been verified with experimental data using real material parameters [Barrot, 2008, Chetouani 2007, Garmire 2007]. In this work, we compare experimental results with the model results using real material parameters that were either measured or obtained from appropriate data sheets. This leads us to verify the dipole force model and the equation applicable for diamagnetic levitation systems from the two equations (5.9.1).

A finite element model was developed for NdFeB permanent magnets using COMSOL software and experimentally verified against measurement data (5.3). Using the developed model, magnetic flux in the space above the ONP configuration was simulated and compared against the experimental data (5.6). The influence of both area variation and thickness variation of pyrolytic graphite in static levitation conditions was simulated using COMSOL software and compared against measurements (5.9). The force equation $mg = \nabla(M \cdot B)$ was validated for the static diamagnetic levitation (5.9.1).

1.3.4 Utilization in Energy Harvesters

The research concludes with the investigation of the feasibility of application of diamagnetic levitation in energy harvesters.

Apart from the prior mentioned contributions, we have identified the need to establish in-depth knowledge of magnets and magnetism, and to clarify some concepts in order to understand and utilize magnetic levitation in engineering applications. It is

important to know about permanent magnets and their behavior: the magnetic field distribution, magnetic force and potential well formation that are necessary to identify parameters such as equilibrium position, levitation height and other necessary criteria that will ultimately allow to design and utilize this technology. Part of our goal is to contribute by establishing some of the fundamentals and participate in the development of the magnetic levitation field to utilize it to its highest potential. The levitation phenomenon has promising advantages in applications involving standalone devices as well as integration with existing traditional systems. The outcome of this research will also pave the way for designing other smaller scale systems that would benefit from attachment-free levitation.

1.4 Organization of this Dissertation

This dissertation is organized as follows,

- Chapter 2 provides the related research work done in the field of NdFeB permanent magnets, magnetic levitation, simulation and energy harvesters. Additionally, it provides glimpses of history and major milestones of magnetic levitation as well as a brief introduction to different magnetic levitation methods (CHAPTER 2).
- Chapter 3 provides the theoretical background on magnetism fundamentals, NeFeB magnets, static magnetic levitation and dynamic behavior of levitated diamagnetic material. Concept and theory that are relevant to magnetic levitation is introduced in order to bridge the knowledge barrier between physics and engineering. Magnetic levitation

can flourish by making both sides aware of both theory and possible application areas. (CHAPTER 3).

- Chapter 4 provides the experimental set up and experimental results of static and dynamic levitation and other measurements relevant to the system (CHAPTER 4).
- Chapter 5 explains, in detail, the COMSOL modeling procedure for permanent magnets and compares model results with experimental results (CHAPTER 5).
- Chapter 6 includes the static levitation model and magneto-mechanical coupling. Magnetic force and magnetic potential of the diamagnetic material were obtained from COMSOL simulations and compared with experimental results(CHAPTER 5)
- Chapter 7 explains the applicability of diamagnetic levitation in different applications, with the main focus on energy harvesters (CHAPTER 7).
- Chapter 8 concludes this dissertation, summarizing the achievements and contributions of this investigation (CHAPTER 8).

CHAPTER 2

LITERATURE REVIEW

This chapter provides a literature review on both magnetic levitation and energy harvesting devices. The chapter starts with the history of magnetic levitation, and the milestones achieved along the way. Then, different methods of levitation are reviewed with appropriate references and seminal works shown for each method, giving an emphasis for the work on magnetic levitation by permanent magnets. The next section discusses the advantages and disadvantages of levitation. The review concludes with an overview of energy harvesters.

2.1 History and Milestones of Magnetic Levitation

The possibility of diamagnetic levitation had been predicted by Lord Kelvin in 1847. The German physicist Braunbek was able to demonstrate diamagnetic levitation in 1939, more than 150 years after the observation of diamagnetism in materials and close to a century after Lord Kelvin's prediction. Braunbek studied the possibility of static stable levitation and found it was only possible using diamagnetic materials. He determined the necessary field configuration for stable levitation and built an electromagnet in which he levitated small pieces of diamagnetic graphite and bismuth [Simon 2000]. This observation is in contradiction to Earnshaw's theorem, which states that a charged particle in empty space cannot remain in stable equilibrium under electrostatic forces alone [Earnshaw 1842]. The theorem was later extended to magneto-

static forces and modern days the theorem is considered as not applicable for diamagnetic materials after the observation of diamagnetic levitation [Simon 2000].

Braunbek's demonstration of diamagnetic levitation in 1939 revived magnetic levitation for the 21st century. The past 50 years have been the most active time period in terms of investigating, understanding, and making use of magnetic levitation phenomena in macro scale applications (Eg. maglev trains, low friction bearings, etc.). In recent years, Gleim and other researchers from Nijmegen University in the Netherlands were able to levitate diamagnetic materials, including a living frog, with the help of a large magnetic field (16 T) inside a solenoid (Bitter magnet) [Berry 1997]. These experiments led them to two Nobel Prizes: The Ingor Nobel Prize for frog levitation and a Nobel Prize in 2010 for discovery of graphene. Berry and Geim were able to develop a theoretical equation that could predict the possible regions of stable levitation for electromagnetic levitation. Furthermore, a group of researchers including Geim and Simon were able to show the possibility of levitating a permanent magnet in between two fingers underneath a powerful superconductor magnet: in this case stabilization was achieved by diamagnetism in the fingers [Geim 1999]. Geim, Simon and Helfinger all contributed to developing the theory for stability regarding this observation [Geim 1999, Simon 2000]. Since 2000 the focus has branched out towards meso and micro scale levitation: In 2004, Igor Lyuksyutov and his colleagues from Texas A&M University presented a new device for the high precision manipulation of tiny floating diamagnetic droplets and particles, opening the possibility of magnetic levitation in micro scale devices [Lyuksyutov 2004]. In recent years a boom in research has been observed towards MEMS sensors and

actuators such as accelerometers, gyroscopes, position sensors, etc. Table 2.1 shows the major milestones of diamagnetic levitation and their respective years.

Table 2.1 Milestones of diamagnetic levitation.

Year	Event
1778	Observation of Diamagnetism by Anton Brugmans.
1842	Earnshaw's theorem.
1845	Michael Faraday rediscovers diamagnetism and names it.
1847	First prediction of magnetic levitation by William Thomson (Lord Kelvin) using mathematical formulae.
1939	First demonstration of levitation via electromagnets by W. Braunbek.
1952	Steingroever and the Boerdijk independently show diamagnetic levitation using a permanent magnet.
1964	Steingroever displays first use of anisotropic graphite (mono-crystal and pyrolytic) for levitation.
1965	Robert D. Waldron uses pyrolytic graphite for diamagnetic bearings.
1991	Levitation of water droplets by E. Beaugnon and R. Tournier.
1992	Ronald E. Pelrine builds a levitating permanent magnet array on a pyrolytic graphite disc.
1997	Andrey Geim *et al* levitate a frog
2004	Magnetic Micro-manipulation Chip by Lyuksyutov.
2007	D. Gamier investigates diamagnetic levitation for MEMS accelerometers.
2010	Kauffmann levitates Jurkat cells on a patterned trench.

2.2 Different Methods of Magnetic Levitation

Magnetic levitation methods can be broadly divided into two categories: active and passive. In the active method, the levitation force is generated by electromagnetic

means and often requires a feedback system to stabilize the levitation. In passive levitation, neither power nor a feedback system is required to achieve stable levitation. Levitation involving permanent magnets and superconductors belongs to passive levitation; however superconductors are categorized as a separate method because the mechanism of levitation of a superconductor is different from that of a permanent magnet.

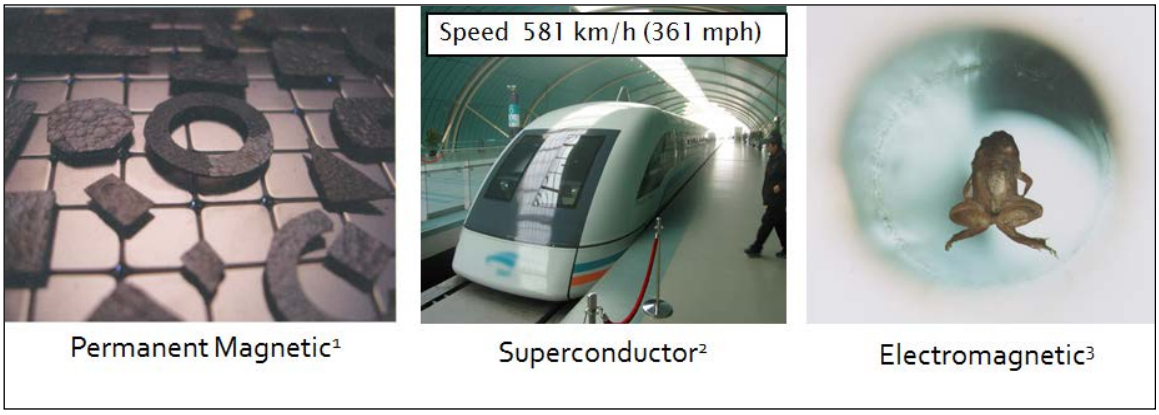


Figure 2.1 Different types of magnetic levitation ([1]Permanent magnetic [1][Pelrine, 2004],[2]Superconductor ["Transrapid" 2004], [3]Electromagnetic ["Highfield magnetic laboratory" 2009]).

2.2.1 Electromagnetic Levitation

Electromagnetic levitation applications can be found in magnetic levitation transport [Azukizawa 1989], bearings [Vischer 1993], high-accuracy position control of fusion fuel in nuclear reactors [Ishigaki 2009], vibration control [Hoque 2006], geophones [Dams 2009], and motion controllers [Teranishi 2002]. Electromagnetic levitation field is a mature field compared to passive magnetic levitation. The Maglev train is the most well-known electromagnetic application: development began in the

[1][Pelrine, 2004] Utilized with permission of the publisher.
[2] http://en.wikipedia.org/wiki/File:Shanghai_Transrapid_002.jpg.
[3] http://www.ru.nl/hfml/research/levitation/diamagnetic. Utilized with permission of the publisher.

1960s and was first employed in public transportation in Shanghai China in 2003. A speed of 581 km/h has reported by Japan's Maglev train in 2005 [Mizutani 2005]. Active magnetic bearings are one of the early industrial applications of the magnetic levitation concept. Active bearings have several advantages such as no parts to wear, contamination free, possessing low friction and the ability to position freely in the air gap. These bearings have industrial applications in electric power generation, petroleum refining, machine tool operation and turbo molecular pumps [Cansiz 2004].

2.2.2 Superconductor Levitation

Superconductors are considered a perfect diamagnet as the susceptibility (χ) is -1 and the permeability (μ) is zero. However, in superconductors, levitation occurs due to the Meissner effect (surface currents cancel the applied magnetic field), compared to the oppositely induced magnetic field which occurs in other diamagnetic materials. The stable levitation of a superconductor above a permanent magnet or vice versa has fascinated physicists since its discovery [Brandt 1989]. Arkadiev was the first to demonstrate the levitation of a permanent magnet using a bowl of lead superconductor in 1945 [Arkadiev 1945]. Japanese researchers were able to levitate a sumo wrestler weighing over 140 kg using superconductors [Livingston 2011]. Applications of superconductor levitation are also found in maglev trains. A group of physicists at Tel Aviv University in Israel has recently demonstrated superconductor levitation such that the superconductor hovered and rotated above the permanent magnet guiderail and was able to have it also hover and rotate when flipping the system upside down [Campbell 2011].

2.2.3 Permanent Magnet Levitation

The high power consumption of electromagnets and cryogenic requirements of superconductors has limited use of these methods in practical applications. Levitation using permanent magnets has attracted interest due to minuscule power consumption, stability without a control system, room temperature applicability and ease of miniaturization. In addition, devices can be built more compactly with permanent magnets compared to electromagnets or superconductors. Venues of using permanent magnets in levitation were opened after the discovery of powerful and relatively cheap sintered NdFeB permanent magnets in 1984 [Sagawa 1984]. Prior to this, the common rare earth permanent magnet being used was SmCo, which is expensive, brittle, prone to cracking and chipping and weaker in magnetic strength than NdFeB.

Diamagnetic levitation using permanent magnets was discovered by Pelrine: Initially, a permanent magnet was levitated using a block of graphite, following the experimental path of the first superconductor levitation, and later it was discovered that the opposite was also possible [Pelrine 1995]. In 1995, Pelrine received a patent for diamagnetic levitation using an ONP configuration of permanent magnets. SRI international developed and patented a hybrid levitation system based on Pelrine's observation to use as a wafer transporter in clean room environments as a contamination free alternative to traditional lubricant requiring machines [Schmidt 2001]. Further investigation of diamagnetic levitation by permanent magnets is being carried out by different groups in millimeter and micron scale devices. Simon *at el* has built a toy called "Leviton" to levitate a small cubical permanent magnet holding a more powerful ring of permanent magnets above it; stabilization has been achieved by placing the small

permanent magnet in between two graphite slabs [Simon 2001]. Mann and Sims have experimented with another way of levitation by permanent magnet, in which they have fastened two permanent magnets to two ends of a tube, and then suspended another permanent magnet in the middle facing the same polarity to the nearby magnets. These different methods of levitation and their characteristics are given in Table 2.2. As this research is based on levitating diamagnetic material using permanent magnets, the focus of literature review was henceforward given to levitation by the permanent magnets method.

2.2.3.1 Permanent Magnetically Levitated MEMS Devices

Magnetic MEMS devices have not been used in applications as much as electrostatic devices, mainly due to fabrication difficulties. However, magnetic MEMS actuation principles provide a number of advantages over electrostatic actuators, particularly low voltage and low power consumption combined with large actuation forces over relatively long distances. Cugat *et al* has shown that the magnetic force has special advantages when it comes to scale reduction over the electrostatic force as the magnetic force is multiplied by a factor while the electrostatic force diminishes by the same factor [Cugat 2003, Cugat 2006]. Additionally, magnetic MEMS devices have a much higher (~ four orders of magnitude higher) magnetostatic energy density than electrostatic energy density [Judy 2001]. Permanent magnets are more appropriate in realizing magnetic MEMS due to these reasons: 1) A permanent magnet can be scaled in all three dimensions, maintaining the same magnetic remanence. 2) There is no power consumption and no need of a cooling system. 3) Permanent magnet devices are failsafe as long as they are operated below the Curie temperature. In addition, NdFeB micro-

magnets have been fabricated via sputtering and electroplating methods and are able to be patterned into any desired shape [Niarchos 2003, Walther 2009]. This facilitates the freedom to form a variety of shapes and strength variations of magnetic flux compare to the limited shape variation seen in the electromagnet method. These facts suggest that levitation using permanent magnets particularly has more potential in MEMS and NEMS devices.

MEMS sensors and actuators using diamagnetic levitation have been investigated by different groups in the field of inertial sensors, biosensors and contactless bearings. Garmire *et al* has introduced the theory and a proof-of-concept design for MEMS-based, diamagnetically levitated accelerometers [Garmire 2007]. They have mounted a pre-fabricated SOI (silicon on insulator) proof mass with comb fingers to several layers of pyrolytic graphite, and have levitated it above NdFeB magnets in an ONP configuration. The change of capacitance in the lateral vibration has been obtained by aligning the electrostatic-sensing combs and thereby the acceleration. In addition, the possibility of using magnetic levitation on acceleration and inclination sensors based on diamagnetic levitation has been investigated by Barrot *et al* for structural health monitoring purposes. The advantage of this approach is low cost, three degree of freedom (DOF) and high sensitivity at low frequencies that has applications in earthquake monitoring [Barrot 2008]. Contactless handling methods are being extensively investigated presently for bio related applications such as trapping, positioning and handling. Chetouani *et al* have demonstrated a micro droplet levitating method using grooves made in permanent magnet films [Chetouani 2006]. The Walther group has advanced the field by micro patterning NdFeB magnets. They have been able to deposit 5 μm thick NdFeB films on a pre-

patterned trench structure [Walther 2009]. Following their work, the Kauffmann group has patterned NdFeB magnet holes in a similar manner and has been able to levitate Jurkat cells in patterned trenches [Kauffmann 2010].

Table 2.2 Review of the current *state of the art*.

System	Contribution	Author/Group
Permanent magnet levitation using PM	Dynamic and static analysis.	[Mann 2009], [Profijt 2009], [Damrongsak 2009], [Simon 2001],[Verma 2004]
Diamagnetic levitation by electromagnetic method	Levitating frog demonstration and mathematical derivation for electromagnetic levitation. Levitating micron size graphite particle. Nonlinear force oscillation. Applications :Gyroscope	[Berry 1997], [Geim 1999], [Savin 2009],[Inoue 2008], [Yates 1996]
Diamagnetic levitation using pyrolytic graphite and PM	Static levitating height -Variable thickness -Different magnet arrangement	[Pelrine 1995] [Garmire 2007] [Barrot 2008]
Diamagnetic levitation in biology	Contactless trap of micro droplets on and inside permanent magnets.	[Chetouani 2006],[Chetouani 2007],[Walther 2009], [Cugat 2004], [Kauffmann 2010], [Lyuksyutov 2004]
Modeling of diamagnetic levitation	Static modeling of levitating height	[Berry 1997], [Chetouani 2007]
Diamagnetic levitation in MEMS	Accelerometer application	[Garmire 2007]

The major disadvantage of the permanent magnet is that user does not have the ability to control the magnetic field intensity. An individual magnetization of an assembly of permanent magnets in more than one direction is also presently a challenge. The other disadvantage of the permanent magnet method is limitation of the maximum magnetic flux obtained by permanent magnets (lower than 1.5T using NdFeB) whereas there are electromagnets that provide a much higher magnetic flux (up to 32 T has been

achieved). However, this is not an obstacle for micro and meso scale devices as they do not demand high magnetic flux for their applications. The advantages and disadvantages of levitation using permanent magnets compare to electromagnet and superconductor method is given in Table 2.3.

Table 2.3 Advantage and disadvantage of levitation using the permanent magnet method.

	Advantages	**Disadvantage**
Permanent magnet vs. other methods (i.e. Super conductor, Electromagnetic)	Minuscule power consumption Room temperature applicability Low cost Stability No need of control system	User does not have the controllability

2.3 Levitation Advantages

Device attachment to the substrate is a major obstacle to optimal performance in many applications in both macro and micro devices. The significance of this effect is especially high in MEMS applications such as resonators, inertial sensors, biosensors and energy harvesters. These attachments limit and alter the dynamic behavior of the moving part of the device in addition to difficulties such as final adjustments, life time limitation, power dissipation, etc. Dissipative effects take place inside structural components that are subjected to bending as a consequence of internal friction in solids. Moreover, attachment introduces a higher overall stiffness to the system, elevating the resonance frequency of the system.. Element bending also affects the device reliability and durability due to mechanical fatigue, a process that takes place in structures that are subjected to alternate loads.

One possible solution to this problem is contact free-levitation of the vibrating or moving part using methods such as magnetic levitation. An additional benefit deriving

from magnetic levitation is the prevention of stiction effects between the proof-mass and the substrate. This problem is common in micro scale devices, particularly those related to biology which operates in liquid or humid environments. Obstacles associated with stiction can be avoided by the diamagnetic levitation approach, as the force between the device and the substrate is repulsive, thus preventing contact. Furthermore, levitation enables chip assembly, i.e. part of the device can be fabricated separately and then assembled together at a later stage. This is an added advantage when the device has thermal mismatch processing, or operation of the device is sensitive to processing imperfections.

Table 2.4 Advantages and disadvantages of levitating and attached systems.

	Advantages	**Disadvantage**
Levitated vs. Attached Systems	Higher DOF Durability No fatigue No stiction Low Stiffness Part replacement ability	Not applicable for all Materials Stability Difficulty in handling

2.4 Energy Harvesters

Depletion of conventional natural energy sources and an increase in demand for energy has pushed us to think about alternative energy sources. Energy harvesters are currently an active field of study and the present US government is providing encouragement and support to find reliable alternative energy sources. Wireless devices are becoming increasingly popular in the world, demanding wireless energy solutions for devices. There are several different energy harvesting sources such as vibrations, solar power, wind power, and thermal energy, all being investigated to accomplish this goal. As this research is focused on vibration based energy harvesters, literature review is

limited to vibrational based energy harvesters. Vibrational energy is generally extracted by the means of electromagnetic, piezoelectric or electrostatic mechanisms and is used to power electrical devices either directly or transmitted to batteries for storage. Vibrations can be found in numerous applications, including common household goods (fridges, washing machines, computers, etc), industrial machinery, moving structures such as automobiles and aeroplanes, and structures such as buildings and bridges. A few of these sources and their fundamental vibration frequencies are listed in Table 2.5, taken from the reference of Roundy *et al*.

Table 2.5 Acceleration and resonance frequency of fundamental vibration mode for various sources [Roundy 2003].

Vibration source	**Acceleration (m/s^2)**	**Resonance Frequency (Hz)**
Car engine compartment	12	200
Base of 3-axis machine tool	10	70
Blender casing	6.4	121
Clothes dryer	3.5	121
Person nervously tapping their heel	3	1
Car instrument panel	3	13
Door frame just after door closes	3	125
Small microwave oven	2.5	121
HVAC vents in office building	0.2-1.5	60
Windows next to a busy road	0.7	100
CD on notebook computer	0.6	75
Second story floor of busy office	0.2	100

2.4.1 Piezoelectric

Piezoelectric materials convert strain into an electric charge. They are widely available in many forms including single crystal (e.g. quartz), piezoceramic (e.g. lead zirconate titanate- PZT), thin film (e.g. sputtered zinc oxide), screen printable thick-films based upon piezoceramic powders and polymeric materials such as polyvinylidenefluoride (PVDF) [Beiber 2006]. A cantilever structure with a piezoelectric

material attached to the top and bottom surfaces has been the most attractive geometry for harvesting energy from vibrations [Shen 2008].

2.4.2 Electromagnetic

Electromagnetic generators employ electromagnetic induction arising from the relative motion between a magnetic flux gradient and a conductor. The conductor typically takes the form of a coil and electricity is generated by either the relative movement of the magnet and coil, or because of changes in the magnetic field [Beiber 2006]. In the former case, the amount of electricity generated depends upon the strength of the magnetic field, the velocity of the relative motion and the number of turns of the coil. A novel energy harvesting device that uses magnetic restoring forces to levitate an oscillating central magnet has been introduced by Mann and Sim. In this method, energy is harvested by a coil wrapped around a tube that has a magnetically suspended oscillating magnet [Mann 2009].

2.4.3 Electrostatic

A capacitor consists of two plates which are electrically isolated from each other, typically by air, vacuum or an insulator. Capacitance C is given by,

$$C = \frac{\varepsilon_0 \varepsilon_r A_r}{d_a} \tag{2.1}$$

where, ε_0 is the permittivity of the free space, ε_r permittivity of the medium, A_r the area of the electrode and d_a the distance between electrodes. Electrostatic harvesters are built in such a way that vibrations create a change of A_r and d_a in the device and hence change the capacitance. The changes of capacitance are stored and convert to voltage by an electrical circuit to power the required device. Electrostatic generators can be

classified into three types: 1) In-plane overlap, 2) In-plane gap closing, and 3). Out-of-plane gap closing [Beiber 2006]. Electrostatic converters have the advantage in that they can be more easily implemented with MEMS technology. Electret energy harvesters are a newly added branch to the electrostatic technique. The advantage of this method is that it does not require an electronic circuit to convert capacitance variation to voltage and is able to provide generated power directly to the device.

CHAPTER 3

THEORETICAL BACKGROUND

This chapter covers the essential theoretical knowledge required to understand and explain the static and dynamic behavior of the diamagnetic levitation systems, as well as the theory necessary in COMSOL modeling. The chapter starts with the fundamentals of magnetism and magnetic materials, and leads to build relations for magnetic forces in static levitation and dynamic relations based on the Duffing equation. Also, the theory related to permanent magnets and two different analytical formulas for magnetic flux calculations existing in the literature will be introduced.

3.1 Important Definitions

Some definitions and notations in magnetism are quite confusing as some books use the same notation for different contexts. For example, $\boldsymbol{B}$ is used to denote both magnetic flux density and the magnetic field, which have distinct differences. Table 3.1 gives the definition and notation used in this dissertation. Additionally Table 3.2 gives the cgs (Centimeter-gram-second) and SI (International system of units of measurement) units of parameters and their conversions.

Table 3.1 Definition and notation of some magnetic parameters.

Parameter	Description	Notation	SI unit
Magnetic flux Density (Mag. Induction)	Magnetic flux per unit area at a given point in space.	**B**	T
Magnetic field	A region around a magnetic material, electric current or a moving charge where a magnetic force acts on any other magnet or moving charge.	**H**	Am^{-1}
Magnetic flux	The total number of magnetic lines of force passing through a specified area in a magnetic field.	Φ	Weber
Magnetization	Total magnetic dipole moment in a unit volume.	**M**	Am^{-1}
Coercivity	The amount of reverse magnetic field that must be applied to a magnetic material to make the magnetic flux return to zero.	H_c	Am^{-1}
Remanence	The magnetization value that remains in a material when the magnetic field is removed.	Br	T
Permeability	The amount of magnetic flux density that will occur for a given magnetic field intensity (H).	μ	$N \cdot A^{-2}$

Table 3.2 The cgs and SI units of some magnetic parameters and their conversions.

Parameter	cgs Unit	SI Unit	Conversion
Magnetic flux density (**B**)	Gauss (G)	Tesla (T)	$1G = 10^{-4}T$
Magnetic Field (**H**)	Oersted (Oe)	A/m	$1Oe = (10^3/4\pi)\ Am^{-1}$ $1Oe = (1/4\pi)G$
Magnetization (**M**)	Gauss (G) emu/cm^2	A/m A/m	$1G = 10^3 Am^{-1}$ $1emu/cm^{-3} = 1000\ Am^{-1}$
Susceptibility (χ) Volume (χ_v) Mass (χ_{mass}) Molar (χ_{mol})	 Dimensionless $g^{-1}\ cm^3$ $mol^{-1}cm^3$	 Dimensionless $kg^{-1}m^3$ $mol^{-1}\ m^3$	4π cgs = 1 SI
Magnetic flux (Φ)	Maxwell	Weber	$1\ Maxwell = 10^{-8}$ Weber
Magnetic Energy $(BH)_{max}$	GOe	Jm^{-3}	$1\ GOe = (1/40\pi)\ Jm^{-3}$

3.2 Quantum Interpretation of Magnetism

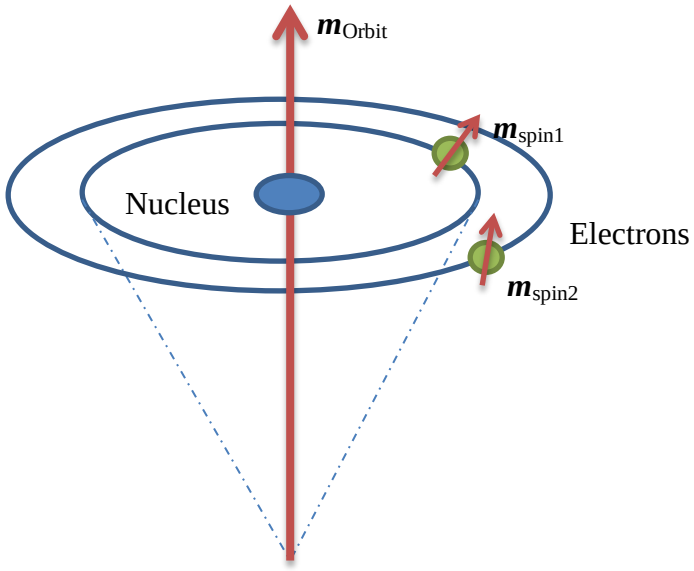


Figure 3.1 Magnetism formation in a free atom.

Magnetism is generated in a material due to the movements of electrons in the atom. There are two types of motion that generate magnetic moment of a free atom, 1) current generated due to the orbital motion of electrons around the nucleus, identified as orbital magnetic momentum and 2) electron spin motion identified as spin magnetic moment [Stohr 2006]. The coupling magnetic moment attributes to the total magnetic dipole moment ($\boldsymbol{m}$) of a material are,

(1) Orbital and spin

(2) Orbit and orbit

(3) Spin and spin

The magnetic material type depends on the prominent contribution of each coupling type and the strength of the magnetic dipole moment. Diamagnetism of the material arises due to orbital angular momentum and can also be explained using Len's

law in classical physics. Paramagnetism arises due to the spin motion, and other forms of magnetism (ferro, ferri, antiferro) arise due to the exchange interaction of magnetic dipoles that can solely be explained by quantum mechanics [Getzlaff 2008].

3.3 Magnetic Hysteresis Curve

A B-H graph shows how a magnetic material behaves as it is brought to saturation, demagnetized, saturated in the opposite direction and then demagnetized again by an external magnetic field.

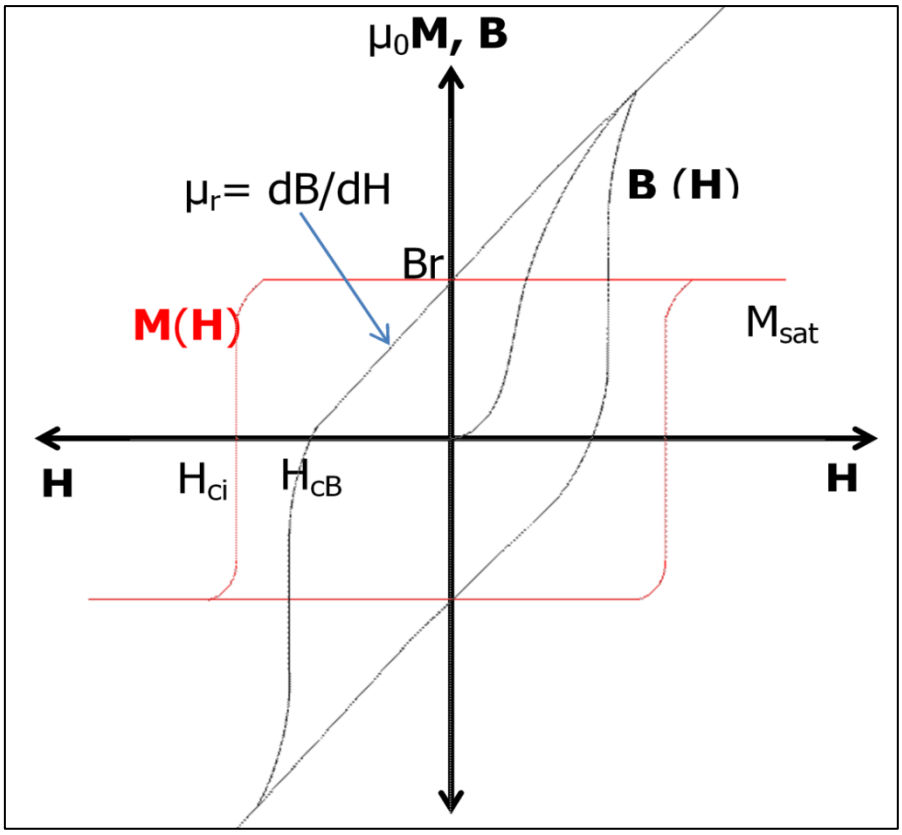


Figure 3.2 ***M*** vs. ***H*** and ***B*** vs. ***H*** curves.

There are two types of hysteresis loops: Magnetization ***M*** vs. ***H*** (also is given as magnetic polarization, ***J*** (***J***= μ_0***M***) in some books and data sheets) and magnetic induction ***B*** vs. ***H***. Magnetization, ***M*** is the magnetic dipole moment per unit volume of

the material and $\boldsymbol{H}$ is the magnetic field strength. The Hysteresis loop depicts the properties of the material: permanent magnets exhibit a wider loop and soft magnets exhibit a narrow loop while diamagnetic materials give a straight line. The second quadrant of the hysteresis graph defines the parameters B_r, H_{ci}, H_{cB}, μ_r and $(BH)_{\max}$. Therefore, in most technical datasheets only the second quadrant of the $\boldsymbol{B}$-$\boldsymbol{H}$ and $\boldsymbol{J}$-$\boldsymbol{H}$ representations are given for permanent magnets. The important parameters that can be extracted from these curves are as follows:

(1) Saturation magnetization (M_{sat}) - the maximum possible magnetization value of a material that can be achieved when an external magnetic field is applied.

(2) Remanent magnetization **(**M_r**)** - the magnetization value that remains in a material when the magnetic field is removed. The remanent magnetization is known as retentivity when the material has been magnetized to the saturation point.

(3) Remanence induction (B_r) - The magnetic induction that remains in the material after the removal of an applied magnetizing field.

(4) Coercive field **(**H_c**)** - the amount of reverse magnetic field that must be applied to a magnetic material to make the magnetic flux return to zero. H_{ci} = Intrinsic coercivity (or switching field) and H_{cB} = Coercivity of $\boldsymbol{B}$.

(5) Relative permeability (μ_r) - The ratio of permeability of a medium to that of a vacuum.

(6) Maximum energy product $(BH)_{\max}$ – the maximum energy that can be supplied by the magnetic material.

The response of a material when applying an external magnetic field $\boldsymbol{H}$ is called magnetic induction (or magnetic flux density) $\boldsymbol{B}$. The relationship between $\boldsymbol{H}$ and $\boldsymbol{B}$ is a characteristic property of the material itself. In vacuum, a linear correlation between $\boldsymbol{B}$ and $\boldsymbol{H}$ is given by,

$$\boldsymbol{B} = \mu_0 \boldsymbol{H} \tag{3.1}$$

In order to describe the fields existing in matter, a third field vector, the magnetization $\boldsymbol{M}$ is introduced. The relation between $\boldsymbol{B}$ and $\boldsymbol{H}$ inside a magnetic material is given by,

$$\boldsymbol{B} = \mu_0(\boldsymbol{H} + \boldsymbol{M}) \tag{3.2}$$

If the magnetization $\boldsymbol{M}$ is parallel to an external magnetic field $\boldsymbol{H}$,

$$\boldsymbol{M} = \chi\, \boldsymbol{H} \tag{3.3}$$

Hence,

$$\boldsymbol{B} = \mu_0(\chi + 1)\boldsymbol{H} \tag{3.4}$$

$$\boldsymbol{B} = \mu_0 \mu_r \boldsymbol{H} \tag{3.5}$$

The ratio of the magnetization $\boldsymbol{M}$ to $\boldsymbol{H}$, which is the measure of how susceptible the material is to becoming magnetized, is called the magnetic susceptibility χ of the material. There are three kinds of susceptibilities: volume magnetic susceptibility (χ_v), mass magnetic susceptibility (χ_{mass}) and molar magnetic susceptibility (χ_{mol}). One may get confused with the term magnetic susceptibility, as often in literature magnetic susceptibility is given without referring to the kind or using the symbol without the subscript notation. Magnetic susceptibility has different values and meaning depending on the units it uses or the context. In this dissertation, we will use χ for the volume susceptibility. The volume susceptibility is a dimensionless quantity while the other two

susceptibilities have units as seen in Table 3.2. The magnetic susceptibility of a material can be a tensor if $\boldsymbol{M}$ has components other than the direction of the applied magnetic field $\boldsymbol{H}$.

3.4 Magnetic Material

Magnetic materials can be categorized depending on their permeability (μ) into five categories; ferromagnets, antiferromagnets, ferrimagnets, paramagnets and diamagnets. For diamagnetic and paramagnetic materials, $\boldsymbol{M}$ is zero when there is no applied magnetic field. Permanent magnets exhibit magnetization called magnetic remanence ($\boldsymbol{B_r}$), even in the absence of external field. In this research two types of magnets were used: ferromagnets (NdFeB permanent magnet falls in to this category) and diamagnets (Pyrolytic graphite). Ferromagnets (materials consisting of atoms with a net magnetic moment) have the highest permeability (e.g. Iron has a relative permeability of 4,000 and some forms even have a value as high as 10,000). However, NdFeB exhibits low permeability close to 1. Paramagnets and diamagnets have similarities, such as both have no permanent magnetic moments and both have small permeability values. However, the materials are different due to the fact that paramagnets have permeability $\mu > 1$ and diamagnets have $\mu < 1$. In other words, the susceptibility χ of diamagnetic materials is negative whereas is positive for paramagnets.

In this dissertation detailed discussion is limited to NdFeB (permanent magnet) and pyrolytic graphite (diamagnet) as they were the base magnetic materials used. It is important to understand the properties and formation of the aforementioned magnets for both experiments and modeling.

3.5 Diamagnetism

Diamagnetism is the property of a material that causes repulsion when an external magnetic field is applied. It arises from the precession of spinning charges in a magnetic field. In the absence of external magnetic field, orbital electrons generate randomly aligned fields which cancel one another so that the material does not generate an overall field of its own. When subjected to an external magnetic field, the electrons speed up or slow down to oppose the change inside their orbits. The net effect is an induced magnetization that opposes the applied field, causing a repulsive force [Pelrine 2004].

All substances have diamagnetism, however the effect is hindering when the other forms of magnetism are present, as the diamagnetism is a very small quantity. The magnetism of conventional metal comes from two different contributions: the Pauli paramagnetism due to the spin magnetic moment, and the Landau diamagnetism due to the orbital motion of electrons. In a free electron system, the magnitude of the spin component is larger than the orbital component so that the system exhibits net paramagnetism. In a condensed matter system, on the other hand, the orbital magnetism sensitively depends on the detail of the band structure, and sometimes largely deviates from the conventional Landau diamagnetism. In particular, narrow gap materials such as graphite or bismuth possess a strong orbital diamagnetism which overcomes the spin paramagnetism [Koshino 2011]. Some substances that show diamagnetism are graphite, bismuth, water, human cells, copper, silicon, carbon nanotubes, graphene [Simon 2001, Fujiwara 2001, Ratner 2004].

3.5.1 Pyrolytic Graphite

Pyrolytic graphite is a form of carbon that does not exist in nature but is produced by heating hydrocarbons to a high temperature [Yousefi 2006]. Pyrolytic carbon is a material similar to graphite, but with a large inter-spacing distance between layers and some covalent bonding between its graphene sheets as a result of imperfections in its production [Ratner 2004]. Pyrolytic graphite shows the highest diamagnetism of all at room temperature due to some of its electrons travel in larger than normal orbits [Pelrine 2004].

3.6 Permanent Magnets

Prior to 1951, inexpensive permanent magnets could only be made into limited shapes such as needles, bars and horseshoes. The shape barrier was broken in 1951 with the discovery of a new family of materials, Ferrimagnetic hexagonal ferrites, which can be manufactured into magnets whose coercivity (H_c) exceeds the spontaneous magnetization (M_s) [Coey 2011]. Many permanent magnet materials are manufactured in a way that enhances their magnetic properties along a preferred axis, making them anisotropic, because in most applications only the field produced in a particular direction is interested [Campbell 1994]. Requirements for uniaxial anisotropy are that the magnet should have a uniaxial crystal structure –tetragonal, rhombohedral or hexagonal. Modern permanent magnets are based on highly anisotropic rare earth–3d alloys. The magnetic moments of the 3d atoms are mainly based on the spin of electrons, because the angular magnetic moments are usually quenched and therefore annihilated [Kirchmayr 1996]. Ferromagnetic materials have atoms in which one electron shell contains fewer than the maximum number of electrons. In such unfilled shells, there are one or more unbalanced

electron spins, giving rise to a small magnetic moment and making the atom itself a tiny magnet. Normally, in a large collection of such atoms, the atomic magnetic moments point in various directions and cancel out one another. If a sample of ferromagnetic materials is placed in a magnetic field, however, the individual atomic magnets tend to line up so that when the sample is removed from the field it retains a net residual magnetism. The total magnetization, $\boldsymbol{M}$, is the sum of the contributions of all the elementary atomic magnets. The magnetization in any direction reaches its saturation value when all the atomic magnets are parallel and pointing in the same direction [Jayawant 1998].

Neodymium Iron Boron ($Nd_2Fe_{14}B$) has the highest remanence among all rare earth based permanent magnets. There are two ways to make such magnets: Sintering and bonding. A brief description of the manufacturing method and characteristics of sintered and bonded magnets are given in Appendix. Sintered magnets have higher remanence magnetic flux densities and hence a higher magnetic force. The highest remanence material has the lowest maximum operation temperature, while materials with the highest coercivity have the highest maximum operation temperature. The magnets can be either isotropic or anisotropic depending upon their manufacturing method. A magnet is said to be anisotropic when the magnetic properties depend on the axis along which magnetic measurements are made. The magnetic anisotropy may arise from the shape of the particle, from magneto-crystalline effects, and from strain [Stoner 1947].

3.7 Mathematical Model for Calculating the Magnetic Field Space above Permanent Magnets

The magnetic field of an electromagnet is given by the rather simplistic form of,

$$\boldsymbol{B}(\boldsymbol{r}) = \int \frac{\mu_0 \mathrm{I}\ \mathrm{dl} \times \boldsymbol{r}}{4\pi|\mathrm{r}|^3} \qquad 3.6$$

where $\boldsymbol{I}$ is the current, *dl* is the differential length of the wire and $\boldsymbol{r}$ is the displacement vector.

The magnetic field distribution of a permanent magnet however is complex, and unlike for electromagnets, there is no simple equation developed to predict the field distribution in space. In literature, there are two models that have been presented to calculate and characterize the magnetic field distribution of permanent magnets. One is the scalar potential model (*charge model*), and the other is the vector potential model (*current model*) [Furlani 2001].

In the *current model*, the magnet is reduced to a distribution of equivalent current. This is then input into the magneto-static field equations as a source term, and the field is obtained using standard methods for steady currents. In the *charge model*, a magnet is reduced to a distribution of equivalent ‘‘magnetic charge’’. The charge distribution is used as a source term in the magneto-static field equations, and the fields are obtained using standard methods [Xiao-fan 2004].

The magnetic flux density of a given point in space can be written using the *charge model* as,

$$\boldsymbol{B}(x,y,z) = \frac{\mu_0 \boldsymbol{M}}{4\pi}\sum_{k}^{2}(-1)^k \int_{y_1}^{y_2}\int_{x_1}^{x_2} \frac{(x-x')\boldsymbol{e_x} + (y-y')\boldsymbol{e_y} + (z-z_k)\boldsymbol{e_z})}{[(x-x')^2 + (y-y')^2 + (z-z_k)^2]^{\frac{3}{2}}} dx'dy' \quad 3.7$$

where $\boldsymbol{M}$ is the magnetization of the permanent magnet and μ_0 is the permittivity of free space.

The *current model*,

$$\boldsymbol{B}(x) = \frac{\mu_0}{4\pi}\int \boldsymbol{J}_m(x') \times \frac{(\boldsymbol{x}-\boldsymbol{x}')}{|(\boldsymbol{x}-\boldsymbol{x}')|^{3'}} dv' \quad 3.8$$

where $\boldsymbol{J_m}$ is the volume current density.

3.8 Magnetic Levitation Phenomena

The Earnshaw Theorem states that a collection of point charges cannot be maintained in a stable stationary equilibrium configuration solely by the electrostatic interaction of the charges [Geim 1999, Jones 1980]. This was later extended to magnetostatic fields. According to the Earnshaw Theorem, diamagnetic materials (i.e. collections of magnetic dipoles) cannot stably levitate using permanent magnets (collections of dipoles). Therefore, there are no local minima or maxima of the field potential in free space, only saddle points. This can be mathematically proved as follows:

From Gauss Theorem,

$$\nabla . \boldsymbol{B} = 0 \quad 3.9$$

If $\boldsymbol{B}$ is a conservative field (no variation of $\boldsymbol{B}$), a scalar magnetic potential can be defined as,

$$\boldsymbol{B} = -\nabla V_m \quad 3.10$$

Therefore,

$$\nabla^2 V_m = 0 \tag{3.11}$$

By substituting ψ, a scalar potential at a point to equation 3.11 (Laplace's equation),

$$\frac{d^2\psi}{dx^2} + \frac{d^2\psi}{dy^2} + \frac{d^2\psi}{dz^2} = 0 \tag{3.12}$$

In order for levitation of the object in an equilibrium state,

$$\frac{d\psi}{dx} = \frac{d\psi}{dy} = \frac{d\psi}{dz} = 0 \tag{3.13}$$

For this condition to be fulfilled the potential should be a minimum (i.e. second derivative of $\psi > 0$). In equation 3.12, if two quantities are positive, the other should be negative. That means the object is not in equilibrium in one direction, hence stable levitation by a static magnetic field is not possible in space using a static magnetic field. Levitation can be achieved if conditions for the theorem are violated. Some physicist and engineers have attained levitation by different means; however physics need to fully explain levitation or disprove the Earnshaw theorem, which has yet to be accomplished.

3.8.1 Analytical Models for Static Levitation

There are two formulas in the literature for the magnetic force on an elementary dipole ***m***: one was developed using the electric current loop model and the other using the magnetic charge model. Though the two models are treated as the same in textbooks, they have distinct differences and lead to two different force expressions for the magnetic dipole [Boyer 1987].

Magnetic force on a magnetic dipole from the *electric current model* [Boyer 1987, Barrot 2007],

$$\boldsymbol{F_i} = \nabla(\boldsymbol{m} \cdot \boldsymbol{B}) \tag{3.14}$$

Magnetic force on a the magnetic dipole from *charge model* [Fulani 2001, Boyer 1987],

$$\boldsymbol{F_i} = (\boldsymbol{m} \cdot \nabla)\boldsymbol{B} \tag{3.15}$$

The difference between the outcomes of two models can be shown by taking vector identity,

$$\nabla(\boldsymbol{m} \cdot \boldsymbol{B}) = \boldsymbol{m} \times (\nabla \times \boldsymbol{B}) + \boldsymbol{B} \times (\nabla \times \boldsymbol{m}) + (\boldsymbol{m} \cdot \nabla)\boldsymbol{B} + (\boldsymbol{B} \cdot \nabla)\boldsymbol{m} \tag{3.16}$$

$$\nabla(\boldsymbol{m} \cdot \boldsymbol{B}) - (\boldsymbol{m} \cdot \nabla)\boldsymbol{B} = \boldsymbol{m} \times (\nabla \times \boldsymbol{B}) + \boldsymbol{B} \times (\nabla \times \boldsymbol{m}) + (\boldsymbol{B} \cdot \nabla)\boldsymbol{m} \tag{3.17}$$

$$\boldsymbol{F_i^{Current}} - \boldsymbol{F_i^{Charge}} = \boldsymbol{m} \times (\nabla \times \boldsymbol{B}) + \boldsymbol{B} \times (\nabla \times \boldsymbol{m}) + (\boldsymbol{B} \cdot \nabla)\boldsymbol{m} \tag{3.18}$$

In order for both expressions given in equation 3.14 and 3.15 to be the same, the right hand side of equation 3.17 should be equal to zero.

The first controversy of the accuracy of the two models involved the experimental results of the magnetic moment of neutrons. Two groups have calculated the scattering of neutrons from a ferromagnetic material using the *current model* and the *charge model*. Experimental results have agreed with the *electric current model* and disagreed with the *charge model*, confirming the *current model* as the correct model for the neutron dipole moment [Jackson 1977]. Also, the force expression given in equation 3.14 predicts a repulsive or attractive magnetic force. However, an experiment done later by Aharonov and Casher has achieved agreement with the *charge model* [Boyer 1987]. In addition, Chetouani *et al* has taken the magnetic force as $\nabla(\boldsymbol{m} \cdot \boldsymbol{B})/2$ for their models [Chetouani 2007]. The applicability and accuracy of these different equations will be investigated using measurements and model results in *Chapter 6*.

3.8.1.1 Magnetic Force from Current Model

Magnetic force due to a unit volume [Boyer 1987],

$$\boldsymbol{F_m} = \nabla(\boldsymbol{M} \cdot \boldsymbol{B}) \tag{3.19}$$

For diamagnetic materials,

$$\boldsymbol{M} = \chi \boldsymbol{H} = \chi \frac{\boldsymbol{B}}{\mu_0} \tag{3.20}$$

$\boldsymbol{M}$ is the magnetization of a unit volume and χ is the volume susceptibility. The final expression for the magnetic force,

$$\boldsymbol{F_m} = \frac{\chi}{\mu_0} \nabla (\boldsymbol{B} \cdot \boldsymbol{B}) \tag{3.21}$$

The z- direction force for the entire volume,

$$F_{m,z} = \iiint \frac{\chi_z}{\mu_0} \frac{d}{dz} B_z^2 \, dv \tag{3.22}$$

where dv is the unit volume of the diamagnetic material. Taking the z- direction force equivalent to the weight of the levitating mass,

$$\text{mg} = \iiint \frac{\chi_z}{\mu_0} \frac{d}{dz} B_z^2 \, dv \tag{3.23}$$

The force and potential energy relation,

$$\boldsymbol{F_m} = -\nabla U \tag{3.24}$$

The dipole energy of a unit volume is,

$$U = -(\boldsymbol{M} \cdot \boldsymbol{B}) = (\chi \frac{\boldsymbol{B}}{\mu_0}) \cdot \boldsymbol{B} \tag{3.25}$$

$$U \propto -\boldsymbol{B}^2 \tag{3.26}$$

3.8.1.2 Magnetic Force from Charge Model

Magnetic force due to the unit volume [Furlani 2001],

$$\boldsymbol{F_m} = (\boldsymbol{M} \cdot \nabla)\boldsymbol{B} \tag{3.27}$$

For diamagnetic materials,

$$\boldsymbol{M} = \chi \boldsymbol{H} = \chi \frac{\boldsymbol{B}}{\mu_0} \tag{3.28}$$

The final expression for the magnetic force,

$$\boldsymbol{F_m} = \frac{\chi}{\mu_0} (\boldsymbol{B} \cdot \nabla)\, \boldsymbol{B} \tag{3.29}$$

Magnetic force due to the entire volume [Barrot 2008],

$$\boldsymbol{F_m} = \iiint \frac{\chi}{2\mu_0} \nabla \boldsymbol{B}^2 \, dv \tag{3.30}$$

3.8.2 The Analytical Model for the Dynamic Behavior

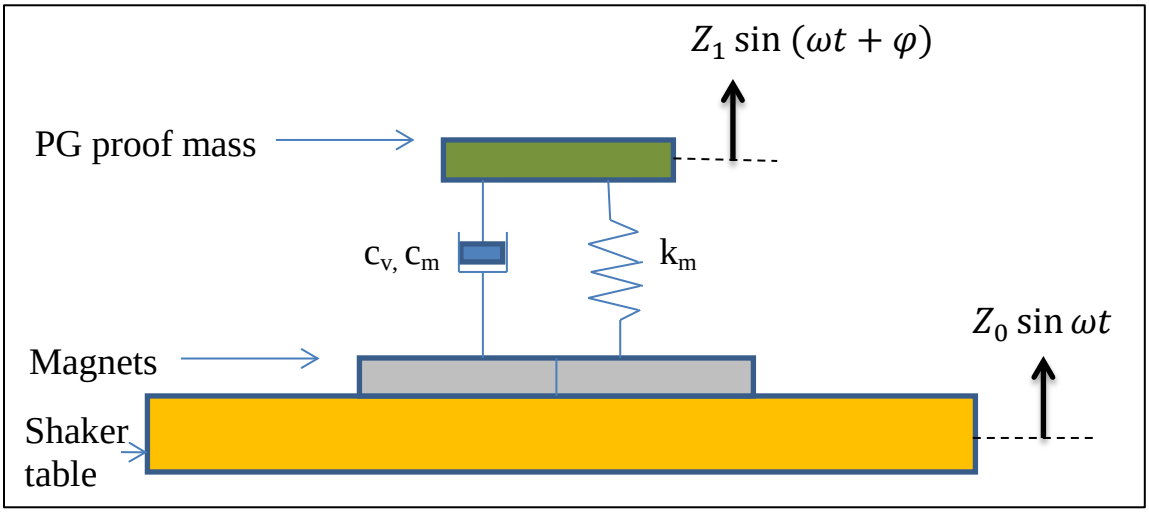


Figure 3.3 Single DOF model of levitating magnetic suspension.

Figure 3.3 represents the single degree of freedom (DOF) model of levitating suspension, with the mass (m) of the levitating diamagnetic material, the magnetic

stiffness (k_m) given by the repulsive effect, the viscous damping (c_v) due to the compression of air when the plate is moving, and the magnetic damping (c_m).

The time dependent periodic force can be written as a Fourier series [Senturia 2002],

$$\boldsymbol{F}(t) = \sum \boldsymbol{F_n} \cos(n\omega t) \tag{3.31}$$

If we know the response of the system $\boldsymbol{F_1} \cos \omega t$, in general the solution for any periodic force can be found by superposition of solutions for each ω.

If it is an un-damped linear oscillator, the equation for vibration is,

$$\mathrm{m}\,\ddot{\mathrm{Z}} + k\,\mathrm{Z} = \boldsymbol{F_1} \cos \omega\,\mathrm{t} \tag{3.32}$$

where m is the mass, Z is the displacement of the mass, F_1 is the amplitude of the force and ω is the frequency of the force. The general solution for this equation can be written as,

$$Z(t) = C \cos \omega_0 t + D \ sin\ \omega_0 t + s2 \tag{3.33}$$

Substituting in initial conditions, the complete solution can be written as,

$$Z(t) = \frac{\boldsymbol{F_1}}{m({\omega_0}^2 - \omega^{2)}} \ (\cos \omega t - \cos\ \omega_0 t) \tag{3.34}$$

The equation for the damped linear oscillator with the damping coefficient c is,

$$m\,\ddot{Z} + c\dot{Z} + k\,Z = \boldsymbol{F_1} \cos \omega\, t \tag{3.35}$$

The solution for the equation 3.35 is,

$$Z(t) = e^{\frac{-\gamma t}{2}}(\ C \cos \omega_0 t + D \ sin\ \omega_0 t) + S3 \tag{3.36}$$

where $\gamma = c/m$ and S3 is the particular solution. For a sufficiently long time, equation 3.36 reduces to,

$$Z(t) = A \cos(\omega t - \varphi) \tag{3.37}$$

where amplitude, A and angle, φ is given by,

$$A = \frac{F/m}{\sqrt[2]{(\omega_0^2 - \omega^2)^2 + \gamma^2\omega^2}} \tag{3.38}$$

$$\tan\varphi = \frac{\gamma\omega}{(\omega_0^2 - \omega^2)} \tag{3.39}$$

Considering the forces acting on the levitating mass, the resultant force $\boldsymbol{F_1}$ can be written as,

$$\boldsymbol{F_1 = F_m + F_s + F_g + F_c} \tag{3.40}$$

with the magnetic force ($\boldsymbol{F_m}$), the force from the mechanical shaker ($\boldsymbol{F_s}$), the gravitational force of the graphite ($\boldsymbol{F_g}$) and the damping force ($\boldsymbol{F_c}$).

CHAPTER 4

EXPERIMENTAL DATA

The objective of this chapter is to experimentally investigate the static and dynamic behavior of diamagnetic levitating systems that consist of permanent magnets (PMs) and pyrolytic graphite (PG) specimens, referred here onwards as proof masses. The parametric studies of key design parameters (i.e. magnetic flux density and dimensions of PGs) influence on static and dynamic performance of the levitated systems are examined. The resonance frequencies and stiffness variation with the physical and magnetic parameters of the systems are established by the dynamic experimental results. Qualitative experimentations conducted by scaling down the dimensions of the systems also are presented with comparison of the scaling effects on the dynamic response. Additionally, the graphite stable equilibrium position variations with the dimensions of PG in a 2D array of nine magnets arrangement are documented. Finally, a semi-empirical study carried out to investigate the motion-dependent magnetic forces derived from experiment results is presented.

4.1 Static and Dynamic Experiment Organization

The goal of this investigation is to obtain both quantitative and qualitative results in order to understand and optimize systems that have magnetically levitated diamagnetic materials. The required magnetic field for levitation is obtaining by permanent magnets that are arranged in an o*pposite neighboring poles* (ONP) configuration. The static and

dynamic studies of the levitating systems conduct by changing different variable components of the system. The two parameterized systems investigated in this research are:

(1) System 1: Variable length (l) with constant thickness (t) of rectangular pyrolytic graphite proof masses and N number of magnetic layers.

(2) System 2: Variable thicknesses (t) with constant length (l) of rectangular pyrolytic graphite proof masses and N number of magnetic layers.

The Figure 4.1 shows the graphical representation of the two systems used in this study. Table 4.1 provides the physical parameters and variables of the levitating system.

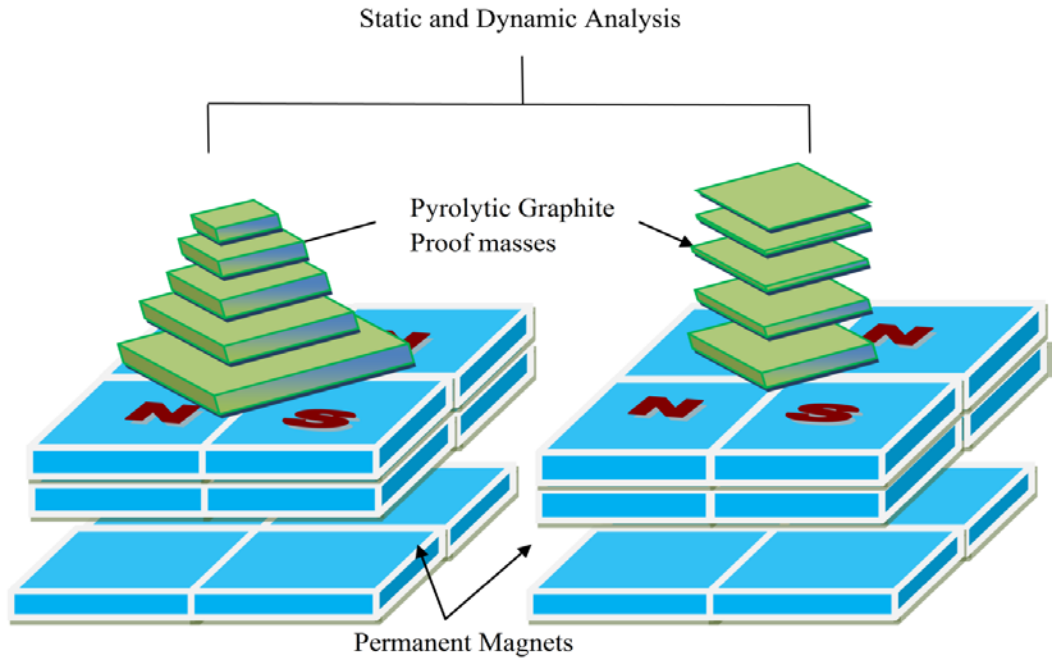


Figure 4.1 Graphical representation of the two systems that test both the static and dynamic behavior of the levitating systems. The N layers of the underlying magnet (N=1, 2 and 3) provide variable magnetic field strengths.

4.2 Experiment Setup

The magnetic levitation setup has *N* layers of NdFeB permanent magnets in ONP configuration (four magnets in each layer) with a piece of pyrolytic graphite acting as the levitating proof mass. The experiments were performed to study the static and dynamic behavior of the levitating masses that have variable parameterized geometries, under different magnetic field strengths obtained by varying the number of magnetic layers underneath. The static tests were performed using an optical laser displacement sensor (Keyence LK-G82). Dynamic tests were performed by applying a driving force by means of an electro-mechanical shaker (Tira TV51120), which simulated the vibrations of the environment. The shaker was driven with a sinusoidal force supplied by a function generator and a power amplifier (LDS model PA 100E). The open-loop excitation of the shaker was controlled by an acceleration sensor. The equilibrium levitating position of the proof mass in static conditions and the time-dependent displacement under dynamic conditions were measured by an optical laser displacement sensor (Keyence LK-G82) with a 50 kHz maximum sampling frequency and 0.2µm±0.05% accuracy. The complete testing setup and a close-up image of the levitating system attached stage are shown in Figure 4.2(a) & (b) respectively.

Table 4.1 Properties of the magnetic levitation system.

Description	Symbol	Value	Unit
NdFeB magnet length	w	20	mm
NdFeB magnet thickness	t_m	3	mm
NdFeB magnet layers	N	1-2-3	-
Pyrolytic graphite length	l	3-4-5-6-7-8-9-10-11-12-13-15-17-19-20	mm
Pyrolytic graphite thickness	t	0.3-0.5-0.7-0.9-1-1.1	mm

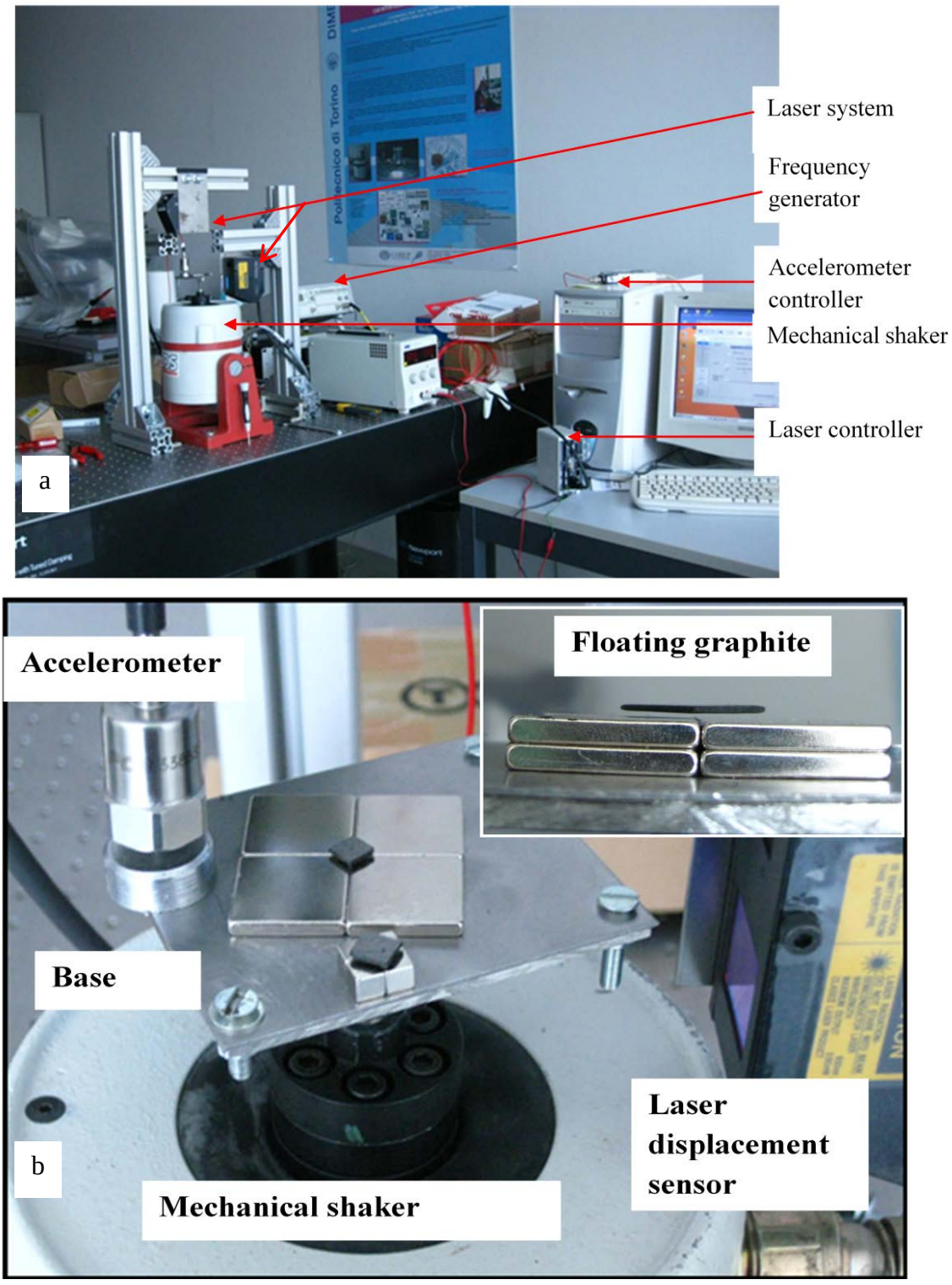


Figure 4.2 (a) Experimental set up for dynamic measurements of the levitating system. (b). Close-up view of the levitating system attached to the mechanical shaker. Inset of Figure 4.2 (b) shows the floating graphite proof mass.

4.3 Static Behavior of the Diamagnetic Levitation System

The static behavior of the levitation was investigated for various dimensions of the proof masses and magnetic strengths. The dimensions of the proof masses were systematically varied during the study. *System 1* consisted of PG square proof masses with constant t (= 1±0.1 mm) and variable length (l = 3-20 mm) and *System 2* consisted of PG square proof masses with constant l (=10 mm) and variable t ((= 0.3-1.1) ±0.1 mm) as given in the Table 4.1. Four square pieces of the NdFeB magnets arranged in an ONP configuration provided the magnetic field necessary for levitating the mass. The dimensions of the magnets were: length and width w = 20 mm and thickness t_m = 3 mm. The number of layers of the magnets were changed from N = 1, 2 and 3 to vary the magnetic field acting on the proof mass. All the levitation heights reported in this study were measured with respect to the surface of the magnets by a laser displacement sensor, placed directly above the proof mass and focused on the middle of the top surface of the proof mass.

The levitation height (z) measurement data with respect to the PG thickness (t) is shown in Figure 4.3. The levitating heights reported were given from the *Center of Mass* (CM) of the proof mass to the top surface of the magnet layer. The secondary axis of Figure 4.3 illustrates the air gap which is the distance between the bottom of the graphite proof mass and the top magnet layer. The graphs depict a linear relation between levitation height (z) and thickness (t) for the proof mass with constant l. Furthermore, Figure 4.3 and Figure 4.4 portray the magnetic field influence on the levitation height (z) addition to the PG geometrical parameters. The thickness increments add contributions to both magnetic and gravitational forces. Figure 4.3 reveals that the increments of thickness

produce a larger magnetic force than gravitational force ($\Delta F_{m,z} > \Delta F_g$), causing the center of gravity of the proof mass to elevate to a higher position. Furthermore, it provides verification that the diamagnetic graphite in fact generates a magnetic force and this induced force is proportional to the material volume of the proof mass.

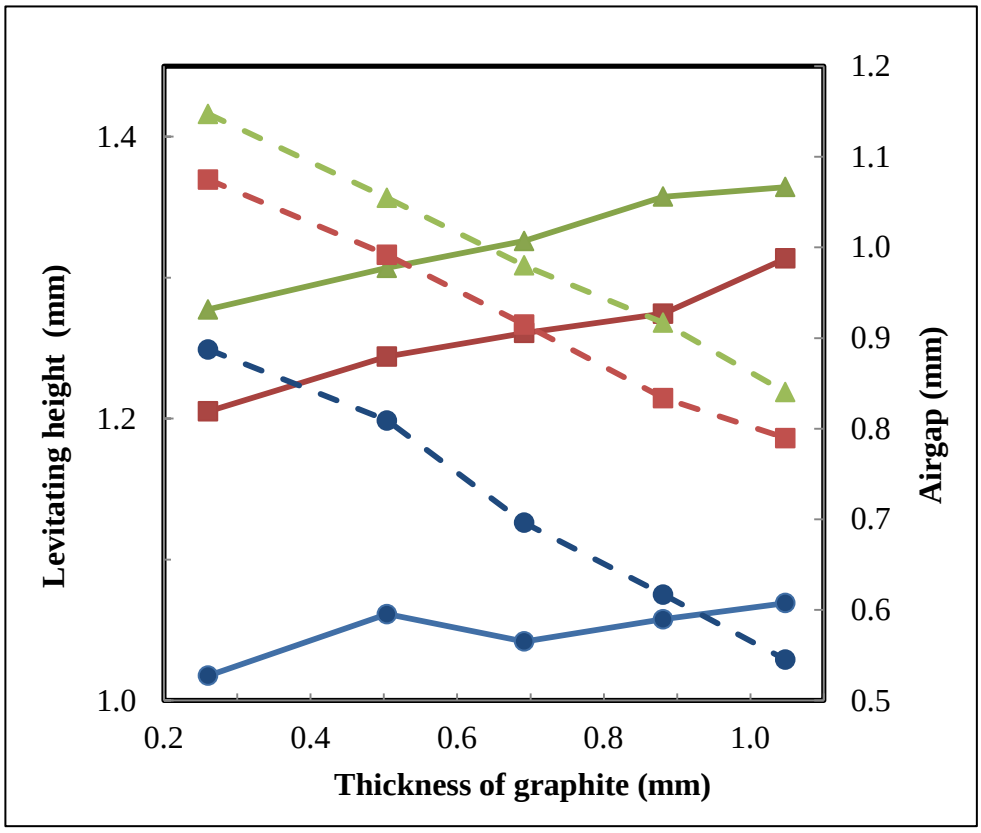


Figure 4.3 Levitation heights(Solid lines) and air gap(dotted lines) for various thicknesses of the proof mass and with one (●), two (■) and three (▲) layers of NdFeB permanent magnets.

Experimental results for similar characterizations conducted for proof masses with fixed thickness (t = 1 mm) and varying side lengths (l) are presented in Figure 4.4. The graphs show a non-linear relation between levitating height (z) and the length (l) of the square graphite masses, contrasting the linear relationship with thickness as seen in Figure 4.3. There is a significant difference in the levitating height of the l = 4 mm proof

mass compare to the l = 3 mm proof mass. The graphs show an increase in levitation height for the region, where l < 10 mm, while showing for l > 10mm a plateau, exhibiting the gravitational force increments due to the additional mass equaling the increments of magnetic force, i.e. $\Delta F_{m,z} \approx \Delta F_g$.

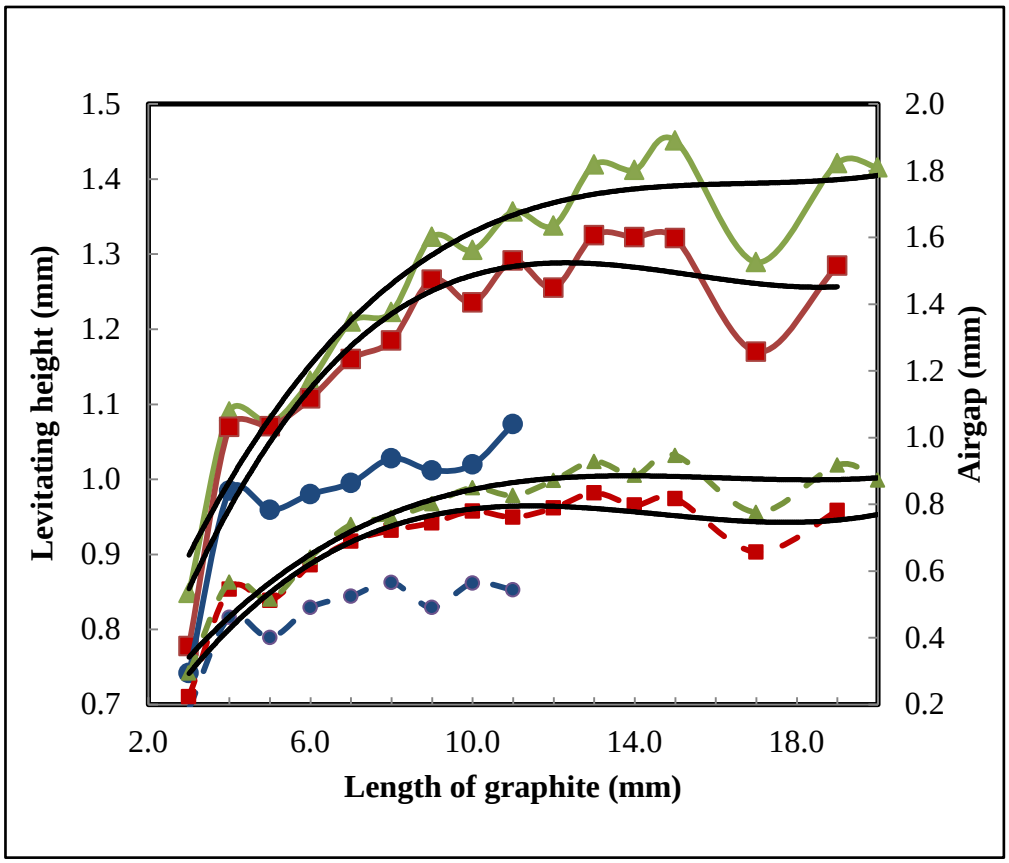


Figure 4.4 Levitating height (Solid lines) and air gap (dotted lines) of graphite vs. variable side lengths for one (●), two (■) and three (▲) layers of NdFeB permanent magnets.

This study reveals important information for device design. If a long dynamic range is desired, a thinner proof mass should be chosen: as seen in Figure 4.3, the levitation height increases less than 0.1 mm for the given thickness range, however the air gap increment is ~ 0.3 mm. Figure 4.4 shows that the optimized levitation height lies in

the l < 10 mm region. The device geometric parameters, thickness and length can be optimized from the information revealed in this study.

Steel is attracted to magnets. In order to see the influence of the steel attachment to the magnet in levitation height, the magnets were attached to 2 mm sheet of steel, and levitation height measurements were conducted. The experimental results in Figure 4.5 demonstrate that attaching magnets to steel can increase the levitation height. Moreover, the maximum length of the graphite proof mass able to levitate is larger when the magnet is attached to steel rather than plastic (a non-magnetic material). This can be a result of the increase of magnetic flux due to the induced magnetization of steel (soft ferromagnetic) by the permanent magnets.

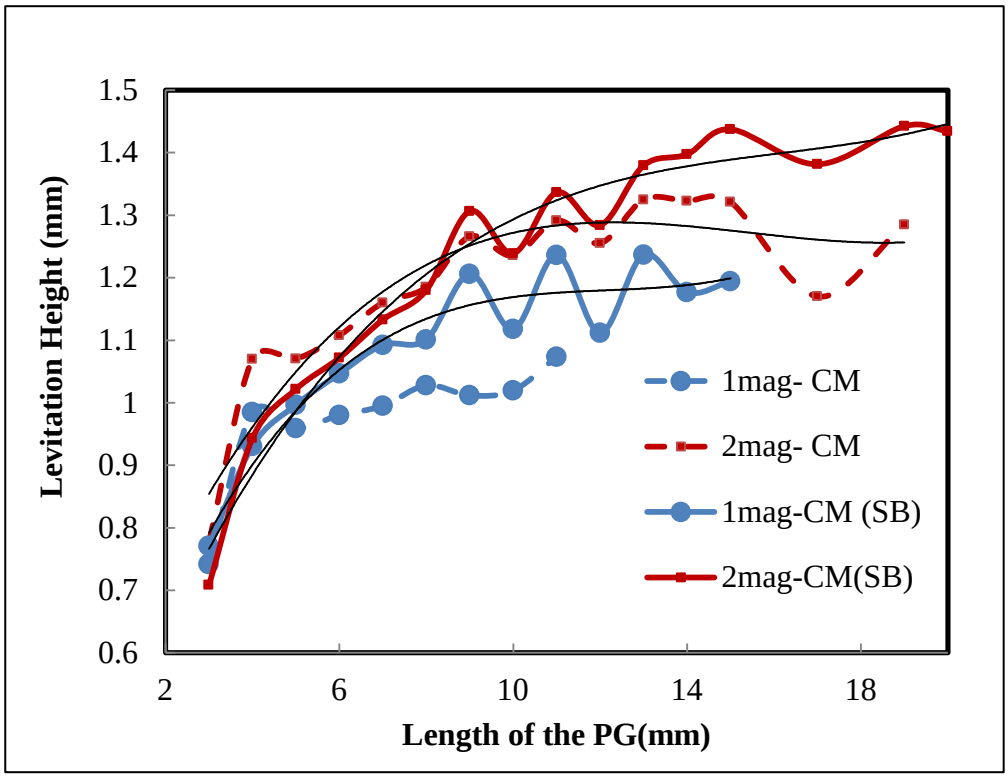


Figure 4.5 Levitation height vs. length of the PG mass for N=1 (●) and N=2 (■) layers of NdFeB permanent magnets. The dotted lines show when the magnets placed on a plastic base while the continuous line represents the height when the magnets are placed on a steel base (SB).

4.4 Dynamic Levitating System

Figure 4.2(a) shows the experimental set up used in frequency response measurements of the levitating system. Magnets were attached to a steel plate to increase the dynamic range. The steel plate with magnets was then fastened to the base (table) of the mechanical shaker. A sinusoidal force was applied vertically onto the base that holds the permanent magnets with the help of a mechanical shaker. Two laser displacement sensors were employed to measure the amplitude of vibration of the proof mass and the base. The laser of the one sensor head was focused on the base while the other on the proof mass; both the sensors were time synchronized. The applied force to the shaker was selected so that the proof masses have regular motions. The acceleration of the shaker was maintained at a constant magnitude to provide consistency between measurements. The shaker induced vibrations on both the levitating proof mass and the base. The dynamic response of the levitating mass during the *Sine Test* (i.e. one frequency at a time driving mode) was obtained by measuring the displacement of the mass from its static equilibrium position. The peak to peak amplitude variations were collected by a laser displacement sensor at each driving frequency starting from 0 Hz to 20 Hz. The procedure was repeated for different dimensions of the levitating masses.

The four forces acting on the levitating body while it vibrates are:

(1) Magnetic Force ($\boldsymbol{F_m}$): As the graphite mass moved downwards from the equilibrium position, the magnetic field experience increases. Hence the magnetic force also increases. The opposite happens when the graphite mass move in the upward direction.

(2) Force due to mechanical shaker (F_s): The force from the mechanical shaker was maintained constant by keeping its acceleration constant.

(3) Gravitation force of the graphite (F_g): This force acts downwards owing to its weight.

(4) Damping force (F_c): This force may have had two components, one air damping due to the movement of the graphite mass and the other arising from the interaction with magnetic field. There is a magnetic damping when a metal vibrate in a magnetic field [Tanaka 2001]. However, the effect on the pyrolytic graphite is unknown.

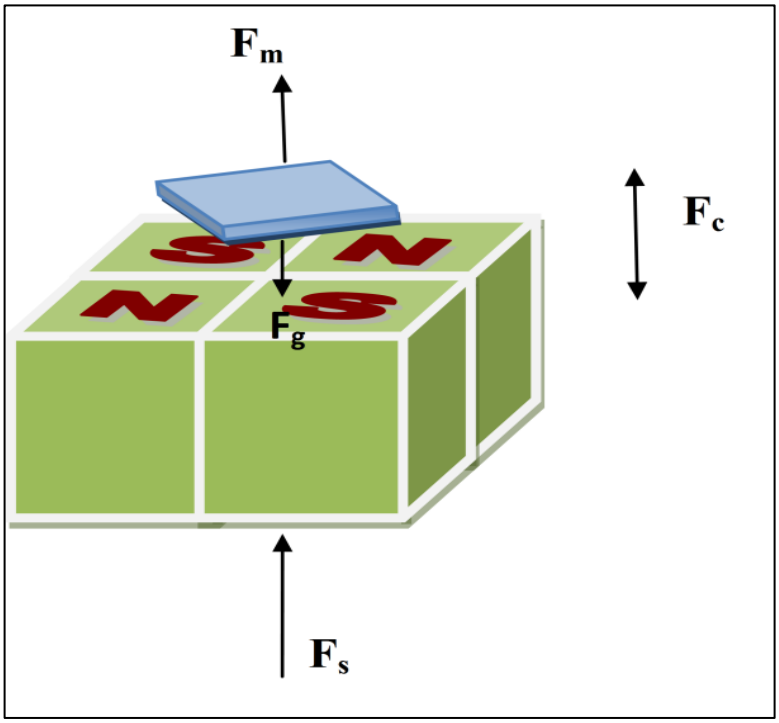


Figure 4.6 Forces acting on the levitating system during vibration.

As explained earlier, the time domain displacements of both the base and the proof masses were recorded through software that controlled the laser displacement sensors. Figure 4.7 and Figure 4.8 show the recorded waveform of the proof mass and

base, for frequencies of vibrations at 13 Hz (far away from the resonance frequency) and 17.4 Hz (at the resonance frequency), respectively. From the waveforms in Figure 4.7, it is evident that the base and the proof mass were vibrating in-phase with small amplitudes. As the frequency of vibration increased, the amplitude of vibration of the proof mass also increased rapidly and approached the maximum value at the resonance frequency. The proof mass and the shaker base started to vibrate out of phase as the frequency increased, reaching 90 degrees out-of- phase at the resonance frequency (See Figure 4.8) [Santuria 2002].

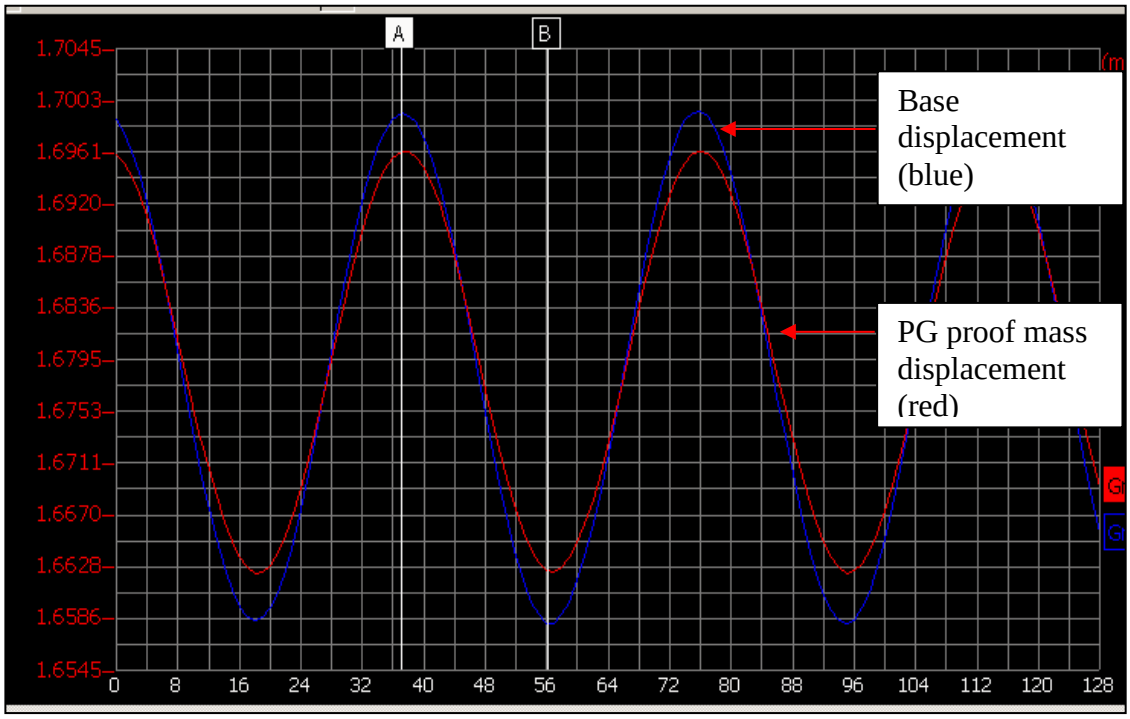


Figure 4.7 Time domain displacement of base and proof mass (9mm) for 13 Hz driving frequency. Amplitude of the graphs are not in same scale.

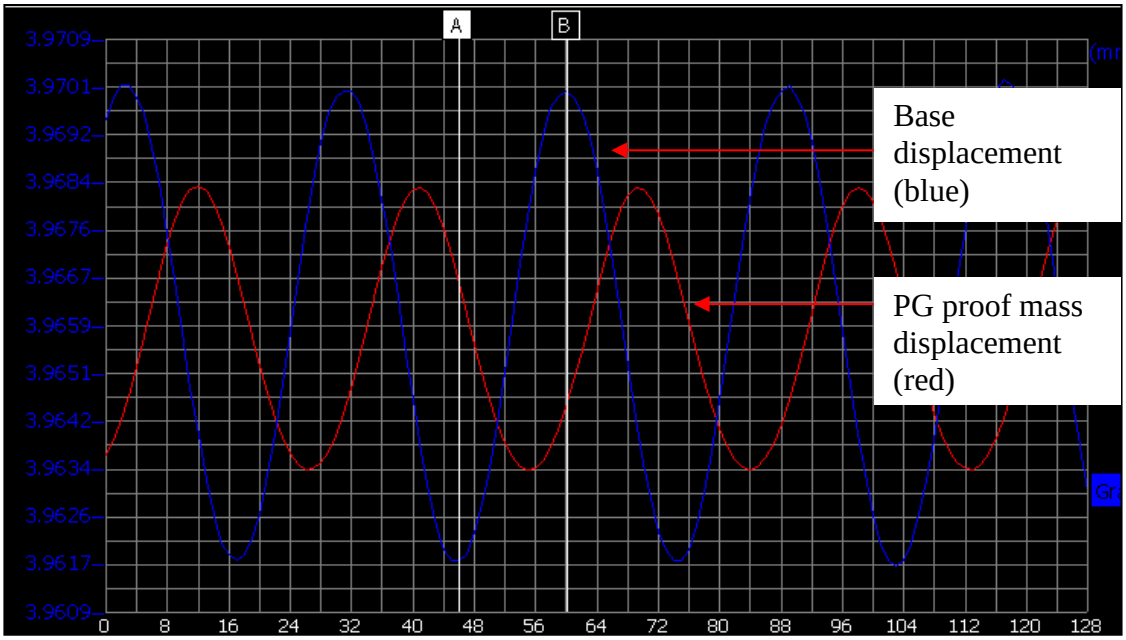


Figure 4.8 Time domain displacement of the base and the proof mass (9 mm) for 17.4 Hz driving frequency (note that the resonance frequency for a 9 mm proof mass is also 17.4 Hz). Amplitude of the graphs are not in same scale.

4.5 System Consisting of Fixed Thickness (*t*) and Variable Length (*l*) of Pyrolytic Graphite Proof Masses

Time domain peak-to-peak amplitude measurements were used to construct the frequency domain graphs for each specimen. The proof masses of dimensions lower than 8 mm were vibrating with large amplitude for the chosen applied force and hence displayed irregular motions. Therefore the experiments were confined to sizes above 8 mm in order to conserve the linearity of the vibrations. It was observed that the motion became more stable with an increase in the dimensions of the proof mass. The frequency domain vibration results are shown in Figure 4.9 , Figure 4.10 and Figure 4.11 for various graphite lengths (l = 9 to 20 mm) and for N number of layers of NdFeB magnets (N = 1, 2, 3). The l mm_N notation in the legend represents the length of the proof mass (l) in millimeters and the respective number of magnet layers (N) used for the measurement.

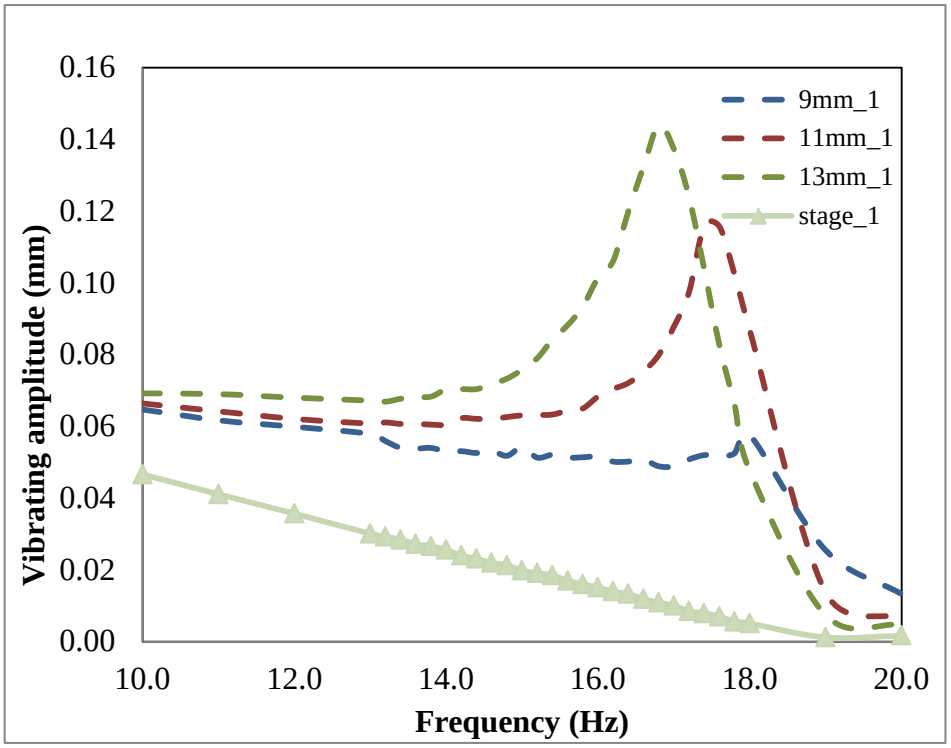


Figure 4.9 Frequency domain amplitude curves for pyrolytic graphite with variable length (*l*) under the influence of a single layer of magnets (*N* =1).

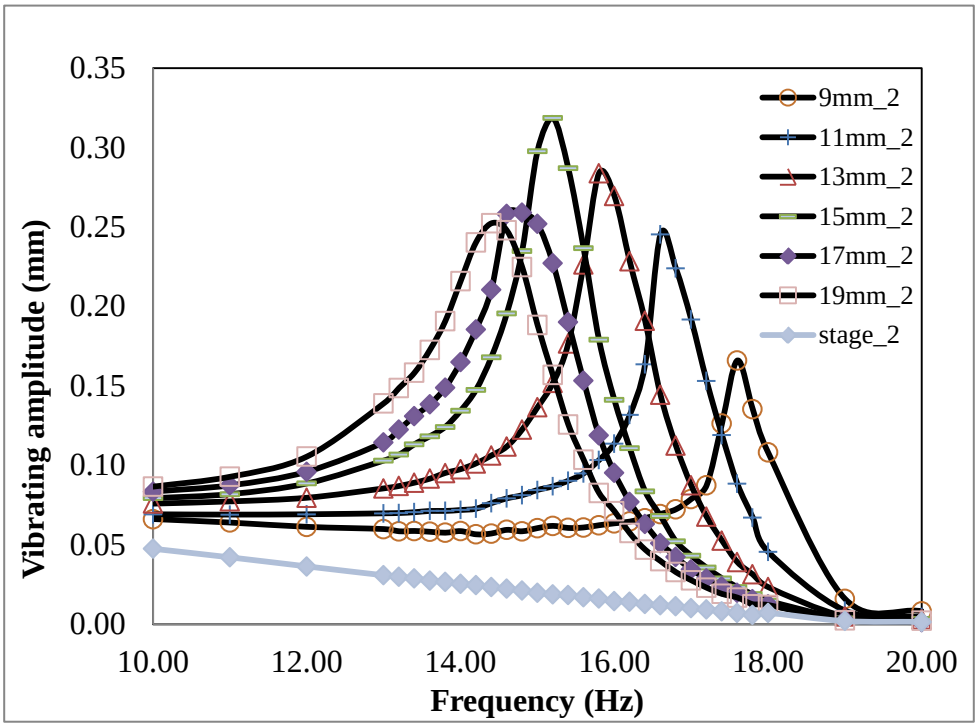


Figure 4.10 Frequency domain amplitude curves for pyrolytic graphite with variable length (*l*) under the influence of two layers of magnets (*N* = 2).

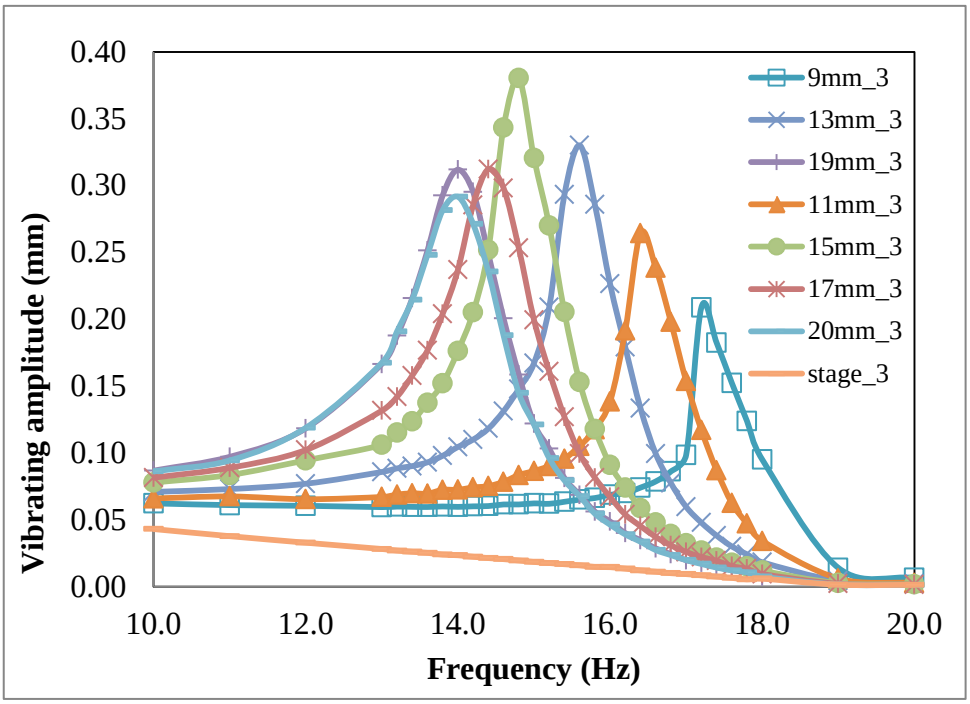


Figure 4.11 Frequency domain amplitude curves for pyrolytic graphite with variable length (l) under the influence of three layers of magnets (N = 3).

The stage amplitude change is also shown in the figures with 1, 2 and 3 notations representing the number of magnet layers (N). The amplitude of the levitating proof mass is the measurement taken relative to the base of the shaker. The absolute value cannot be measured since the frequency of the stage and graphite proof mass moves with a phase difference for some frequencies. As expected, the amplitude of the stage decreases as frequency increases in order to maintain the same driving force on the proof mass.

The resonance amplitude increases as the length (l) of the proof mass increases up to the l = 15 mm. An anomaly was noted when the size of the proof masses increased beyond 15mm: the resonance amplitude started to decrease instead of following the same trend. Moreover, the Full Width Half Maximum (FWHM) value of each graphs increased as the dimensions of the proof mass increased beyond 15 mm, showing an increase in the

resultant damping. This suggests that there is an optimum value for the length ratio between the proof mass and the magnets for the maximum amplitude of vibration of the system.

Figure 4.12 shows the frequency domain response of the l = 15 mm graphite proof mass for different strengths of the magnetic field obtained by varying the number of magnet layers (N = 1, 2 and 3). There is a clearly a shift in resonance frequency when the magnetic field increases. This observation is quite interesting and differs from the mechanically attached system where the frequency depends only on the mass and the spring constant of the system. This result shows that the virtual spring value is a function of the magnetic field in a magnetic levitation system and cannot be considered a constant like in mechanically attached non-magnetic systems. Additionally, Figure 4.12 shows the amplitude increase of the 15 mm specimen when the magnetic field is increased (by the means of N layers). However, amplitude cannot be compared between the system as the driving force can change due to additional masses added to the system (when N increases) despite maintaining a constant acceleration (Force = mass x acceleration).

A relation can be drawn between the length of the magnet and the length of the PG for the maximum amplitude: the diagonal length of the graphite is approximately equal to the length of a magnet (ratio a:c = 2:1). This condition is fulfilled when the PG corners are aligned at the middle of the magnet interface (i.e. c = a/2: Figure 4.13).

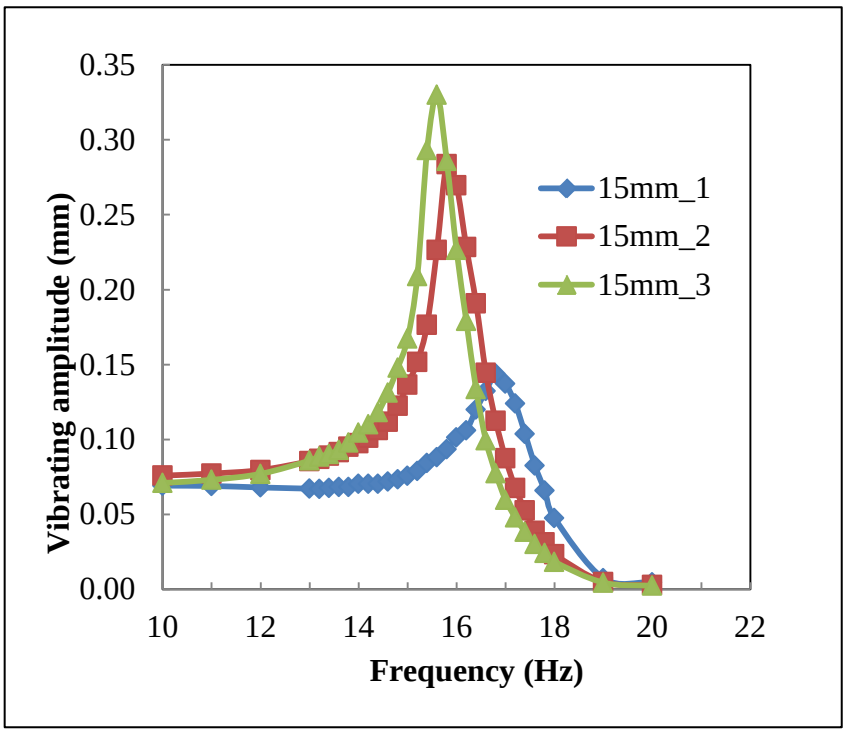


Figure 4.12 Amplitude curves for 15 mm Pyrolytic graphite under the influence of single (*N*=1), double (*N*=2) and triple (*N*=3) layers of magnets.

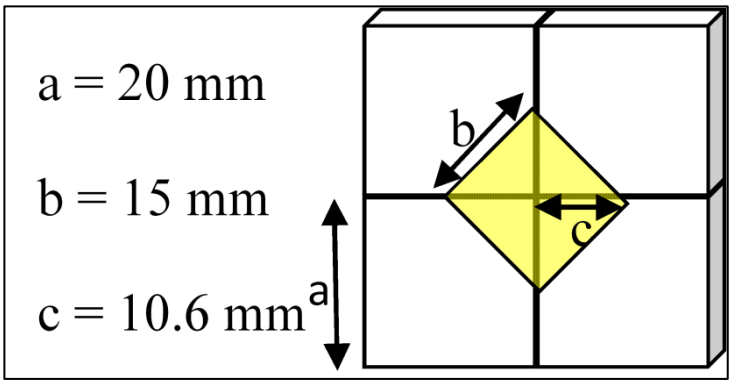


Figure 4.13 The 15 mm proof mass position on the ONP magnet arrangement.

The resonance frequency (f_0) (i.e. the frequency where the maximum vibration amplitude occurs) obtained from the graphs in Figure 4.9, Figure 4.10 and Figure 4.11 were used to calculate the approximate stiffness (spring value) for each proof mass. In this calculation influences due to the magnetic field were neglected. Table 4.2 provides

values while Figure 4.14 provides a graphical representation of resonance frequency and stiffness for the various graphite proof masses. The resonance frequency for the N =1 case is limited up to l =13 mm as the other proof masses did not stably levitate. Table 4.3 shows the experimental results obtained for more proof masses (l = 9, 10, 11, 12, 13 and 14 mm) in a different set of experiments. These two sets of measurement exemplify the accuracy of the resonance frequency measurements.

Table 4.2 Resonance frequency and stiffness of graphite proof masses (l = 9-20 mm).

Graphite length l (mm)	**Resonance frequency f_0 (Hz)**			**Stiffness k (N/m)**		
	***N*=1**	***N*=2**	***N*=3**	***N*=1**	***N*=2**	***N*=3**
9	18.1	17.6	17.3	2.4	2.3	2.2
11	17.5	16.7	16.4	3.4	3.1	3.0
13	16.8	15.8	15.6	4.1	3.6	3.5
15	Unstable	15.2	14.8	NA	4.5	4.3
17	Unstable	14.9	14.4	NA	5.7	5.3
19	Unstable	14.4	14.0	NA	6.6	6.2
20	Unstable	14.4	14.0	NA	7.8	7.4

Table 4.3 Resonance frequency and stiffness of graphite proof masses (l =9-14 mm).

Graphite length, l (mm)	**Resonance frequency f_0 (Hz)**			**Stiffness k (N/m)**		
	***N*=1**	***N*=2**	***N*=3**	***N*=1**	***N*=2**	***N*=3**
9	18.2	17.2	17.0	2.4	2.2	2.1
10	17.9	16.9	16.6	2.5	2.3	2.2
11	17.5	16.4	16.2	3.4	3.0	2.9
12	17.2	16.0	15.7	3.4	3.0	2.9
13	16.8	15.7	15.3	4.1	3.5	3.4
14	16.4	15.2	15.0	4.8	4.2	4.0

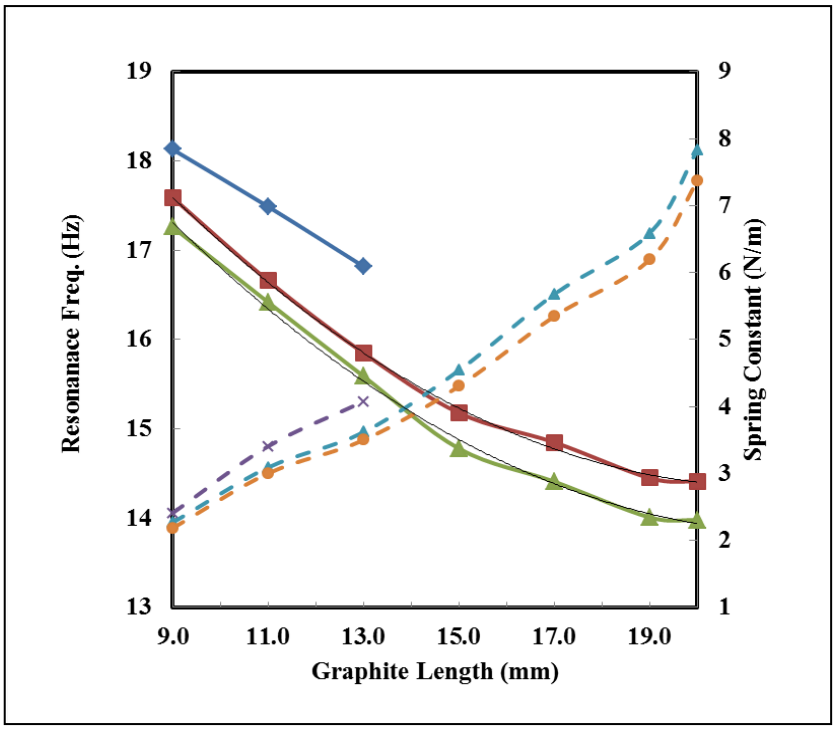


Figure 4.14 Resonance frequency (solid line) and spring value variation (dotted lines) for one (●), two (■) and three (▲) layers of NdFeB permanent magnets.

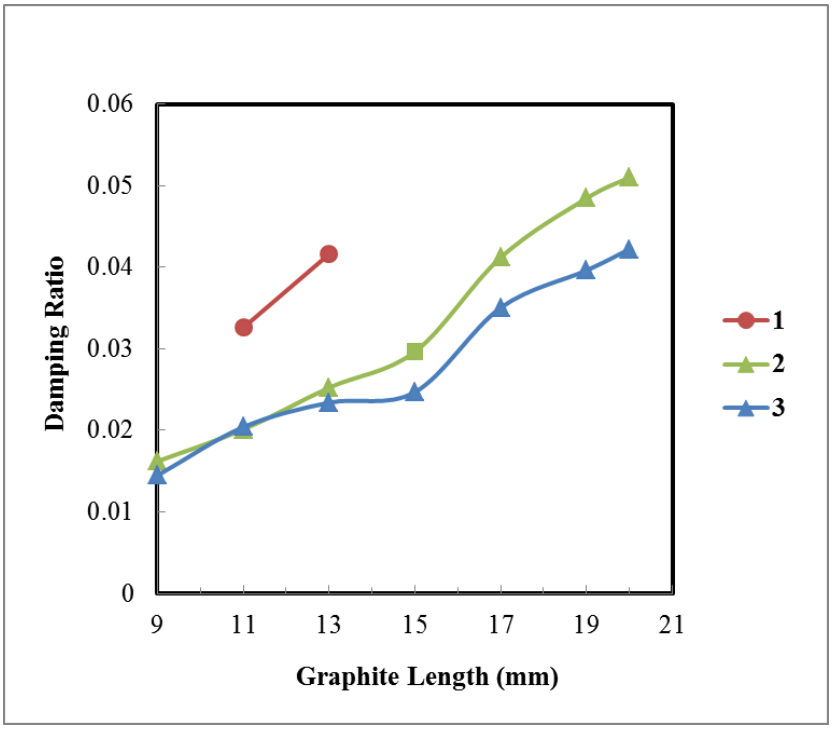


Figure 4.15 Damping ratio values obtained for vibration of different graphite size for influence of one (●), two (■) and three (▲) layers of NdFeB permanent magnets.

The damping ratio (ζ) is given by,

$$\zeta = \frac{\gamma}{2f_0} \tag{4.1}$$

where γ and f_0 represent the band width and resonance frequency, respectively. Figure 4.15 shows the calculated damping ratio for the different sizes of PG proof mass.

4.6 System Consisting of Fixed Length and Variable Thicknesses of Pyrolytic Graphite Proof Masses

The procedure described in *section 4.4* was followed to find the frequency response of the proof masses with various thicknesses and fixed length (l= 10 mm). Figure 4.16, Figure 4.17 and Figure 4.18 show the frequency domain amplitude curves for the proof masses under the influence of N (=1, 2 and 3) layer magnets. The legend shows the proof mass thickness belonging to the relevant amplitude graph.

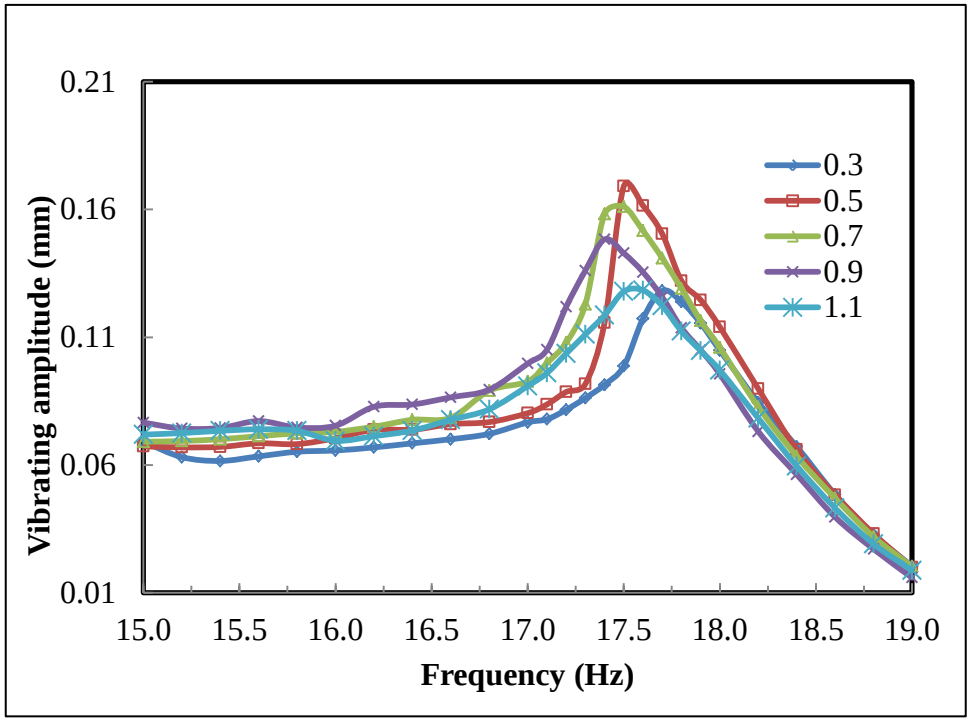


Figure 4.16 Frequency domain amplitude curves for pyrolytic graphite with various thicknesses under the influence of a single magnet layer (N=1).

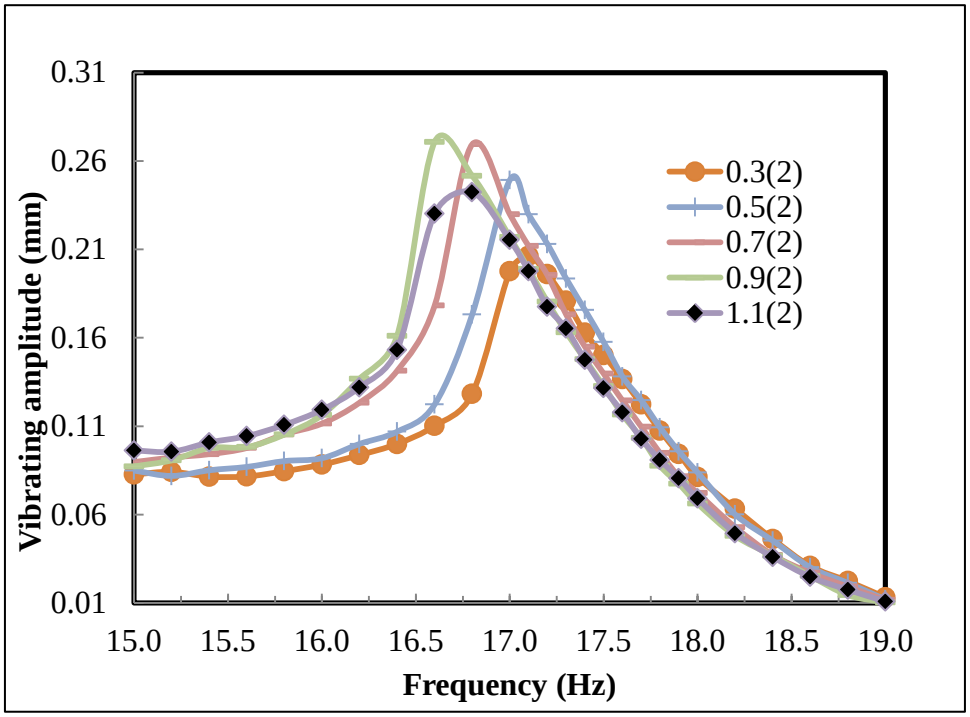


Figure 4.17 Frequency domain amplitude curves for pyrolytic graphite with various thicknesses under the influence of two layers of magnets (N=2).

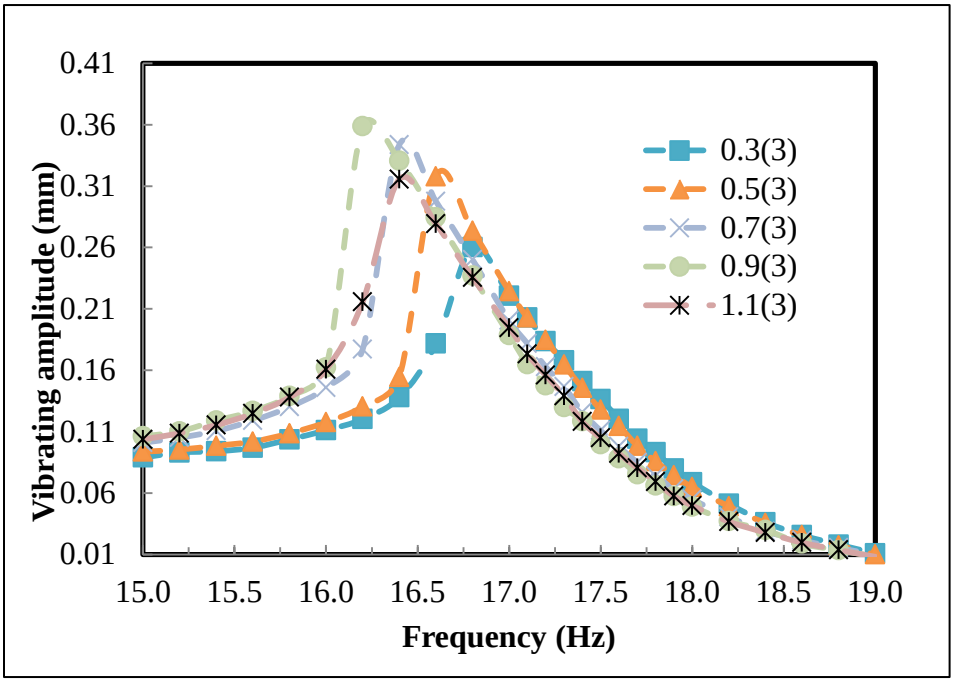


Figure 4.18 Frequency domain amplitude curves for pyrolytic graphite with various thicknesses under the influence of three layers of magnets (N=3).

Resonance frequencies and spring values obtained from the experimental frequency response graphs are given in Table 4.4; the graphical representation is shown in Figure 4.19. The thickness of the pyrolytic graphite was observed to have a non-linear relation to the resonance frequency and a linear relation to the spring values.

Table 4.4 Resonance frequency and stiffness of graphite proof masses (t = 0.3-1.0 mm).

Graphite thickness t (mm)	**Resonance frequency f_0 (Hz)**			**Spring values k (N/m)**		
	***N*=1**	***N*=2**	***N*=3**	***N*=1**	***N*=2**	***N*=3**
0.2603	17.71	17.08	16.82	0.71	0.66	0.64
0.5046	17.53	17.00	16.64	1.35	1.27	1.21
0.6917	17.45	16.83	16.44	1.83	1.70	1.62
0.8813	17.41	16.65	16.26	2.32	2.12	2.02
1.0479	17.55	16.72	16.43	2.80	2.54	2.46

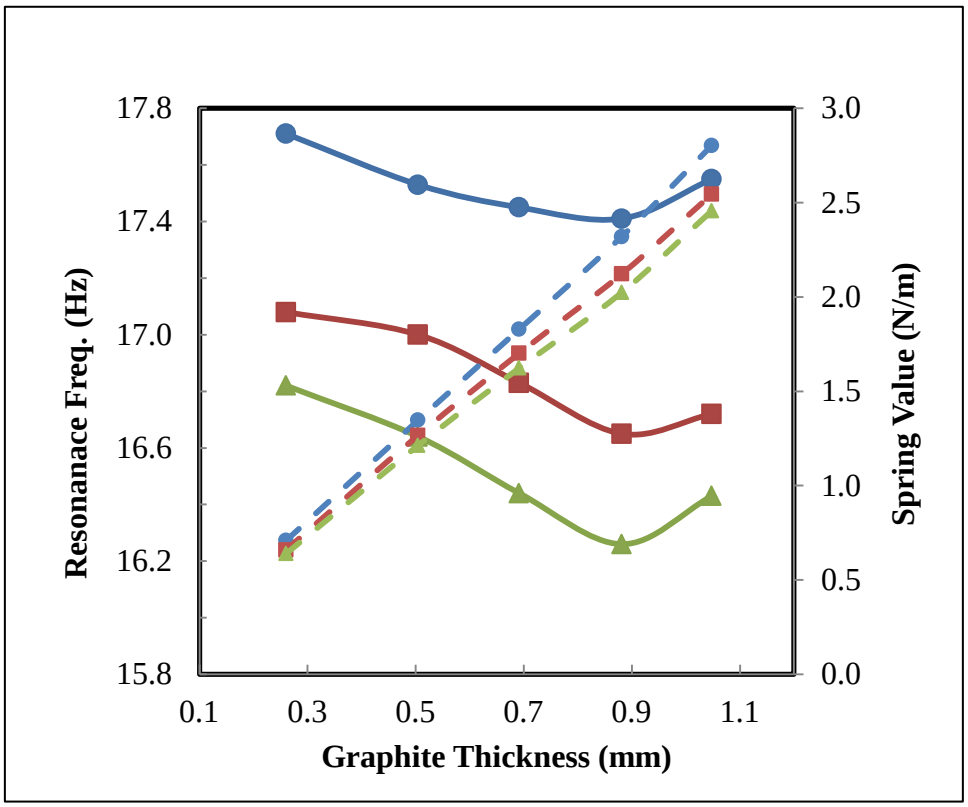


Figure 4.19 Resonance frequency (solid lines) and spring value variation (dotted lines) for one (●), two (■) and three (▲) layers of NdFeB permanent magnets.

4.7 Qualitative Study on 5mm Magnets

Dynamic analysis was carried out for the magnet system with four 5 mm cubic magnets. As seen in Table 4.5, the resonance frequencies of PG proof masses of this system are comparable to the levitating system comprised of four 20 x 20 x 3 mm magnets. This shows the possibility of scale reduction of the magnets without compromising the characteristics of the dynamic response. Evidently the maximum size of the graphite that can levitate is smaller than that of the 20 x 20 x 3 mm system.

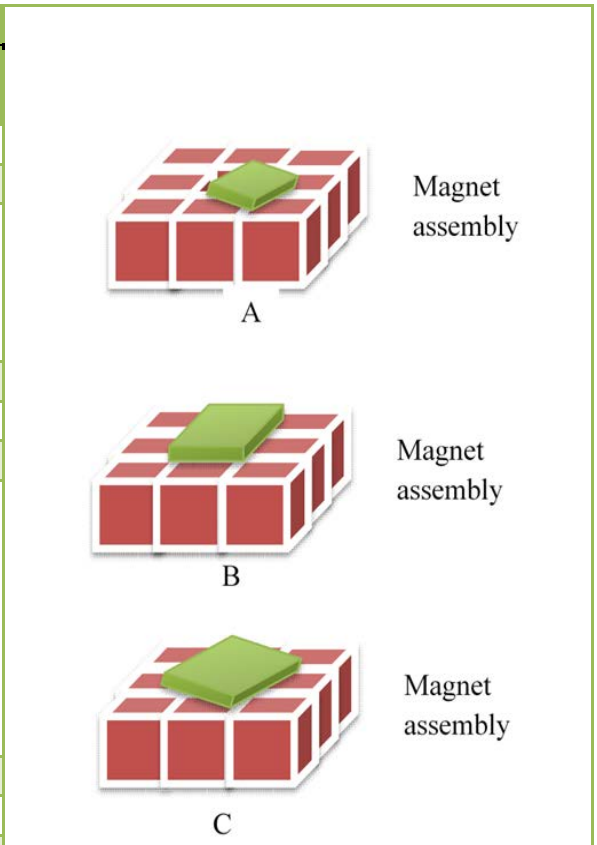
Table 4.5 Comparison between ONP systems of two different magnet sizes.

PG length, *l* (mm)	**PG thickness, t ±0.1(mm)**	**Magnet size (20x20x3mm)**	**Magnet size (5x5x5mm)**
		Resonance freq. (Hz)	**Resonance freq. (Hz)**
3	1	27.8	27.5
4	1	24.8	24.5
5	1	23.1	23.5
6	1	21.8	21.5
7	1	20.8	not stable
8	1	19.9	not stable

Levitation height studies of nine magnets that are in ONP configuration were carried out. As shown in Table 4.6, graphite lengths starting from 4 mm were levitated on the top of the nine magnet configuration. The equilibrium levitation position and orientation changed as the size of the graphite increased. Diagram given as A, B and C in Table 4.6 illustrates the different equilibrium levitation configurations of graphite.

Table 4.6 Equilibrium levitation height and configurations of graphite proof masses on ONP nine magnets system.

Graphite dimension (mm)	Magnet dime. (5x5x5mm)	
	Air gap (mm)	Configuration
4x4x1	.6772	A
5x5x1	.6281	A
6x6x1	.4685	B
7x7x1	.4715	B
8x8x1	.4874	B
9x9x1	.5508	C
10x10x1	.5364	C
11x11x1	.7085	C



4.8 The Study of Experimentally Derived Motion-dependent Magnetic Forces

Motion-dependent magnetic forces are the key elements in the study of magnetically levitated system dynamics [Chen 1994]. The goal of this study is to derive the magnetic force of the diamagnetic material levitated by permanent magnets, when it oscillates. Parameters extracted from experimental results were used in analytical relations to obtain the magnetic force acting on the pyrolytic graphite, which is difficult to measure using a direct method. The method implemented in this section can be considered as an empirical method to quantify magnetic forces at different positions and oscillation conditions. The systems comprise of two layers of magnets (N = 2) and

different lengths (l = 9, 11, 15 and19 mm) of graphite proof masses with same thickness (t = 1 mm). The objectives of this study were:

(1) To understand the characteristics of motion dependent magnetic forces.

(2) To find the applicability of the motion equation that was developed for attached systems to non-attached systems such as magnetic levitation.

(3) To use the knowledge gained from this experiment for designing vibration-based levitating devices.

The calculation procedure was carried out as follows:

(1) As discussed in *Chapter 3*, a time dependent motion equation can be written as,

$$Z(t) = A\cos(\omega t - \varphi) \tag{4.2}$$

where the amplitude (A) and phase angle (φ) are given by relations,

$$A = \frac{F_{Tot}/m}{\sqrt[2]{(\omega_0^2 - \omega^2)^2 + \gamma^2\omega^2}} \tag{4.3}$$

$$\tan\varphi = \frac{\gamma\omega}{(\omega_0^2 - \omega^2)} \tag{4.4}$$

Figure 4.20 illustrates the sketch of a characteristic frequency response graph for a damped linear oscillator. The magnetic damping (γ) was calculated from the experimental graph for each graphite proof mass. Similar to shown in the Figure 4.20, the resonance frequency (f_0) where the amplitude is maximum was obtained from the measurement graphs. The measured resonance frequency (f_0) and γ were used to calculate φ using equation 4.4. Then the force $F_{tot} - F_g$ value was changed until the

amplitude (A), which was calculated from equation 4.3 matched the amplitude obtained from the experimental method.

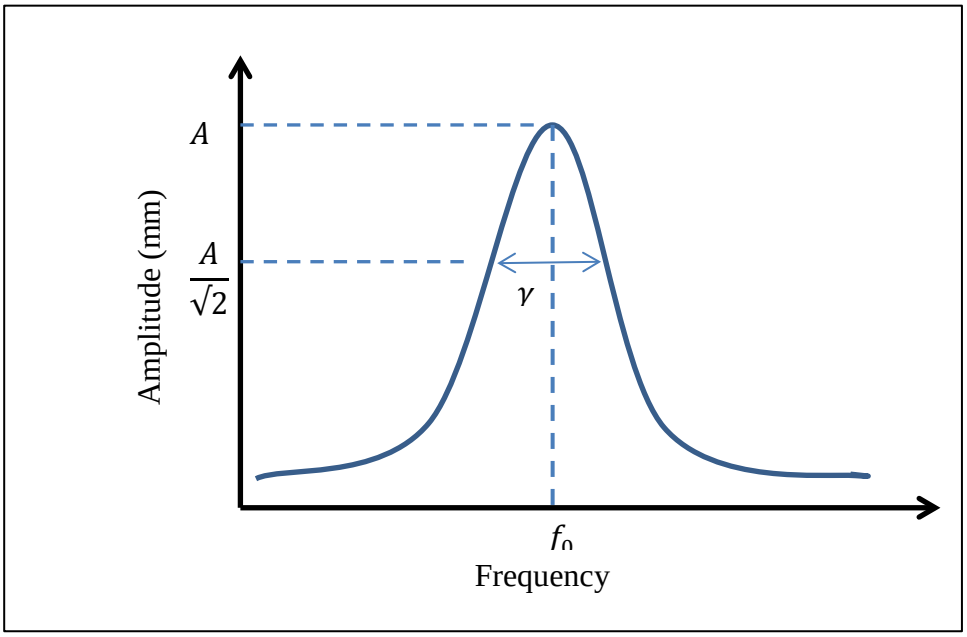


Figure 4.20 Frequency response graph of damped linear oscillator.

The net force acting on the graphite proof mass was,

$$F_m + F_s + F_g + F_c = F_{Tot} \qquad 4.5$$

where F_{Tot} is the resultant total force and F_g is the gravitational force (weight) of the proof mass. The magnetic force and damping force is given by F_m and F_c respectively. F_s is the force applied by the shaker.

A portion of the calculation process is shown in Table 4.7 for the 15 mm length graphite proof mass at f = 15 Hz. This procedure was carried out to calculate force $F_{tot} - F_g$ for all the data points shown in Figure 4.23 and Figure 4.24.

Table 4.7 Calculation of force F_{tot} -F_g by analytical equation for l = 15 mm proof mass at f = 15 Hz.

Time (s)	**Freq. (Hz)**	**Force (F_{tot}-F_g) (N)**	**γ**	**Tan φ (rad)**	**Arctan φ**	**A 10^{-4}(m)**	**Z(t) 10^{-4} (m)**
0.005	200.00	0.0048	7.60	-7.58	-1.44	-2.20	0.73
0.01	100.00	0.0048	7.60	-7.58	-1.44	-2.20	1.59
0.015	66.66	0.0048	7.60	-7.58	-1.44	-2.20	2.11
0.02	50.00	0.0048	7.60	-7.58	-1.44	-2.20	2.16
0.025	40.00	0.0048	7.60	-7.58	-1.44	-2.20	1.74
0.03	33.33	0.0048	7.60	-7.58	-1.44	-2.20	0.95
0.035	28.57	0.0048	7.60	-7.58	-1.44	-2.20	-0.06
0.04	25.00	0.0048	7.60	-7.58	-1.44	-2.20	-1.05
0.045	22.22	0.0048	7.60	-7.58	-1.44	-2.20	-1.81
0.05	20.00	0.0048	7.60	-7.58	-1.44	-2.20	-2.18
0.055	18.18	0.0048	7.60	-7.58	-1.44	-2.20	-2.07
0.06	16.66	0.0048	7.60	-7.58	-1.44	-2.20	-1.51
0.065	15.38	0.0048	7.60	-7.58	-1.44	-2.20	-0.63
0.07	14.28	0.0048	7.60	-7.58	-1.44	-2.20	0.40
0.075	13.33	0.0048	7.60	-7.58	-1.44	-2.20	1.34
0.08	12.50	0.0048	7.60	-7.58	-1.44	-2.20	1.98
…	…	--	--	---	---	---	---

(2) The goal is to reconstruct the time dependent graphite motion by the analytical method. Graphite displacement (Z) with respect to time can be calculated using the equation given in 4.2 using φ obtained by substituting experimental values to equation 4.4. In this calculation quasi steady-motion of graphite was considered. i.e. force at the maximum amplitude was considered to be constant for the entire motion. Hence the magnetic force variation due to the magnet to graphite distance change during oscillation was neglected.

Figure 4.21 shows the time domain graphite displacements (Z) constructed using Table 4.7 for f =10 Hz and f = 15 Hz frequencies. The

force was assumed to be constant for the *Z* motion of the graphite for a particular driving frequency.

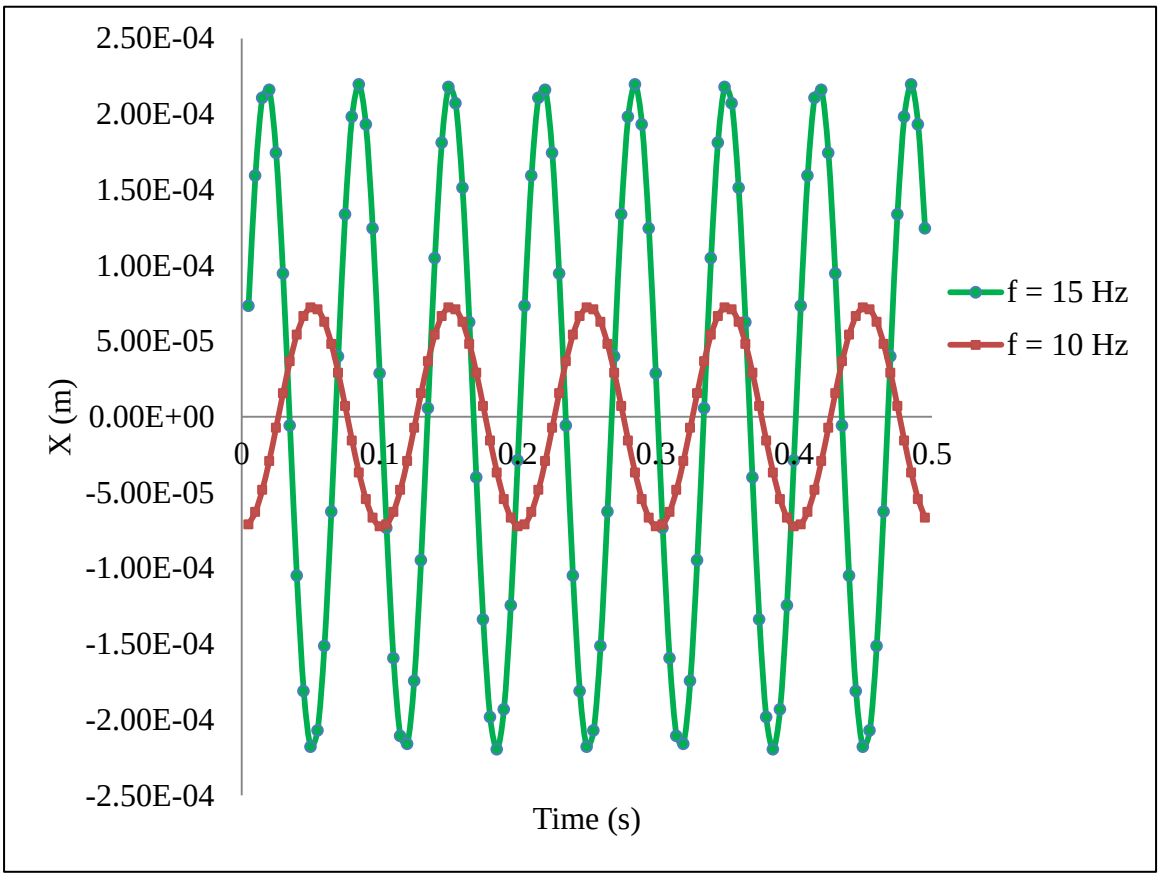


Figure 4.21 The displacement-time graph of a 15 mm pyrolytic graphite proof mass at *f* = 10 Hz and 15 Hz driving frequencies reconstructed by analytical equations using experimental parameters.

The frequency response of a 15 mm proof mass that were constructed by the analytical equation 4.2 and the experimental measurements are shown in Figure 4.22.

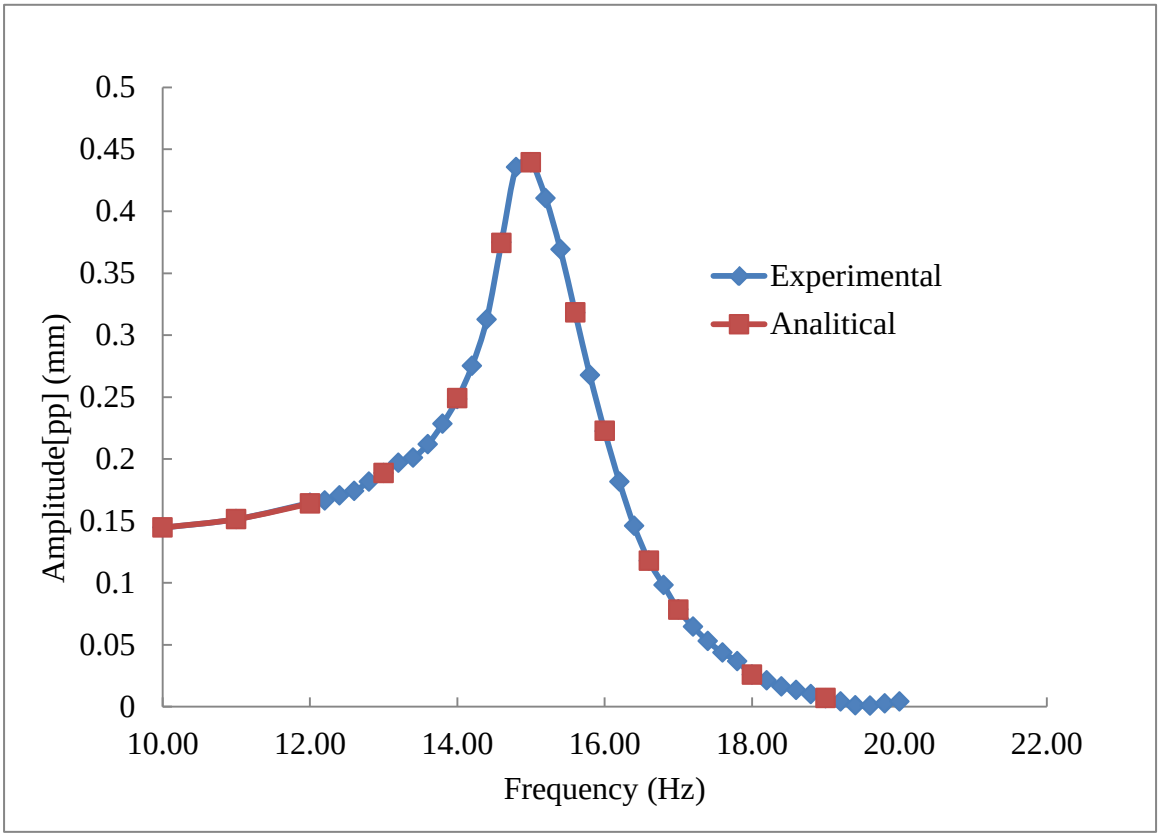
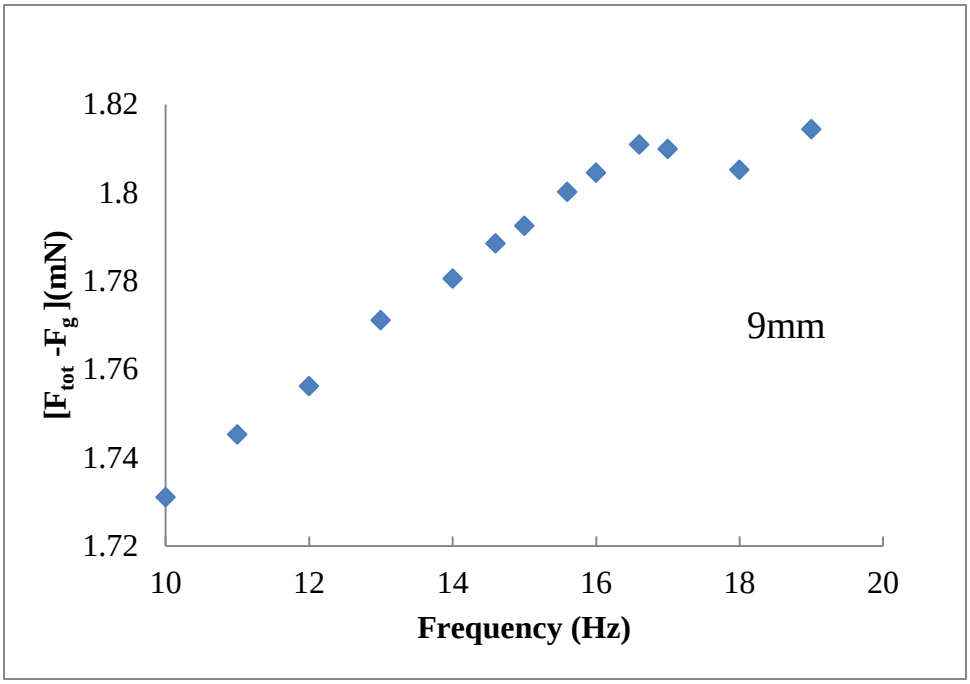


Figure 4.22 Frequency response of a 15 mm proof mass obtained by analytical method and experimental method.

Figure 4.25 shows the variation of force, $(F_{tot} - F_g)$ (extracted from experimental data applying to analytical equations) with respect to the frequencies. It was noted that closer to the resonance frequency, the force variation deviate from that of frequencies which are considerably far from the resonance frequency.



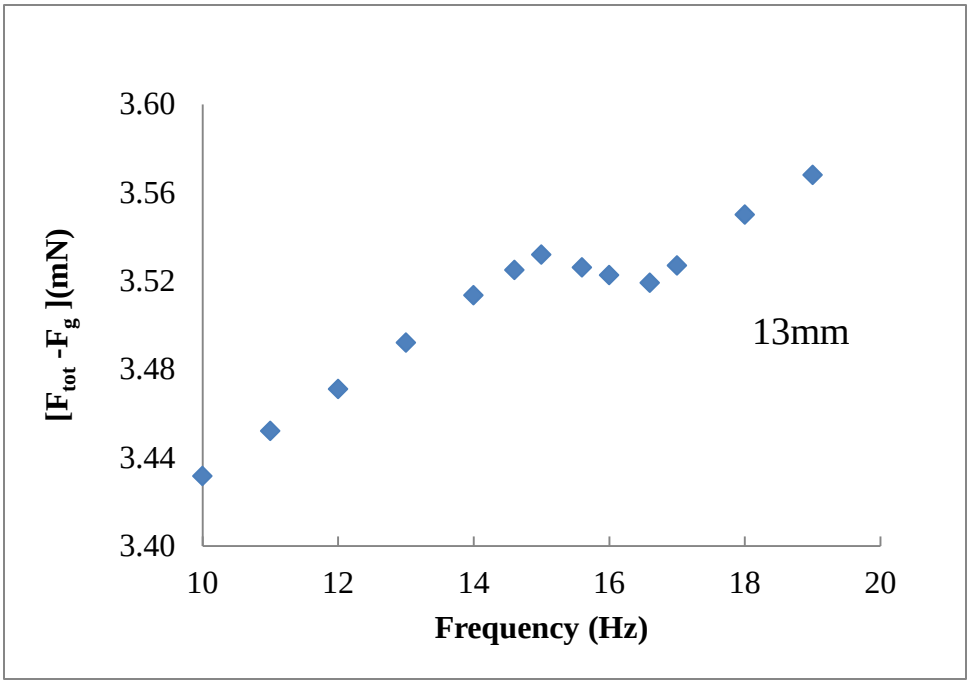
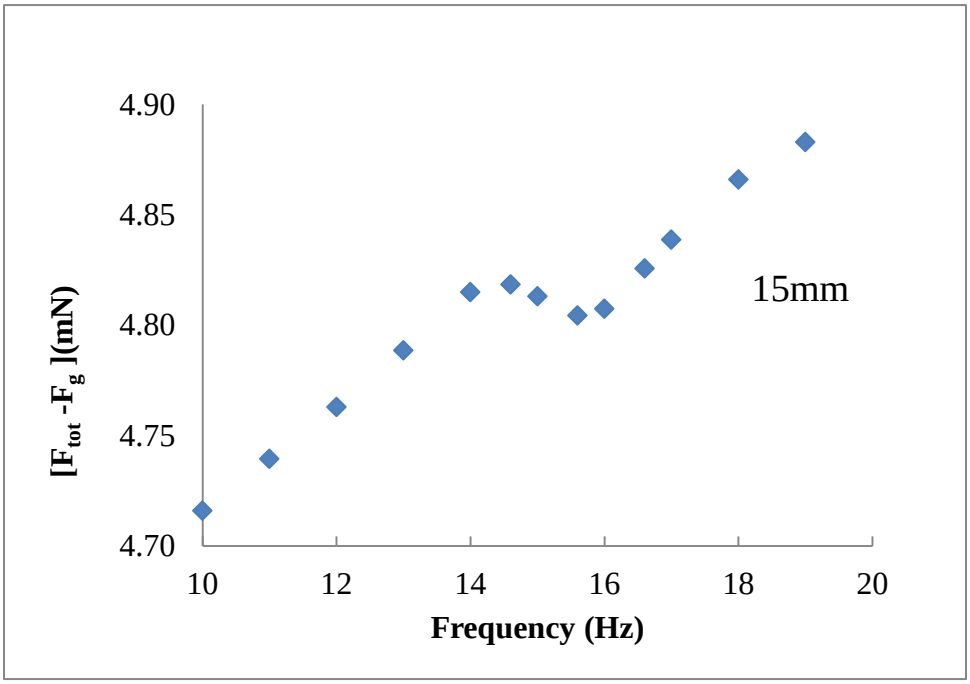


Figure 4.23 Force ($F_{tot} - F_g$) variation with frequency for *l* = 9 mm (top) and *l* = 13 mm (bottom) proof masses.



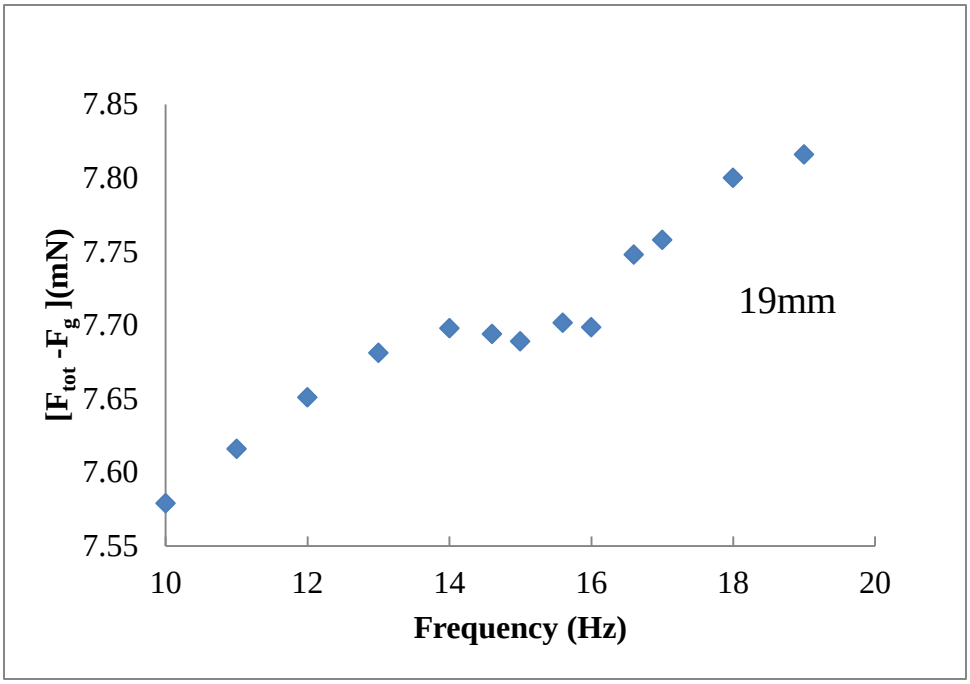


Figure 4.24 Force ($F_{tot} - F_g$) variation with frequency for *l* = 15 mm (top) and *l* = 19 mm (bottom) proof masses.

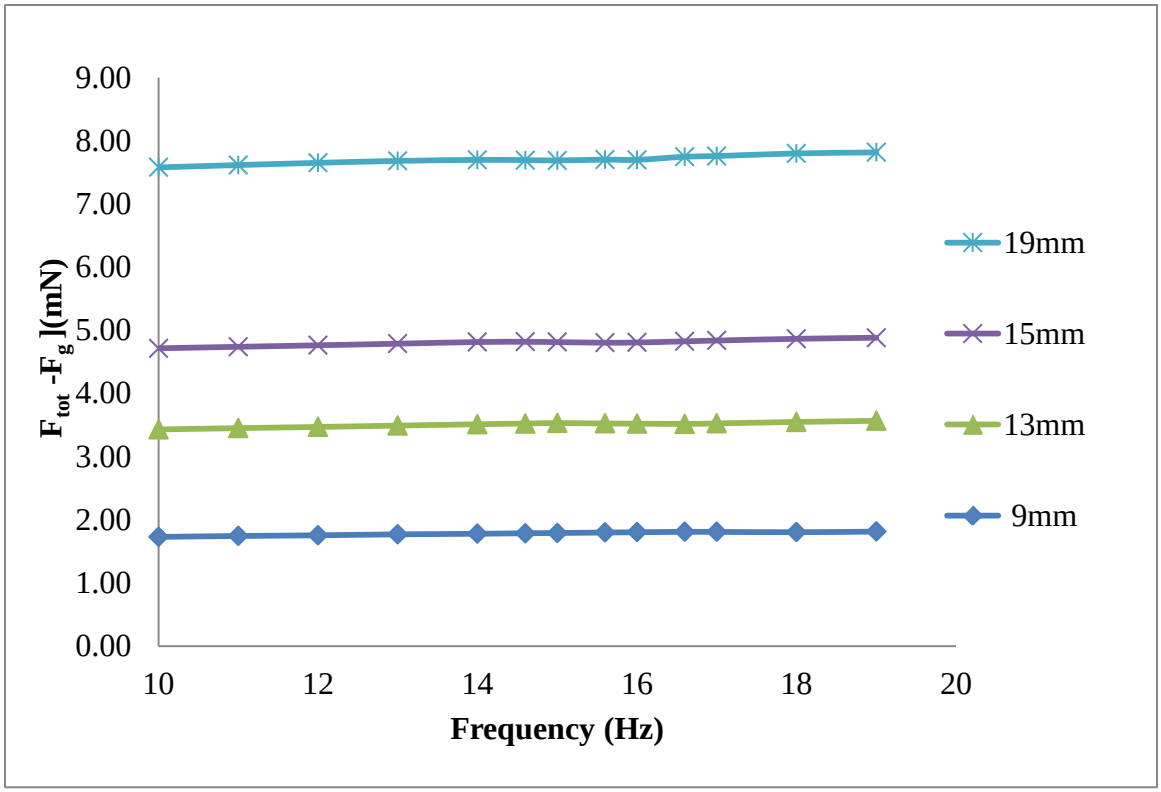


Figure 4.25 Force variation with frequency for *l* = 9, 13, 15 and 19 mm.

CHAPTER 5

FINITE ELEMENT MODEL FOR PERMANENT MAGNETS

In order to model the magnetic levitation, it is important to first accurately model the magnetic field distribution of permanent magnets, as the magnetic flux density is the one of two major governing parameters that defines the levitation and stability of the system. The analytical or semi-analytical modeling of the magnetic fields and forces produced by permanent magnets are difficult to establish, especially when coupled with other variables within a device. Thus, the development of a finite element method (FEM) model to obtain the magnetic field distribution of permanent magnets is of paramount importance. To accomplish this task, a 3D FEM model for the NdFeB magnet were developed using the information given in manufacturer's datasheet and experimentally verified with the aid of measurements obtained by a magnetometer. The framework of the developed model was employed to model ONP configuration and the simulation results were compared with experimental results. The experiments conducted for magnetic field mapping above the magnets in an ONP arrangement at different distance from the surface of the magnets also included.

5.1 Finite Element Method (FEM)

The finite element method is a numerical procedure used to analyze structures or systems when the problem being addressed is impossible or too complicated to be solved by classical analytical methods. In the FEM, the main structure is divided in to the small

size elements that connect back together by points called nodes. A collection of nodes make a grid called a mesh. This mesh is programmed to contain the material and structural properties. The differential (more often) or integral (less often) equations are applied piecewise to the elements that define how the structure will react to certain loading conditions. Computer software can used to simulate the mathematical relations that apply to each element. The concept of piecewise polynomial interpolation is used later to add all the elements together in order to interpolate the solution over the entire structure. It is important to know that the FEM method provides approximate solutions.

5.2 COMSOL AC/DC Module

The *AC/DC* Module in COMSOL commercially available software enables model and simulate electric and magnetic fields in static and low frequency applications, making it a perfect candidate for simulation requirements in this work. Also, the interfaces are fully multi-physics enabled, i.e. it is possible to couple an AC/DC model with any other interface in COMSOL *Multi-physics* to capture variables that influence other than electric or magnetic standalone effects to simulate more realistically. In order to simulate the diamagnetic levitation using the permanent magnet systems, *magnetic field no current* (mfnc) module in COMSOL *AC/DC* was used.

5.3 One Magnet Simulation and Verification of the Model

Figure 5.1 represents the geometry settings of the model that were developed to verify a one magnet simulation. The following sections illustrate the step-by-step procedure followed to develop the FEM model for the NdFeB magnet.

5.3.1 Partial Differential Equations (PDEs)

As there are no electric currents or variable charges present in permanent magnets, Gauss law and Maxwell's law equations simplify to:

$$\nabla \cdot \boldsymbol{B} = 0 \tag{5.1}$$

$$\nabla \times \boldsymbol{H} = 0 \tag{5.2}$$

where $\boldsymbol{B}$ is the magnetic flux density and $\boldsymbol{H}$ is the magnetic field. Since a permanent magnet has conservative fields, a scalar magnetic potential (V_m) can be introduced.

$$\boldsymbol{H} = -\nabla V_m \tag{5.3}$$

5.3.2 Geometry

Figure 5.1 represents the geometry of the model with a 20 x 20 x 3 mm NdFeB magnet surrounded by a 25 x 25 x 15 mm rectangular box, a 40 mm radius inner sphere, and a 50 mm radius outer sphere. The measurement box was introduced around the magnet with a finer mesh size to obtain highly resolved results near the magnet for comparison to experimental data. The domain defined between the 40 mm and 50 mm radius spheres represents the domain for which the infinite element boundary condition is applied. Domain 1 represents the commercially acquired Grade 45 NdFeB magnets used in this study while all other domains represent air.

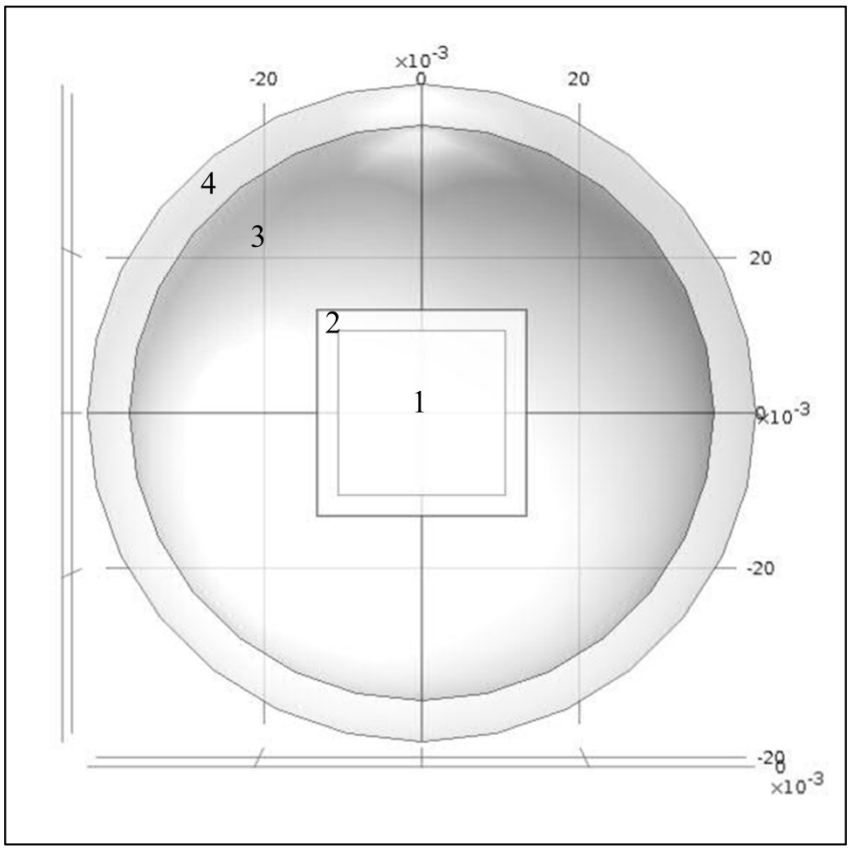


Figure 5.1 The 2D representation of the model geometry: 1) NdFeB magnet, 2) Measurement air box, 3) Inner air sphere and 4) Outer air sphere.

5.3.3 Domain Properties

The magnetic flux density of the NdFeB magnet and air domains were modeled using equations 5.4 and 5.5:

$$\boldsymbol{B} = \mu_0 \mu_r \boldsymbol{H} + \boldsymbol{B_r} \quad \text{for Ferro magnets} \qquad 5.4$$

$$\boldsymbol{B} = \mu_0 \boldsymbol{H} \quad \text{for air} \qquad 5.5$$

The equations 5.1 and 5.4 lead to defining:

$$\nabla \cdot \left(-\nabla V_m + \boldsymbol{B_r} / \mu_0 \mu_r \right) = 0 \quad \text{for Ferro magnets} \qquad 5.6$$

where $\boldsymbol{B_r}$ is the magnetic remanence and μ_r is a 3 x 3 matrix (5.7) representing the relative permeability of NdFeB.

$$\mu = \mu_0 \mu_r = \mu_0 \begin{bmatrix} \mu_{xx} & \mu_{xy} & \mu_{xz} \\ \mu_{yx} & \mu_{yy} & \mu_{yz} \\ \mu_{zx} & \mu_{zy} & \mu_{zz} \end{bmatrix} \quad 5.7$$

Often in literature, the relative permeability of NdFeB is given by a single scalar value (often as 1.05), which is related to the maximum relative permeability along the easy axis (i.e. preferred direction of magnetization) neglecting the perpendicular permeabilities. However, it is vital to use the perpendicular permeabilities to obtain accurate simulation results. The anisotropic permeability (i.e. permeability is different in different direction of the material) of sintered NdFeB magnets has been reported with permeability values parallel and perpendicular to the easy axis of about μ_{par} = 1.04 and μ_{perp} = 1.17 [Bahrdt 2011, Wang 1998]. μ_{perp} decreases with increasing coercivity: for magnets with a coercivity of about 1.8 T, μ_{perp} =1.17 and for magnets with a coercivity of about 3.2 T, μ_{perp} =1.12 [Katter 2005]. The magnets used in this study were made by the sintered method and have nominal magnetic remanence and coercivity values of 1.35 T and 1.20 T respectively. The NdFeB magnets were assumed perfectly magnetized along the z-direction and the μ_r tensor is symmetric. μ_r is a diagonal tensor if the x, y, and z coordinates are chosen along the principal axes [Prat-Camps 2012]. With this assumption, the components of the permeability can be set as $\mu_{zz} = \mu_{par}$, $\mu_{xx} = \mu_{yy} = \mu_{perp}$ with all other components being zero. All components in the magnetic flux density vector (B_x, B_y and B_z) are affected by an anisotropic permeability, μ ($= \mu_0 \mu_r$.) as given in equations 5.8, 5.9 and 5.10 [Fulani 2001].

$$B_x = \mu_{11} H_x + \mu_{12} H_y + \mu_{13} H_z \quad 5.8$$

$$B_y = \mu_{21}H_x + \mu_{22}H_y + \mu_{23}H_z \quad 5.9$$

$$B_z = \mu_{31}H_x + \mu_{32}H_y + \mu_{33}H_z \quad 5.10$$

According to the Arnold magnetics datasheet, the NdFeB magnets used in this study have a B_r range of 1.32 -1.38 T that results in μ_{par} varying between the range of 1.21-1.04 (calculated by (*dB/dH*) from the data given in the demagnetization datasheet). The nominal value of B_r = 1.35 T (μ_{par} = 1.12) along with the upper and lower limits of the B_r values were simulated and compared against the experimental results. μ_{perp} was kept at a reference value of 1.17 (Value obtained from literature that closely matched to the specification of magnets used in this study) for all the simulations [Chavanne 1989, Katter 2005].

5.3.4 Boundary Conditions

Prior to the development of infinite element boundary conditions, the common practice was to extend the unbounded domain to a sufficiently large distance from the simulation domain so that the influence of the terminating boundary conditions (BC) at the far end became negligible. This approach required immense computer power to preserve accuracy. Furthermore, it can make the geometry difficult to mesh due to large differences between the largest and smallest object.

There are two main considerations employed in setting up boundary conditions around the magnet in order to increase the accuracy of the model: 1) the exterior boundary needs to be chosen to be a sphere as the magnetic field is in circular form and 2) infinite elements need to be used to emulate the surrounding infinite open space. The first criterion is important as the boundary should be perpendicular to the field lines such that $\hat{\boldsymbol{n}} \cdot \boldsymbol{B} = 0$. All the internal boundaries of the model preserve the continuity of the

magnetic flux density such that $\hat{\boldsymbol{n}} \cdot \boldsymbol{B_1} = \hat{\boldsymbol{n}} \cdot \boldsymbol{B_2}$. Since magnetic fields extend towards infinity, using infinite elements in the model is more computationally efficient.

As the space around the permanent magnet systems obeys the Laplacian equation (equation 3.11), the surface of the interior 40 mm radius domain can be transformed via a conformal map to the exterior domain at infinity through the use of the infinite elements. In infinite element method, the model coordinates map from the local, finite-sized domain to a stretched domain. The theory behind the transformation is given as follows.

The two coordinate systems are related by,

$$r = r_0 + t_{\boldsymbol{inf}} \tag{5.11}$$

where r is the distance from where the origin of the geometry is drawn, r_0 is the new origin from where the coordinates are scaled (the boundary at inner sphere) and $t_{\boldsymbol{inf}}$ is the distance from the new origin to infinity.

$$t_{\boldsymbol{inf}} = t_p \left(\frac{\Delta_w}{\Delta_p - \gamma(t - t_p)} \right) \tag{5.12}$$

where t_p and Δ_p are the input parameters that represent the pole distance (calculated by the width between the two spheres), and the physical width of the infinite element region, respectively. The variable t is the unscaled coordinate along the width of the infinite element region (from the inner to the outer boundary), and Δ_w is the unscaled width of the region. The value γ is given by,

$$\gamma = 1 - \left(\frac{t_p}{\Delta_{pw} - t_p} \right) \tag{5.13}$$

The infinite physical width (Δ_p) of the scaled region can changed to a finite large value, (Δ_{pw}) to avoid solver issue. The Physical width (Δ_{pw}) parameter sets the modeled

width of the infinite element region, which typically is a large value. The default value is 1000 times the characteristic distance (dGeomChar) for the geometry. The parameter pole distance (t_p) is a tuning parameter that controls the nature of the coordinate transform. The default value is 5 times the average thickness (avgDelta). [COMSOL ACDC user guide, ver. 4.2a.]

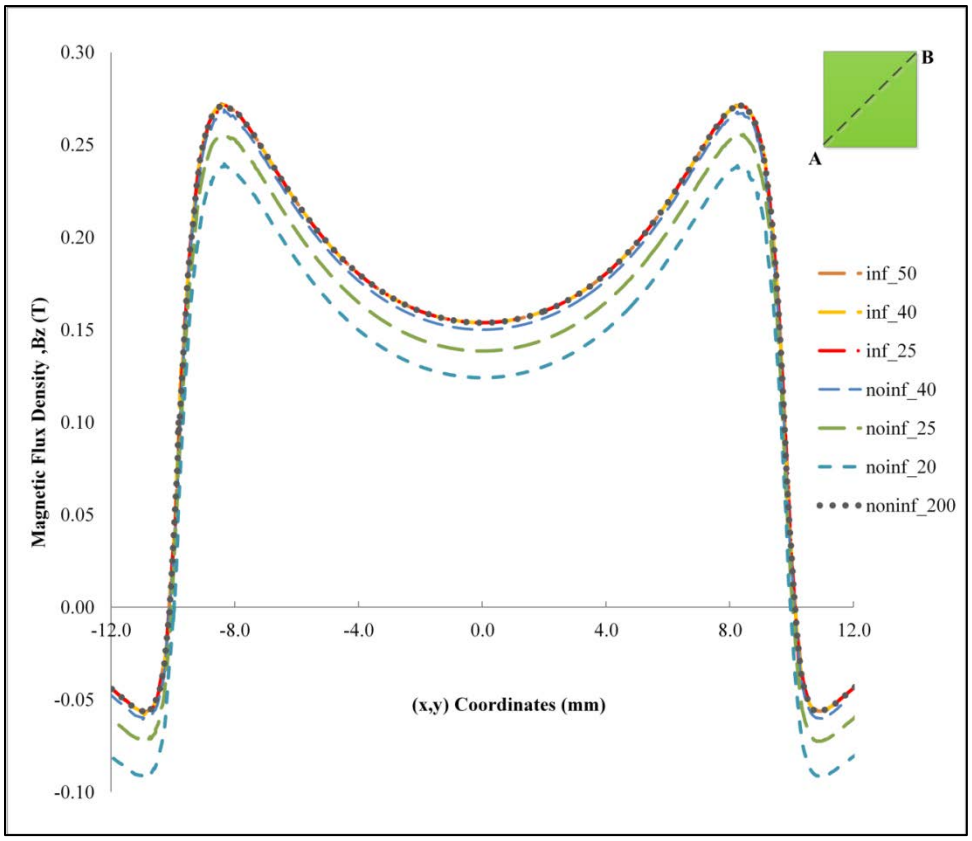


Figure 5.2 Comparison between the results of the model with infinite elements (*inf*) and without infinite elements (*noninf*): The numbers in the legend represent the radius of the outer air sphere.

Experimentally, $\boldsymbol{B}$ was measured to be 0.00 mT beyond 200 mm from the magnet. Due to this reason, simulations were performed with a BC of $\hat{\boldsymbol{n}} \cdot \boldsymbol{B} = 0$ at an outer sphere of radius 200 mm without using the infinite element method. Then, the infinite element method was applied setting the outer radius of a much smaller sphere. The

results obtained for outer spheres with different radius by the infinite element method and without the infinite element method are shown in Figure 5.2. As seen in the figure, the infinite element method applied results are comparable to the results of a 200 mm outer sphere without the infinite element method, with negligible differences. We can see a significant difference in simulation for the outer sphere with smaller radius, if the infinite element method was not employed (see Figure 5.2). Figure 5.2 shows that infinite elements can be placed as near to the source as desired as long as it is outside the area of interest, without compromising accuracy. A 40 mm inner radius was selected as an inner boundary for the henceforth developed models. The source (i.e. magnets) should be centered in the geometry for better results when the infinite element method is used [Zienkiewicz 1983].

5.4 Simulation Model Results for One Magnet

Figure 5.3 shows the surface plot of the simulated results of the magnetic flux density distribution in the *z*-direction (B_z) at 0.6 mm above the surface of the magnet in which the height represents the B_z corresponding to the position. At the corners of the magnet, B_z is greatest and decreases towards the middle as expected from theory.

As seen in Figure 5.4, B_z decreases as move further away from the surface of the magnet as expected. Further, the shape of the simulation results of Figure 5.4 matches with the analytical calculation done by Xiao-fan *et al.* for a magnet of closely matched dimensions [Xiao-fan 1994].

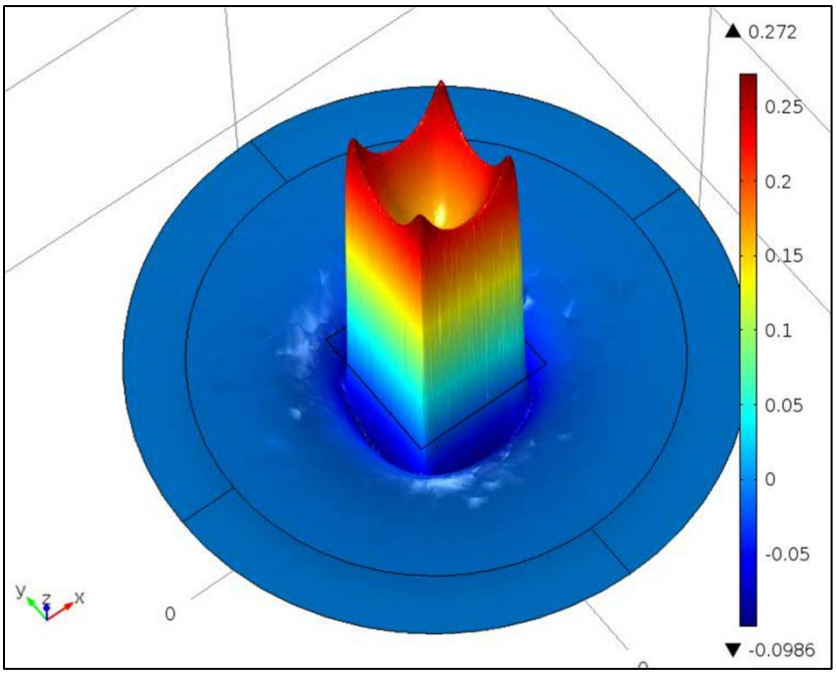


Figure 5.3 2D representation of the z-component of the magnetic flux density (B_z) distribution of the Grade 45 NdFeB magnet at 0.6 mm above the surface of the magnet.

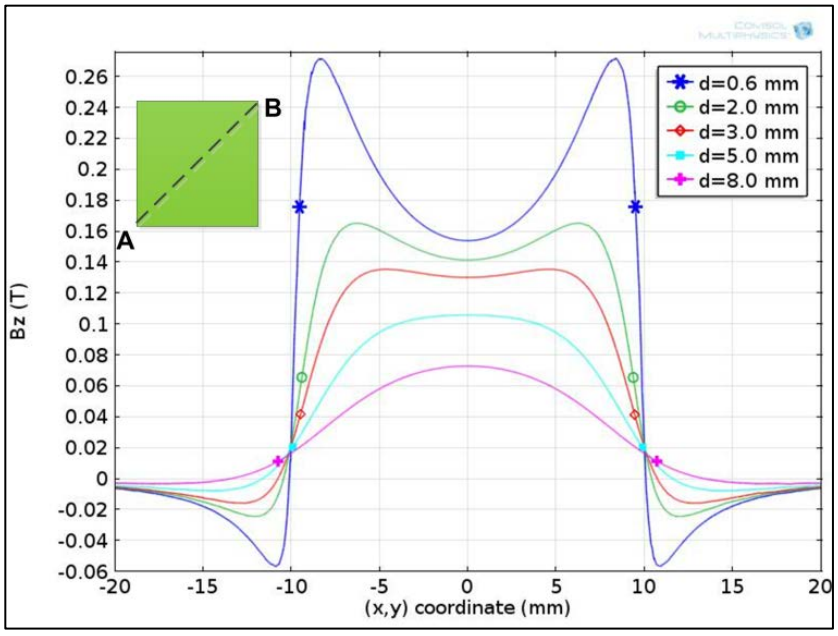


Figure 5.4 Simulated results of the distribution of B_z along the line *AB* at *d* distance above the surface of the magnet. A and B coners of the magnet are at (-10,-10) and (10,10).

5.4.1 Comparison of Simulation and Measured Results

Transverse magnetic flux density measurements were performed using a computerized *XYZ* stage (Newport M-460A, 0.2mm fine travel) and Hall probe Magnetometer (Lakeshore 410 with transverse probe, accuracy 2%). The distance from the magnet to the sensor was 0.6 ± 0.1mm. The measurements were obtained for two magnets, *Magnet 1* and *Magnet 2*. Flux measurements were performed along the *AB*, *CD* and *EF* lines as shown in the insets of Figure 5.5, Figure 5.6 and Figure 5.7.

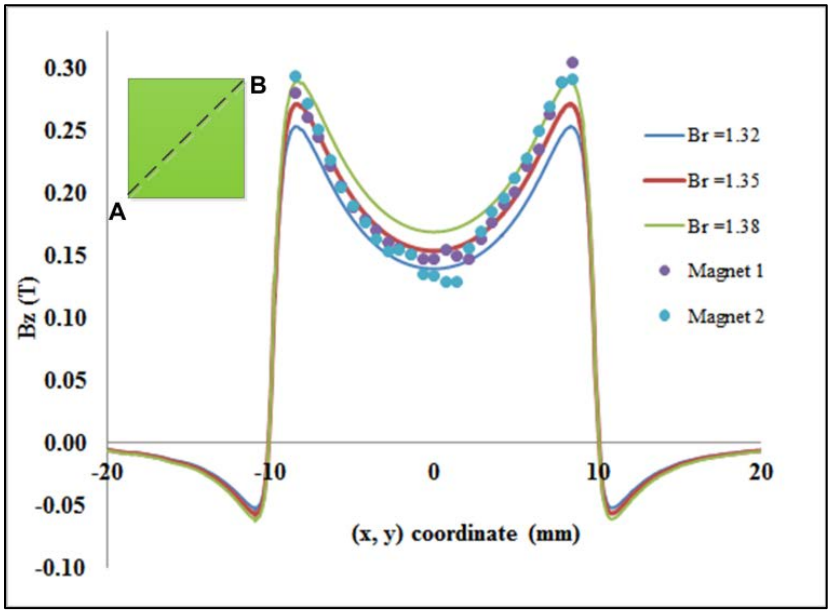


Figure 5.5 Measured (markers) and simulated (solid lines) distributions of B_z along *AB* at 0.6 mm above the surface of the magnet.

In Figure 5.5, the nominal B_r (1.35 T) curve of the simulation results most closely matches the experimental data of two different magnets from the same batch. However, the corners deviate from the simulated results, possibly due to edge effects as the demagnetizing field is larger at the magnet edges, leading to altered permeability when compared to the magnet interior [Nakahata 2011].

Figure 5.6 and Figure 5.7 show B_z measurements and simulation data along the *x* and *y* direction 1 mm from the edges of each magnet. As seen in Figure 5.6 and Figure

5.7, the simulation data with nominal B_r of *Magnet 1* is closely matched with experiment data while *Magnet 2* exhibits an average deviation of 0.034 T in the *x* - direction and 0.004 T in the y - direction.

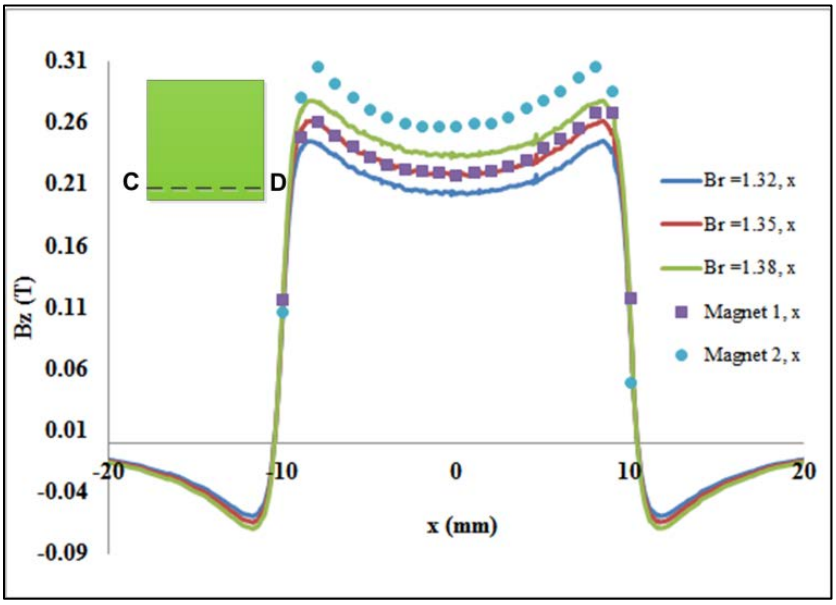


Figure 5.6 Measured (markers) and simulated (solid lines) distributions of B_z along *CD* (x at y = 1 mm) at 0.6 mm above the surface of the magnet.

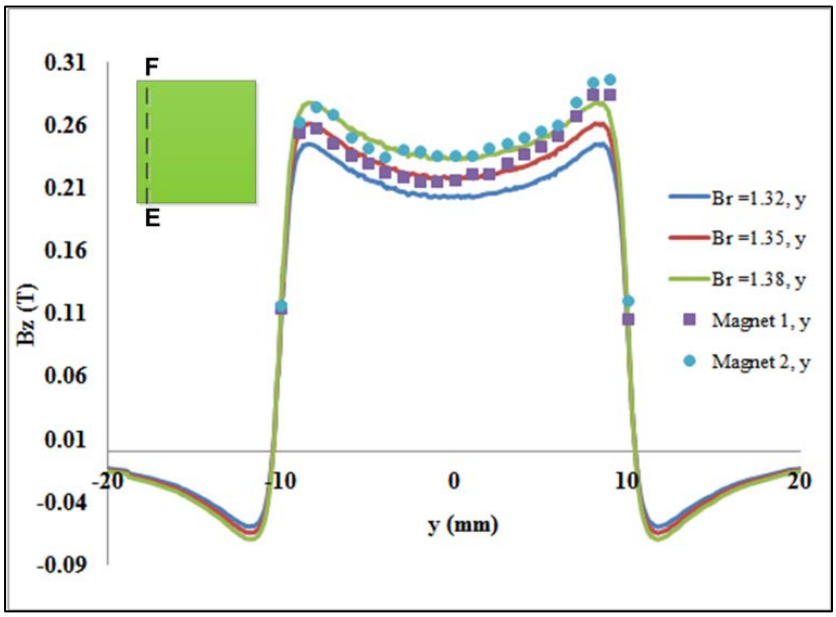


Figure 5.7 Measured (markers) and simulated (solid lines) distribution B_z along *EF* (along y, at x = 1 mm) at 0.6 mm above the surface of the magnet.

Table 5.1 Error analysis of the B_z between simulation with nominal B_r and measurement data of *Magnet 1* and *Magnet 2* samples.

Error category	**Magnet**	**Magnetic flux density (B_z) T Measurement line**		
		AB	**CD**	**EF**
Average Error (T)	Mag. 1	0.0017	0.0039	0.0042
	Mag. 2	0.0017	0.0347	0.0189
Standard deviation	Mag. 1	0.0118	0.0054	0.0105
	Mag. 2	0.0167	0.0222	0.0092
Average Error (T) (70%)	Mag. 1	-0.0011	0.0020	0.0020
	Mag. 2	-0.0017	0.0416	0.0182
Standard deviation (70%)	Mag. 1	0.0084	0.0031	0.0073
	Mag. 2	0.0157	0.0036	0.0053

As seen in Figure 5.5 and Table 5.1, the simulated results of the middle 70% area of the FEM model in the diagonal direction (*AB*) is closely matched with experimental measurements. The edge deviation can be explained by the higher demagnetization field present at the corners of the magnetic geometry. The *Magnet 2* experiment results of the *x* - direction is shifted by an average of 0.0416 T from the simulated results while the results of *Magnet 1* closely match with the average difference of 0.0020 T. These experimental results suggest that μ_{zy} is a non-zero quantity; however the μ_{zy} value is not available in the literature. This can explain the shift of *Magnet 2* in Figure 5.6 and the asymmetric nature of Figure 5.5and Figure 5.7 that caused deviation of the simulated results from experimental results.

5.5 μ_{xx} and μ_{yy} Dependance on B_z Magnetic Flux Distribution

The values of relative permeability (μ_r) can have a variation during the fabrication process. Also, it can be slightly different depending on the adopted fabrication

method: For example μ_{par} = 1.05 for axially pressed and μ_{par} =1.03 for isostatically pressed magnets [Bandit 2011]. Katter *et al* has observed that the μ_{par} has no correlation with coercivity whereas μ_{perp} decreases with increasing coercivity (1.17 for H_{cj} = 18 kOe and 1.12 for H_{cj} = 32 kOe) [Bandit 2011, Katter 2005]. Many of these exact values are not available when obtaining magnets from suppliers. In this section a parameter study was done to exploit the dependence of the parallel and perpendicular relative permeabilities on the distribution of magnetic flux density around a permanent magnet. Nominal B_r (1.35 T) and $\mu_{zz} = 1.12$ were kept constant for all the simulations in this study. Figure 5.8 shows that the B_z variation relative to μ_{xx} and μ_{yy} that are varying from 0-1.3 along the diagonal direction at *d* mm away from the top of the magnets. As seen in the figure, the significance of μ_{xx} and μ_{yy} are high close to the magnet and their influence decreases as the distance increases. Figure 5.9 shows the μ_{xx} and μ_{yy}influence on B_z closer to the edge of the magnet (along the line CD at 1 mm from the edge of the magnet). As graphite levitating d < 2mm distance, μ_{xx} and μ_{yy} have a significant influence on magnetic flux density and hence on levitation (see Section 3.8.1). Also, according to the Figure 5.8, the center portion of the magnet does not have significant influence by μ_{xx} and μ_{yy} values.

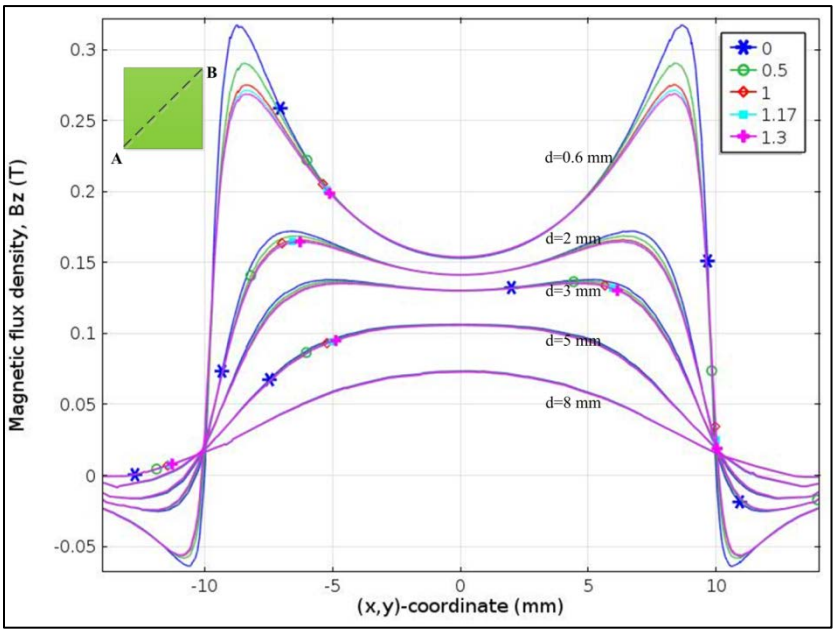


Figure 5.8 Simulated B_z for various μ_{xx} and μ_{yy}, along the line *AB* at *d* distance (d = 0.6, 2, 3, 5, 8 mm) above the surface of the magnet. Legend shows the $\mu_{xx}$and $\mu_{yy}(= \mu_{xx} = 0,0.5,1,1.17,1.3)$ values used in simulation. A and B coners of the magnet are at (-10,-10) and (10,10).

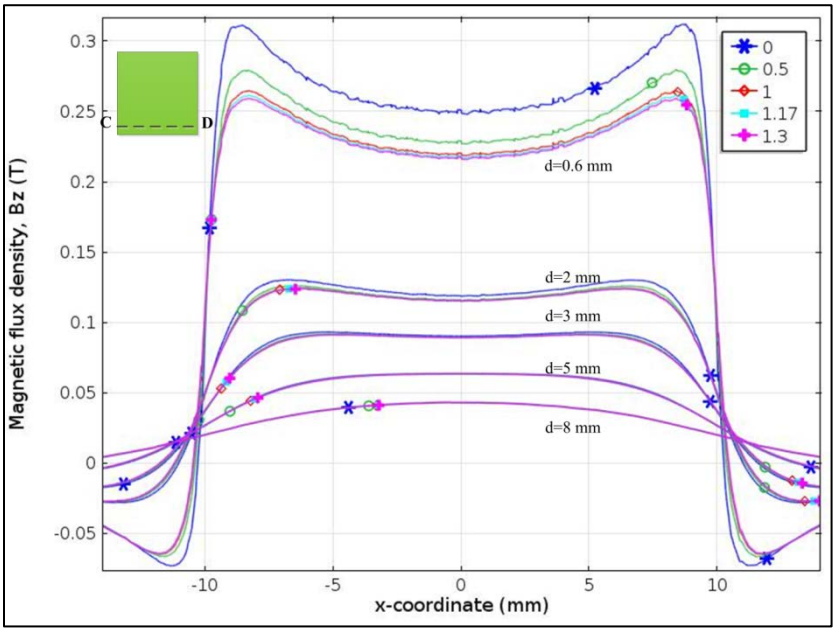


Figure 5.9 Simulated B_z for various μ_{xx} and μ_{yy}, along the line *CD* at *d* distance (d = 0.6, 2, 3, 5, 8 mm) above the surface of the magnet. Legend shows the μ_{xx} and $\mu_{yy}(= \mu_{xx} = 0,0.5,1,1.17,1.3)$ values used in simulation. *CD* line is along *x*- direction at y =1 mm distance.

5.6 Simulation and Verification of the ONP Model

5.6.1 Model Construction

Figure 5.10 represents the geometry of the model that has four 20 x 20 x 3 mm NdFeB magnets arranged in ONP configuration, surrounded by a 50 x 50 x 10 mm rectangular box, a 40 mm radius inner sphere, and a 50 mm radius outer sphere. The domain defined between the 40 mm and 50 mm radius spheres represents the domain for which the infinite element boundary condition is applied. NdFeB magnets were assigned with their material parameters and all other domains represent air. Magnets were simulated using the same domain properties given in one magnet modeling. The nominal value of B_r = 1.35 T, μ_{par} = 1.12 and μ_{perp} = 1.17 were used to define the magnetic properties of NdFeB magnets.

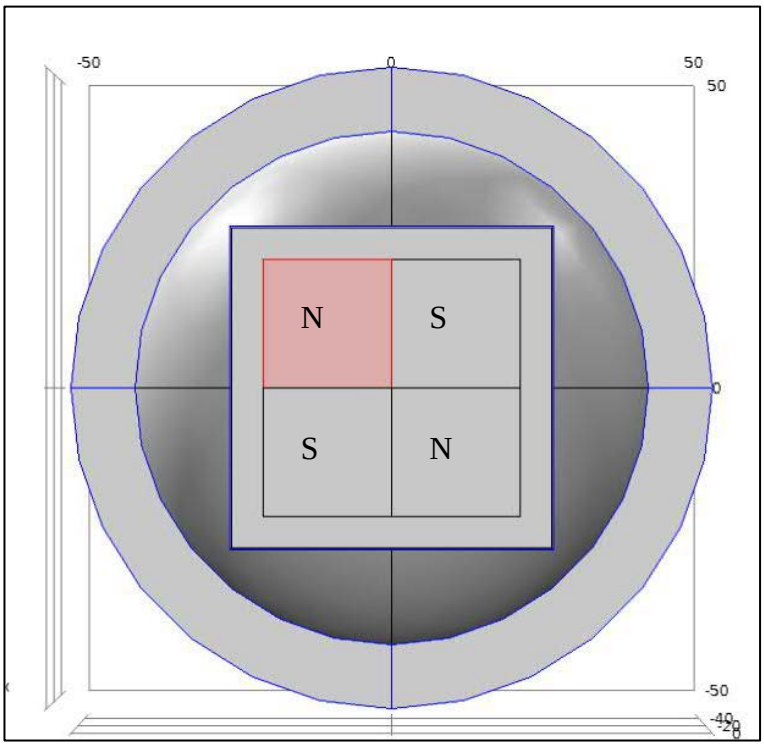


Figure 5.10 The four magnet model consists of 1) Four NdFeB magnets, 2) Measurement air box, 3) Inner air sphere and 4) Outer air sphere.

5.6.2 Simulation Results of ONP Configured Four Magnets

Figure 5.11 shows the magnetic flux, B_z distribution of four magnets 0.6 mm above the surface of the magnets: Height represents the magnitude of the Bz. As seen in the figure, the magnetic flux is highest near the boundary of the four magnets. The one magnet model result showed a symmetric B_z from the center of magnet in previous section. In contrast to the magnetic flux density distribution observed in the one magnet model (Figure 5.3), the Figure 5.11 shows asymmetric B_z from the center of magnet at 0.6 mm above the magnet. This can be explained by the super position principle: the magnetic flux at the interface of the magnets is a super-position of the fields from the neighboring magnets. The inset shows B_z at 4.6 mm above the magnetic surface.

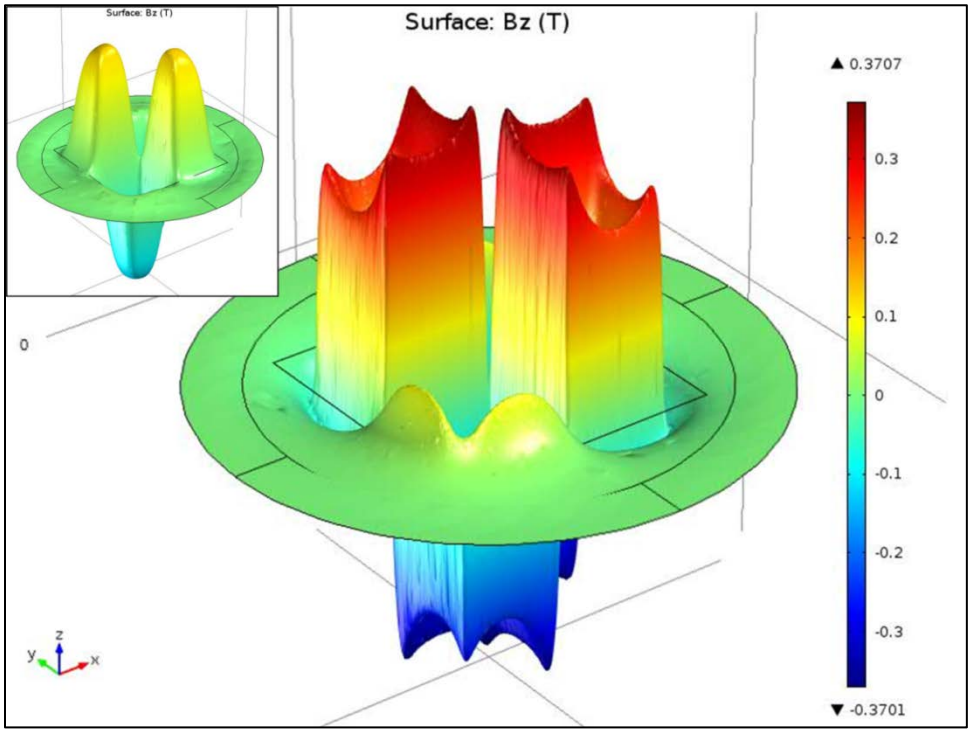


Figure 5.11 Bz distribution at d=0.6 mm. Inset shows the Bz at d=4.6 mm. height represent the magnitude of the Bz.

Figure 5.12 shows the simulated results of B_z at various distances (d) above the surface of the magnet: B_z closer to the interface of the magnets is larger compared to the corners at G and H. B_z decreases as moves further away from the surface of the magnet.

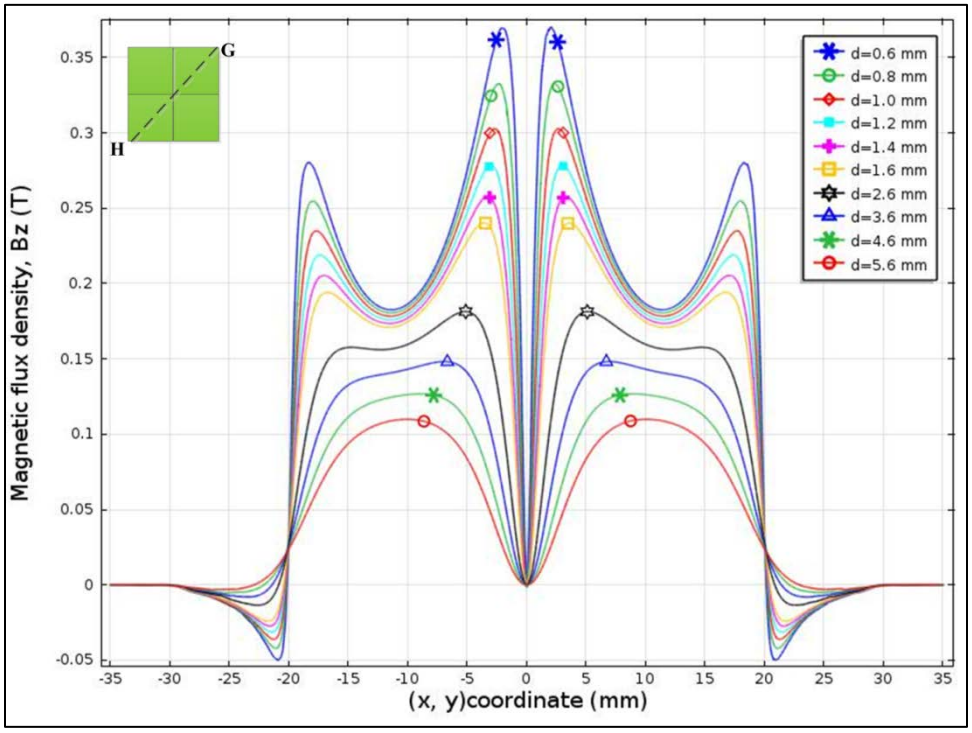


Figure 5.12 Simulated results of the distribution of B_z along the line AB at d distance above the surface of the magnets.

5.7 Magnetic Flux Density Measurement

Magnetic flux density measurements were carried out to map the magnetic flux distribution above the ONP configured magnets by using a computerized XYZ stage (Newport M-460A) and a Magnetometer (AlphaLab DC): the measurement set up is shown in Figure 5.13. Flux measurements were taken by increasing the gap between the magnets and the magnetometer sensor in increments of 0.2 mm from 0 to 2 mm and in increments of 1mm from 2 to 5mm. The flux measuring sensor is located 0.6 ± 0.1 mm from the surface of the lead. Figure 5.14 shows the magnetic flux surfaces plot generated by the measurements.

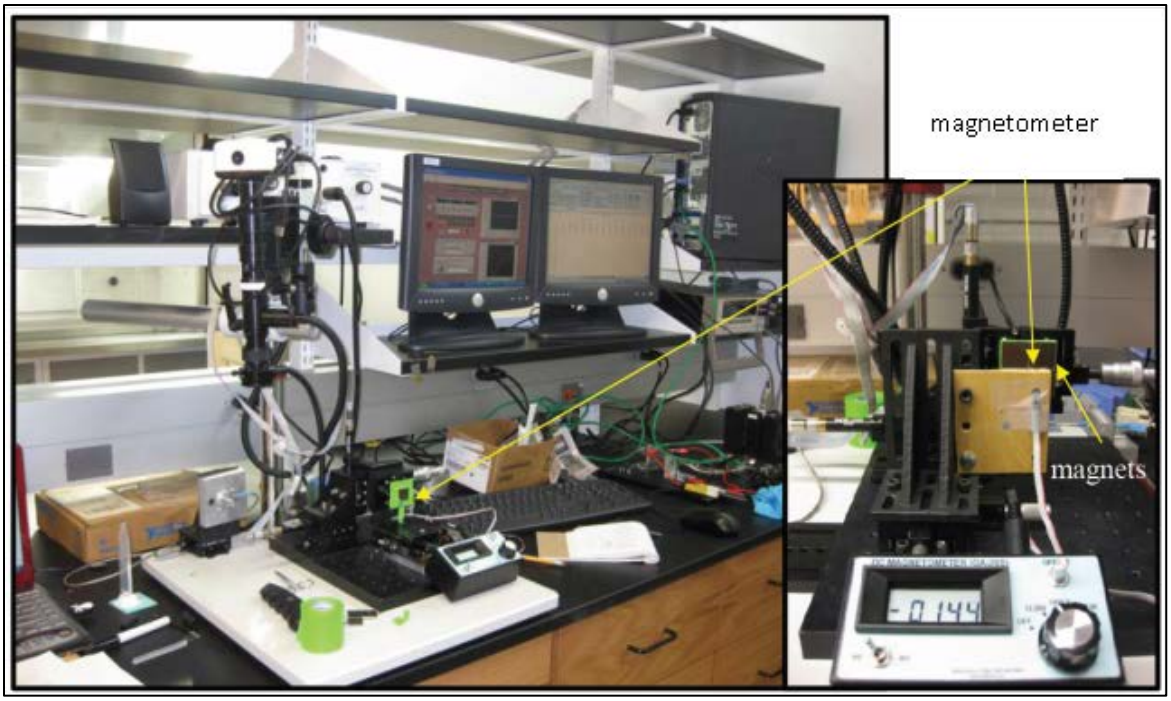


Figure 5.13 Experimental setup for magnetic flux density measurements.

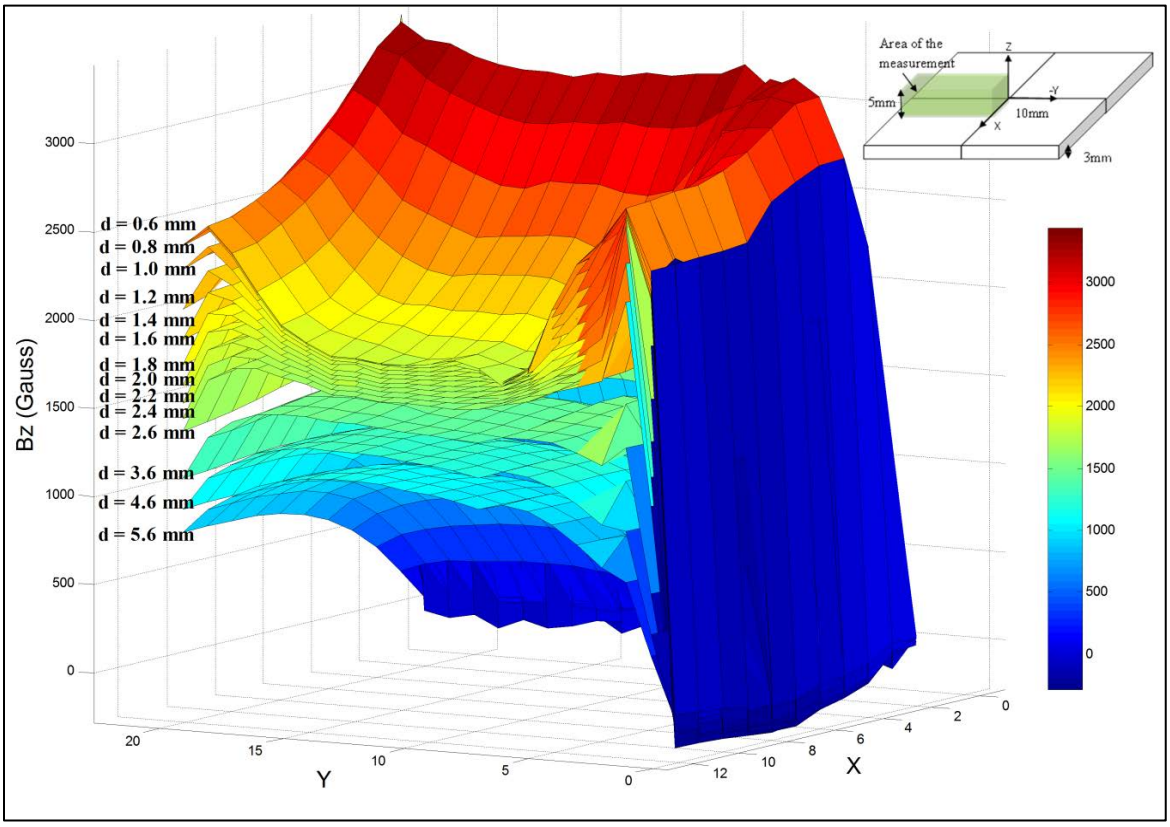


Figure 5.14 Magnetic flux surface plots obtained from measurements. The sketch in the inset illustrate the area of measurement shown in the surface plot graph.

5.8 Comparison with Experimental Results

Figure 5.15 shows the comparison of simulated and experimental results of magnetic flux density, B_z in the diagonal direction at different d distances above the surface of the magnets.

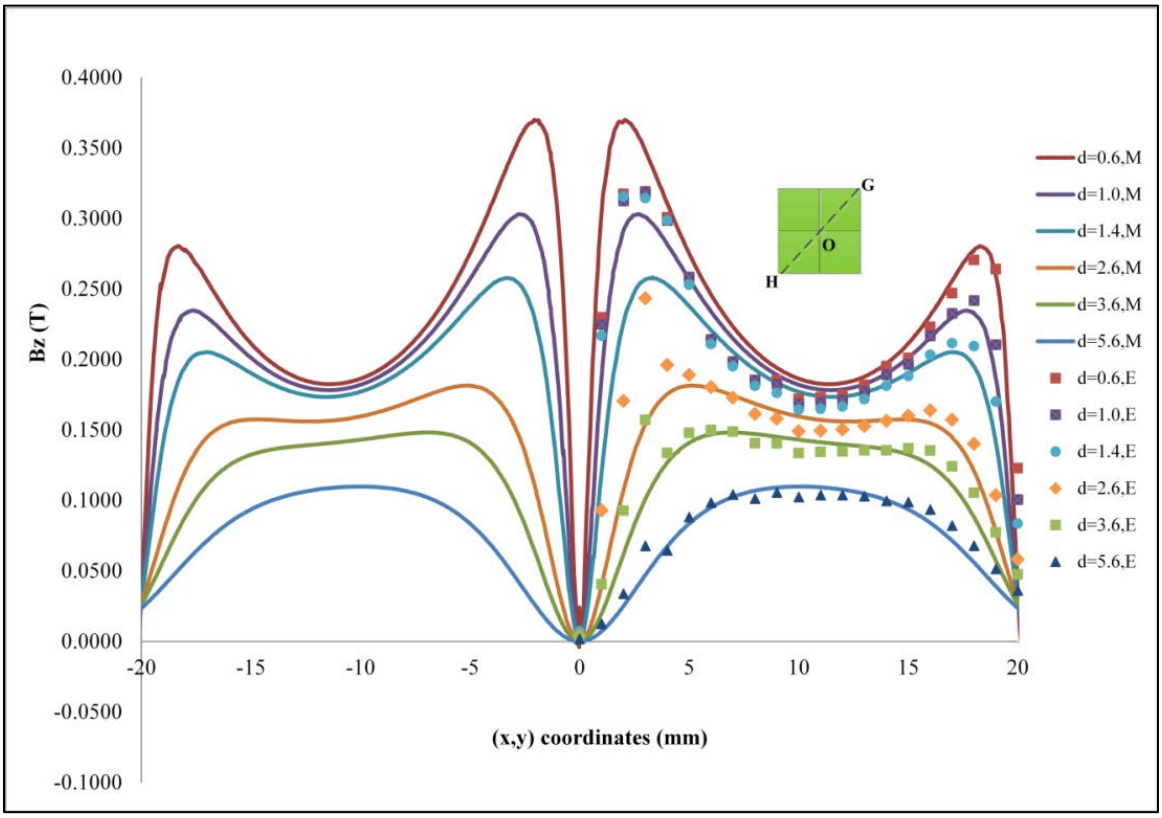


Figure 5.15 Measured (markers) and simulated (solid lines) distributions of B_z along the diagonal line of the ONP configured four magnets at *d* mm above the surface of the magnets.

The measurement and the simulation are in good agreement at the *G* corner of the magnet. However closer to *O*, the experimental values somewhat deviate from simulation results. There can be several causes to the deviation of simulation results from experimental results. One reason is the fact that each magnet has somewhat different values and the real parameter can vary from that of nominal parameters within the range

as given in the manufacturer's data sheet. However, all the magnets in simulation were simulated with the same magnetic properties (B_r = 1.35 T, μ_{para} = 1.12 and μ_{per} = 1.17). Also, there is a position uncertainty in the stage and the sensor uncertainty should be a factor in the measurement errors. Additionally there is a ± 2% error in the magnetometer.

Figure 5.16 shows the simulated magnetic flux densities, B_z of N (= 1, 2 and 3) layers of magnets that are arranged in ONP configuration d = 0.6 mm above the magnets. The B_z magnitude increases as N increases. However, the increment due to each layer decreases as the number of layers increases as expected (due to $B \propto 1/r$ influence of the bottom magnet get smaller).

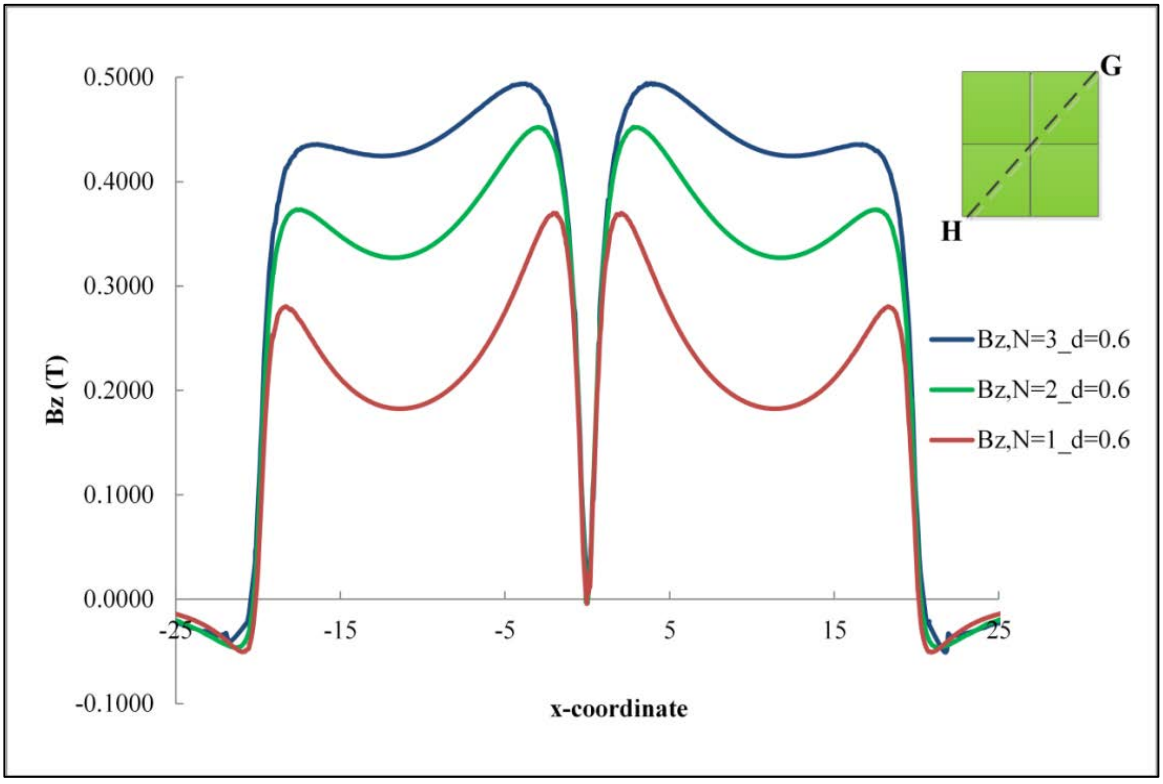


Figure 5.16 Simulated results of the distribution of B_z along the diagonal line at d=0.6mm distance above the surface of the magnets for N = 1, 2 and 3 layers of magnets arranged in ONP configuration.

CHAPTER 6

STATIC LEVITATION MODEL AND MAGNETO-MECHANICAL COUPLING

Objective of this chapter is to establish a model for diamagnetic levitation that can be used in the design and optimization of levitating devices and systems. There are two important parameters are needed to accomplish this task: One is the magnetic flux density distribution of ONP configured magnets which was established in *Chapter 5*. The other important parameter is the accurate data for susceptibility of pyrolytic graphite (PG). The parallel and perpendicular susceptibilities of PG were obtained from the ***M-H*** measurements performed using *physical property measurement system* (PPMS). Afterward the levitation model was developed employing experimentally verified material properties. Then developed model was then employed to obtain the parameters such as magnetic force, levitation height and orientation of the levitating objects.

6.1 M-H Measurements for Pyrolytic Graphite

Diamagnetism has been known for many years. However, some of the more common handbooks appear to contain inconsistencies in susceptibilities [Simon 2001]. Different grades of pyrolytic graphite made under different conditions may have led to inconsistent information. For example, Fischbach's investigation reports that the susceptibility is between 20-30 x 10^{-6} cgs units/gram for different deposition conditions [Fishchbach 1961]. To further complicate matters, diamagnetism can be highly anisotropic and the given values may be for different orientation of the graphite. The

pyrolytic graphite used in this investigation is commercially acquired and the susceptibility data were not available. Due to these reasons, ***M-H*** measurements were carried out using the *Physical Property Measurement System* (PPMS) to determine the diamagnetic susceptibility. Magnetization (***M***) of the pyrolytic graphite in the parallel axis (parallel to the plane of the graphite) and perpendicular axis (perpendicular to the plane of the graphite) were measured by varying the applied magnetic field (***H***) from -10 000 Oe (-1T) to 10 000 Oe (1 T) for two cycles: the measurements followed the same path for both cycles. The χ was obtained by plotting the graph between ***M*** and ***H*** (for diamagnetic materials, $\boldsymbol{M} = \chi \boldsymbol{H}$). The ***M-H*** measured values for 0 – 1 T magnetic field are shown in Figure 6.1. According to the Figure 6.1, the direction perpendicular to the PG sheets has an approximately seven times higher magnetic susceptibility than parallel. The values of magnetic susceptibility of some diamagnetic materials are given in Table 6.1. The χ values obtained by measurements are in good agreement with the values given by Simon *et al*. [Simon 2001].

Table 6.1 Values of χ for some diamagnetic materials (Extracted from reference [Simon 2000]).

Material	**$-\chi$ ($\times 10^{-6}$)**
Water	8.8
Bismuth Metal	170
Graphite rod	160
Pyrolytic graphite ($\perp$ axis)	450
Pyrolytic graphite ($\parallel$ axis)	85

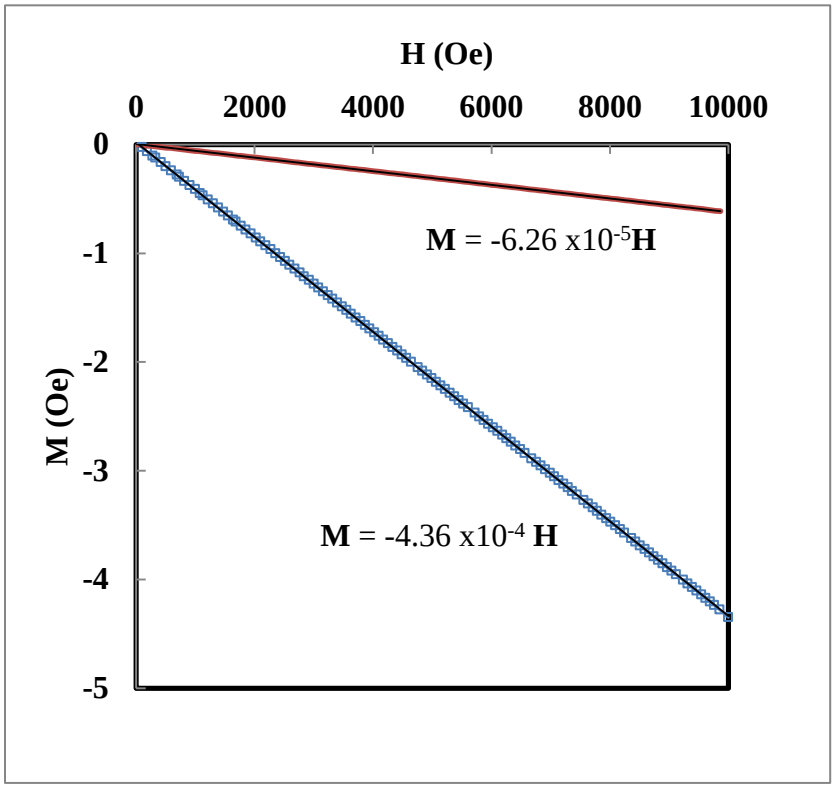


Figure 6.1 M-H measurements of the pyrolytic graphite: Perpendicular axis (○) and parallel axis (-).

6.2 Static Levitation Model

Figure 6.2 shows the model geometry created to simulate static levitation. The model shown in the figure consists of two layers (N = 2) of 20 x 20 x 3 mm NdFeB magnets (i.e. Eight magnets that are in ONP configuration) and a pyrolytic graphite proof mass at d distance above the top surface of the magnets, surrounded by a 45 x 45 x 15 mm rectangular box, a 40 mm radius inner sphere, and a 50 mm radius outer sphere.

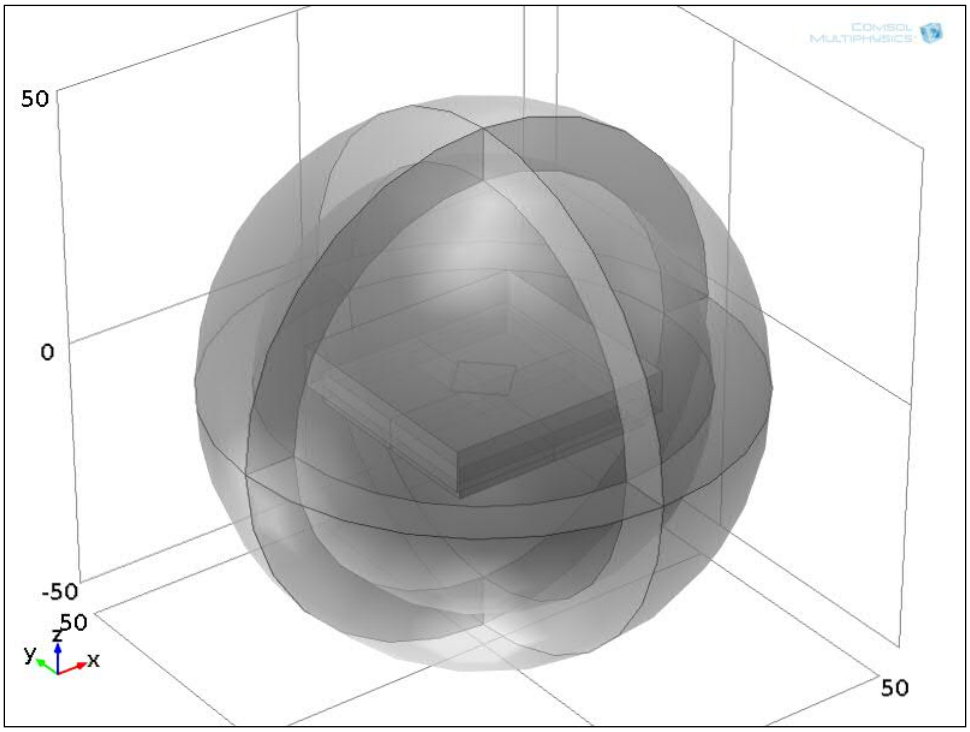


Figure 6.2 The model geometry for the levitation model: the model consist of, 1) Two layers of NdFeB magnets, 2) Measurement air box, 3) Pyrolytic graphite, 4) Inner air sphere and 5) Outer air sphere.

The domain defined between the spheres of radius 40 mm and 50 mm, represents the domain for which the infinite element boundary condition is applied. NdFeB magnets and pyrolytic graphite domains were assigned to their material parameters and all the other domains represent air. The model developed for four magnets in the *Chapter 5* was utilized to define all the material and magnetic parameters except the pyrolytic graphite. The magnetic property of the PG domain was defined by equation 6.1 [Furlani 2001].

$$\boldsymbol{B} = \mu_0(\boldsymbol{H} + \boldsymbol{M}) \tag{6.1}$$

where $\boldsymbol{M}$ is the magnetization of the pyrolytic graphite. For a diamagnetic material, $\boldsymbol{M}$ is given by,

$$\boldsymbol{M} = \chi(H)\boldsymbol{H} \tag{6.2}$$

Experimentally obtained parallel and perpendicular χ values were used to define the magnetization $\boldsymbol{M}$ of equation 6.2. Figure 6.3 and Figure 6.4 show the flux density, B_z and magnetization, M_z at d (=1 mm) distance, respectively. Table 6.2 provides the physical parameters used for modeling. As seen in Figure 6.4, the induced magnetization, M_z of the graphite is opposite to the direction of the applied field and confined only to the graphite area as expected (characteristic of diamagnetic material). If the graphite is placed in an electromagnetic field that produced by a solenoid, the induced magnetization of the whole graphite should be in the same direction as the applied magnetic field of a solenoid is unidirectional unlike in ONP configuration of the permanent magnets.

Table 6.2 The model parameters used to produce Figure 6.3 and Figure 6.4.

Description	**Symbol**	**Value**	**Unit**
NdFeB magnet width	w	20	mm
NdFeB magnet thickness	t_m	3	mm
NdFeB magnet layers	N	3	-
Pyrolytic graphite length	l	15	mm
Pyrolytic graphite thickness	t	1.0085	mm
Magnetic susceptibility of PG ($\perp$ axis)	χ_{perp}	-43.6×10^{-5}	-
Magnetic susceptibility of PG (|| axis)	χ_{par}	-6.26×10^{-5}	-
Air gap	d_a	0.8170	mm
Distance from the top of the magnet	d	1	mm

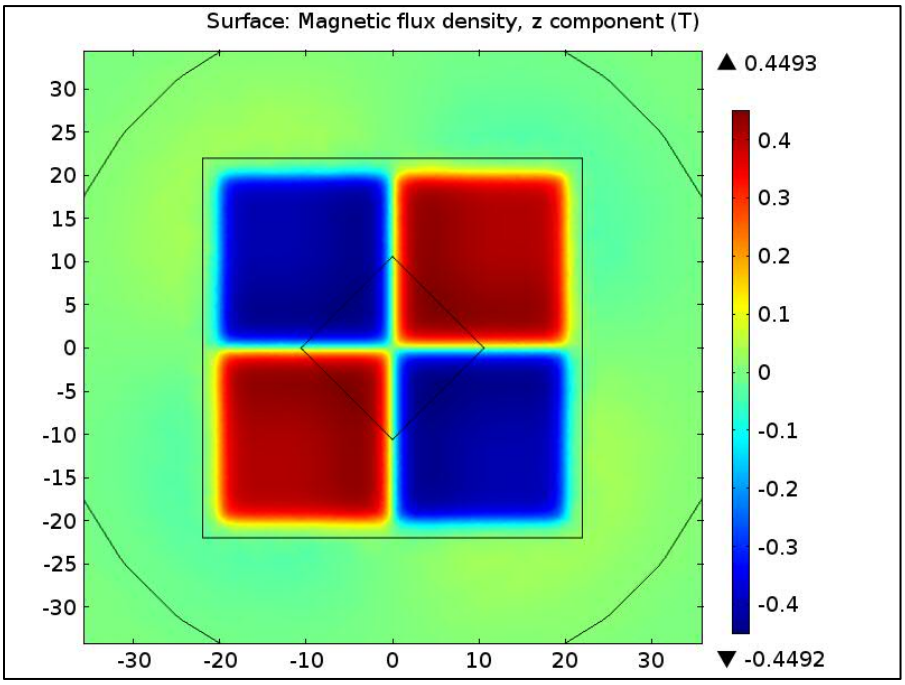


Figure 6.3 *z*- component of magnetic flux density, B_z distribution of N=3 layers of magnets at d = 1 mm.

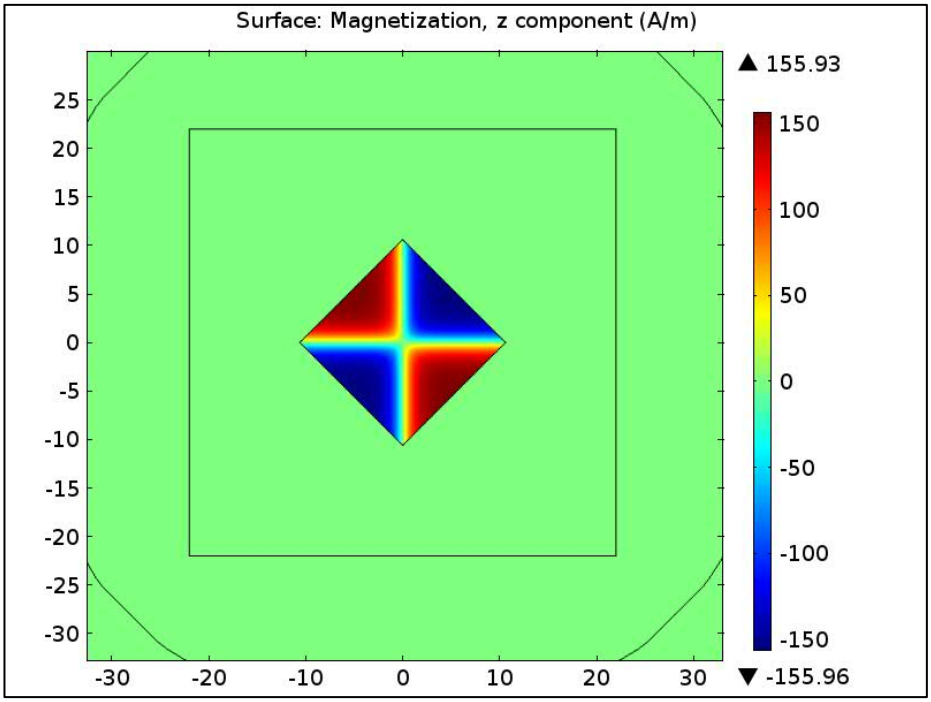


Figure 6.4 Induced magnetization, M_z of graphite layer at d = 1 mm distance under the influence of N = 3 layers of magnets.

6.3 Magnetic Force Simulation

FEM model is an indispensable tool when it comes to verifying the accuracy of the force equation. As discussed in *Chapter 3*, there are two models that exist in the literature giving two different final expressions for the magnetic force. First, the fundamental expression of the *current model* is considered for simulations. Afterwards the expression of the *charge model* is examined and then the two model results will be compared. The force due to the induced magnetization from the *current model* is,

$$\boldsymbol{F_m} = \nabla(\boldsymbol{M}.\boldsymbol{B}) \tag{6.3}$$

The relation given in 6.3 is used to simulate the force induced from the graphite proof mass due to N (= 1, 2 and 3) magnet layers. The main variable of the equations for force produced in the z-direction (F_z) are induced magnetization (M_z), magnetic flux (B_z) and the volume (v). Unlike from an electromagnet, the permanent magnet distribution in the space is quite complex and highly spatially dependent. Obtaining induced force F_z would have been tedious or even an impossible task using equation 6.3 by analytical or experimental methods.

The F_z force was obtained by simulating various lengths of graphite proof masses that are given in Table 6.3. The average thicknesses (from nine measurements taken at position in 3 x 3 equidistance 2D array) of the proof mass and relevant levitation height obtained from measurements were used in the simulations to obtain the magnetic force acting on the graphite mass. The simulations were carried out for influence of N (=1, 2 and 3) layers of magnets that are in ONP configuration. The same procedure was followed for the proof masses with various thicknesses and the model parameters relevant to this study are given in Table 6.4. F_z force values obtained by FEM simulations along

with the weight of the proof mass are illustrated in Figure 6.5 and Figure 6.6 for various *t* and various *l* respectively. As seen in the figures, the simulated force of the proof masses closely match the weight of each proof mass providing evidence that the magnetic force is equal to the weight at equilibrium levitation.

Table 6.3 Measured air gaps of proof masses with various lengths and same thickness. Measured average thicknesses of each proof mass also given.

Length of the PG, *l* (mm)	**Average Thickness, t (mm)**	**Air gap - d_a (mm)**		
		***N*=1**	***N*=2**	***N*=3**
3	1.1096	0.1869	0.2228	0.2938
4	1.0479	0.4609	0.5459	0.5663
5	1.1172	0.4005	0.5119	0.5156
6	0.9791	0.4907	0.6182	0.6414
7	0.9412	0.5244	0.6895	0.7393
8	0.9250	0.5654	0.7224	0.7605
9	1.0428	0.4904	0.7445	0.8016
10	0.9117	0.5638	0.7796	0.8496
11	1.0600	0.5436	0.7615	0.8268
12	0.9326	-	0.7888	0.8717
13	0.9814	-	0.8343	0.9285
14	1.0498	-	0.7978	0.8873
15	1.0085	-	0.8170	0.9470
17	1.0261	-	0.6569	0.7761
19	1.0064	-	0.7814	0.9181
20	1.0859	-	-	0.8724

Table 6.4 Measured air gaps of proof masses with various thickness and same length.

Length of the PG, *l* (mm)	**Thickness, t (mm)**	**Air gap, d_a (mm)**		
		***N*=1**	***N*=2**	***N*=3**
10	0.2603	0.8375	1.025	1.0973
10	0.5046	0.759	0.9417	1.0046
10	0.6917	0.6461	0.8649	0.9301
10	0.8813	0.567	0.7838	0.8668
10	1.0479	0.4952	0.7397	0.7903

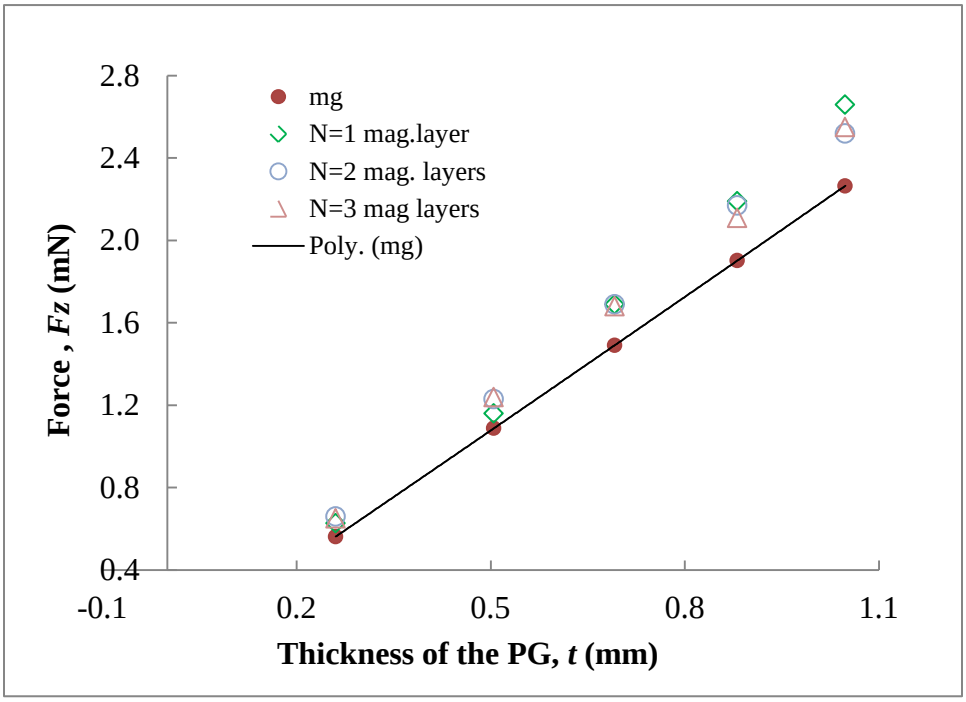


Figure 6.5 Measured and simulated forces (using *current model*) of various *t* of PG proof masses with influence of *N* = 1, 2 and 3 layers of magnets in static levitation.

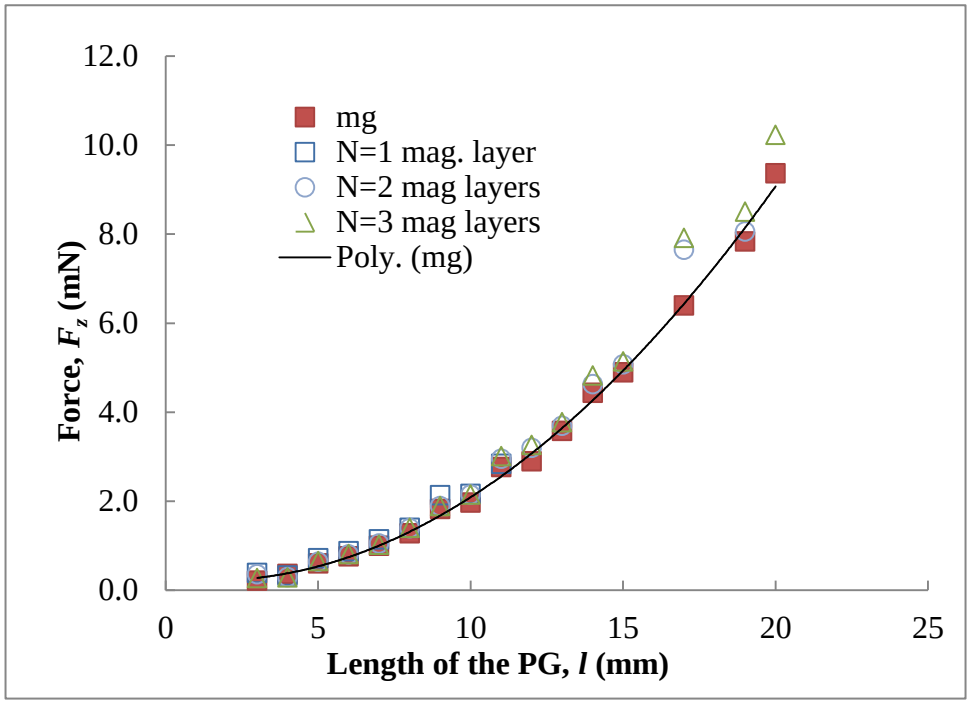


Figure 6.6 Measured and simulated forces (using *current model)* of various *l* of PG proof masses with influence of *N* = 1, 2 and 3 layers of magnets in static levitation.

As discussed in *Chapter 3*, there are two models for magnetic force calculation. The final expression of *Current model*,

$$F_{m,z} = \iiint \frac{\chi_z}{\mu_0} \frac{d}{dz} B_z^2 \, dv \tag{6.4}$$

The final expression of *Charge model*,

$$F_m = \iiint \frac{\chi}{2\mu_0} \frac{d}{dz} \boldsymbol{B}^2 \, dv \tag{6.5}$$

Figure 6.7 compares the results of magnetic forces obtained by the final expression of each model to find the applicability of each model in diamagnetic levitation. The figure shows the $F_{m,z}$ obtained from the *current model* has a good agreement with experiment results and the charge model results deviate significantly from experiment results. This concludes that the current model is the accurate model for diamagnetic levitation similar to the finding in neutron experiments [Boyer 1987]. Note that for the simulations, all the magnets were simulated with nominal parameters and also considered identical. This might have caused the slight differences between simulated magnetic force and weight of PG proof masses.

This verification of the force is an important finding for levitation FEM modeling. It allows the ability to design systems and optimize variable parameters without performing experiments. This will save time and material while providing more degrees of freedom of parameter space.

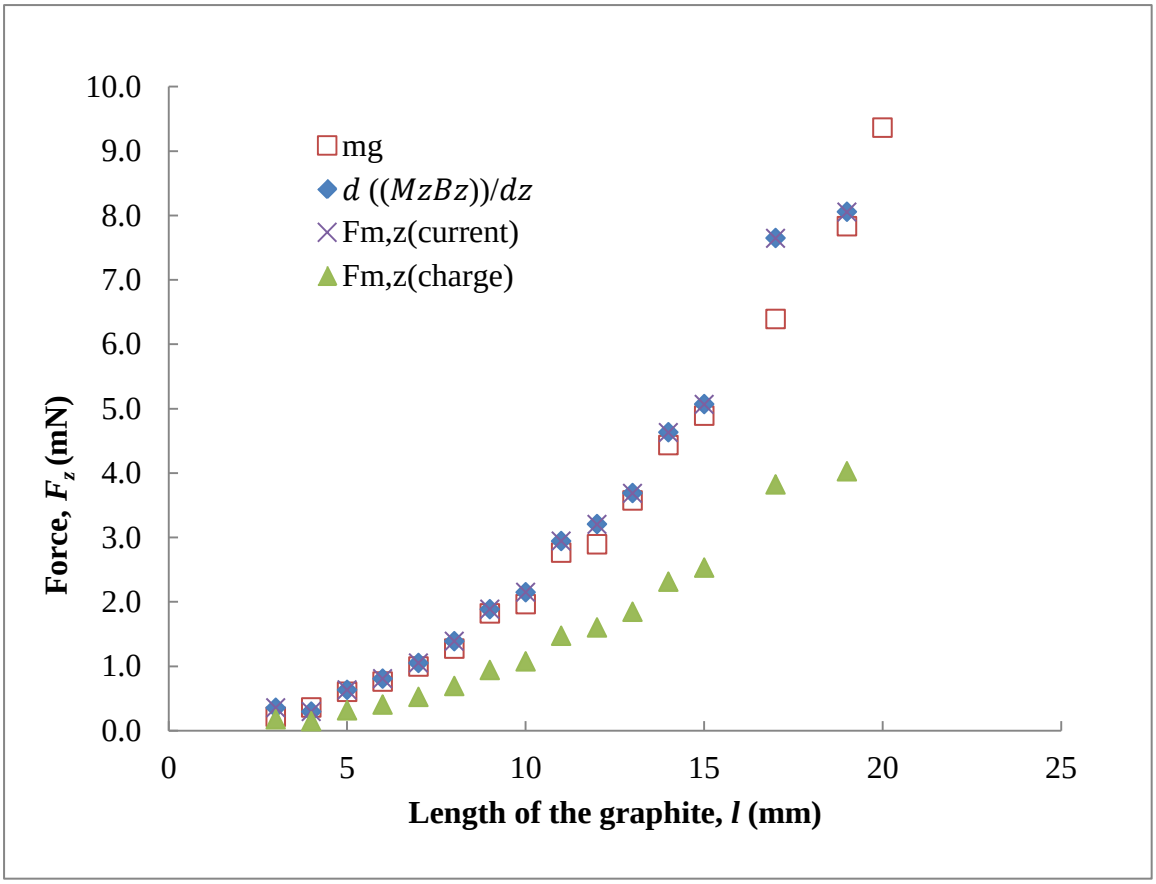


Figure 6.7 Comparison of the forces derived from the *current model* and the *charge model* against the weights of the proof masses. *N*=2 magnet layers.

6.3.1 Static Levitation Height and Maximum Levitable Size Obtained from Simulation

Figure 6.8 demonstrates the use of FEM model results to find the static levitation height of the diamagnetic objects. The simulated magnetic force, *Fz* can be obtained by FEM models for different air gaps. The simulated magnetic forces can be plotted against air gaps in a graph along with the relevant weight of the PG. The static levitation height can be obtained by the air gap where the magnetic force equivalents to the weight of the PG.

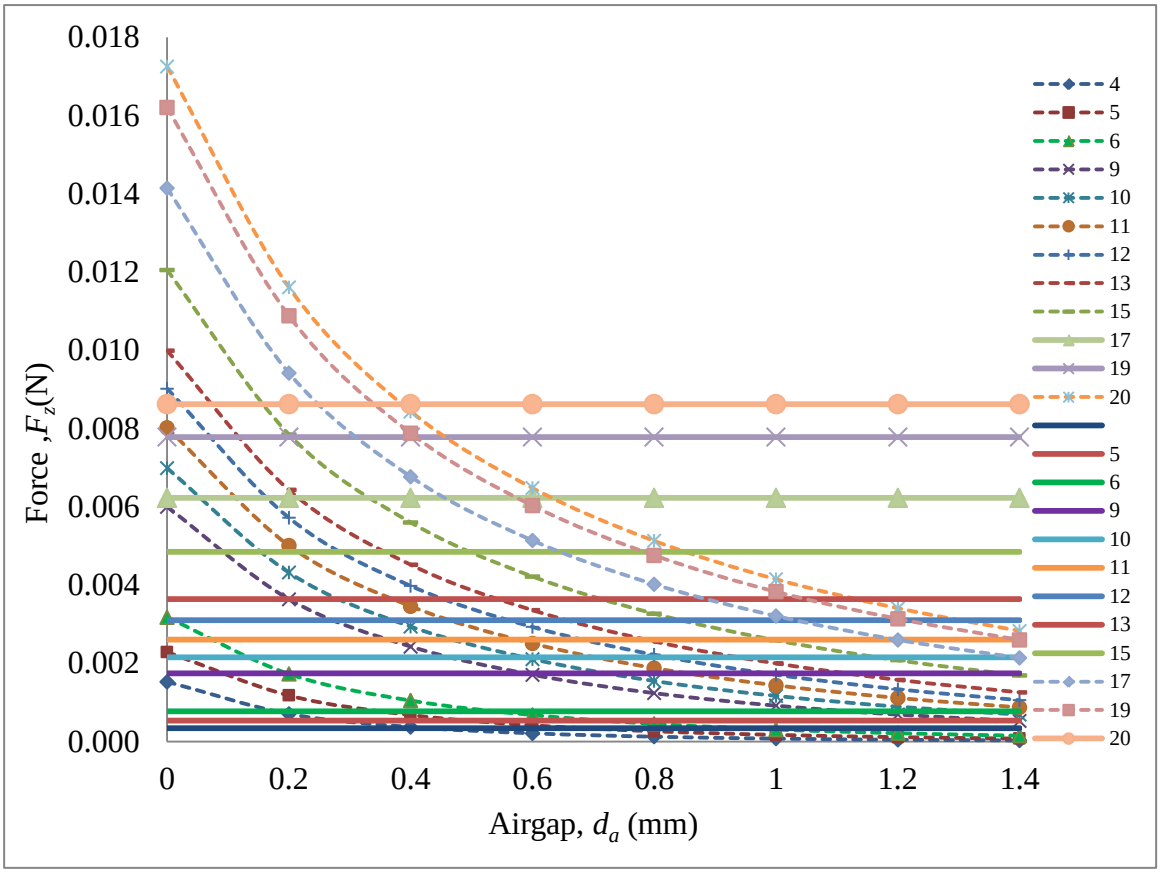


Figure 6.8 Simulated forces (dotted lines) for graphite masses with t=1 mm and various l (= 4 to 20 mm) at d_a (air gap) distance above the N=1 layer of magnets. Solid lines represent the weight of the graphite mass of various length l (= 4 to 20).

Table 6.5 shows the comparison of measured and simulated air gaps obtained for N =1, 2 and 3 layers of magnets. Thicknesses of all PG proof masses were taken as 1 mm for simulations. The air gap as seen in Figure 6.8 decreases after the l=11 mm for N=1 and experimentally we observed that the maximum length can levitate from N=1 layer of magnets is 11 mm. Similarly, the simulated air gap decrease after approximately l=17 mm for N=2 system and l=25 mm for N=3 system. Experimentally we observed maximum levitation size of the proof mass for N=2 system as l= 19 mm and the maximum size for N=3 system is not available as our experiments were limited to l = 20 mm. This information show that it is possible to obtain an approximate idea about the

maximum size of the proof mass that can levitate for a given magnet system from a simulations by the point where the air gap (or levitation height) start to decrease as the size increases.

Table 6.5 Comparison of measured and simulated air gap at static equilibrium levitation obtained for N =1, 2 and 3 layers of magnets. For the simulations, graphite thickness of all the specimens was taken as 1 mm. NS ≡Not stable levitation possible.

l **(mm)**	**Average thickness, t (mm)**	**Air gap - d_a (mm)**					
		***N*=1**		***N*=2**		***N*=3**	
		Exp.	**Simu.**	**Exp.**	**Simu.**	**Exp.**	**Simu.**
4	1.0479	0.4609	0.4373	0.5459	0.4982	0.5663	0.4978
5	1.1172	0.4005	0.5080	0.5119	0.5756	0.5156	0.5828
6	0.9791	0.4907	0.5488	0.6182	0.6486	0.6414	0.6692
9	1.0428	0.4904	0.5899	0.7445	0.7868	0.8016	0.8426
10	0.9117	0.5638	0.5889	0.7796	0.8140	0.8496	0.8904
11	1.0600	0.5436	0.5792	0.7615	0.8372	0.8268	0.9235
12	0.9326	NS	0.5667	0.7888	0.8518	0.8717	0.9508
13	0.9814	NS	0.5511	0.8343	0.8594	0.9285	0.9725
15	1.0085	NS	0.5086	0.8170	0.8589	0.9470	0.9979
17	1.0261	NS	0.4662	0.6569	0.8426	0.7761	1.0116
19	1.0064	NS	0.4105	0.7814	0.8143	0.9181	1.0128
20	1.0859	NS	0.3884	NS	0.7976	0.8724	1.0102
21			0.3696		0.7834		1.0046
22			0.3507		0.7676		0.9984
23			0.3318		0.7509		0.9913
25			0.2849		0.7138		0.9750

Figure 6.9 shows the simulated air gaps of various l proof masses at static equilibrium levitation under the influence of N (=1,2 and 3) layers of magnets.

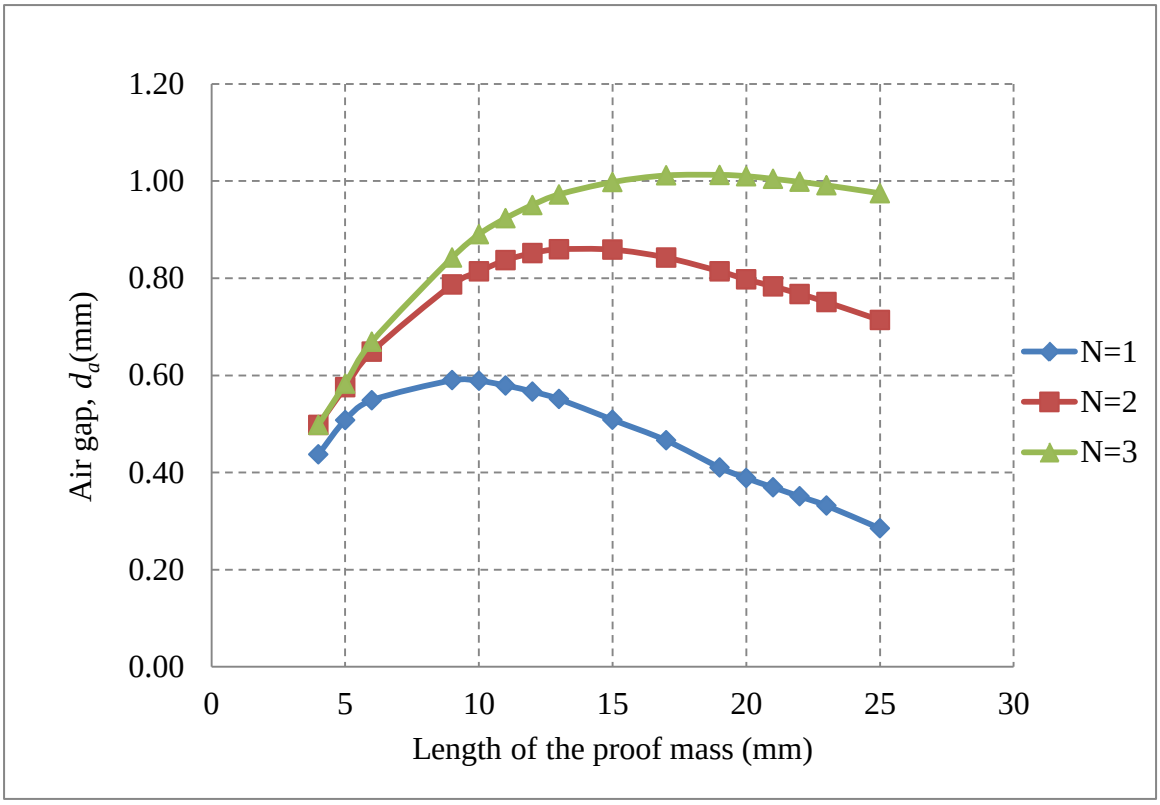


Figure 6.9 Simulated air gaps of various length of proof masses at static equilibrium levitation (*N* =1, 2 and 3 layers)

6.3.2 Magnetic Potential Simulations

The potential energy (U) of a dipole is given by,

$$\mathrm{U} = -(\boldsymbol{m} \cdot \boldsymbol{B}) \tag{6.6}$$

where $\boldsymbol{m}$ is the dipole moment and $\boldsymbol{B}$ is the magnetic flux density. The potential energy of the PG is,

$$\mathrm{U} = -\iiint \left(\frac{\boldsymbol{\chi}}{\boldsymbol{\mu}}\boldsymbol{B} \cdot \boldsymbol{B}\right) dv \tag{6.7}$$

According to the equation 6.7, the potential energy depends on $\boldsymbol{B^2}$. The Figure 6.10 illustrates the $\boldsymbol{Bz^2}$ distribution at d= 0.6mm distance above the magnet arrangement. As seen in the figure, the area closer to the center of the arrangement has the highest Bz^2

values. That provides an indication that the energy minima lie around that region of the arrangement.

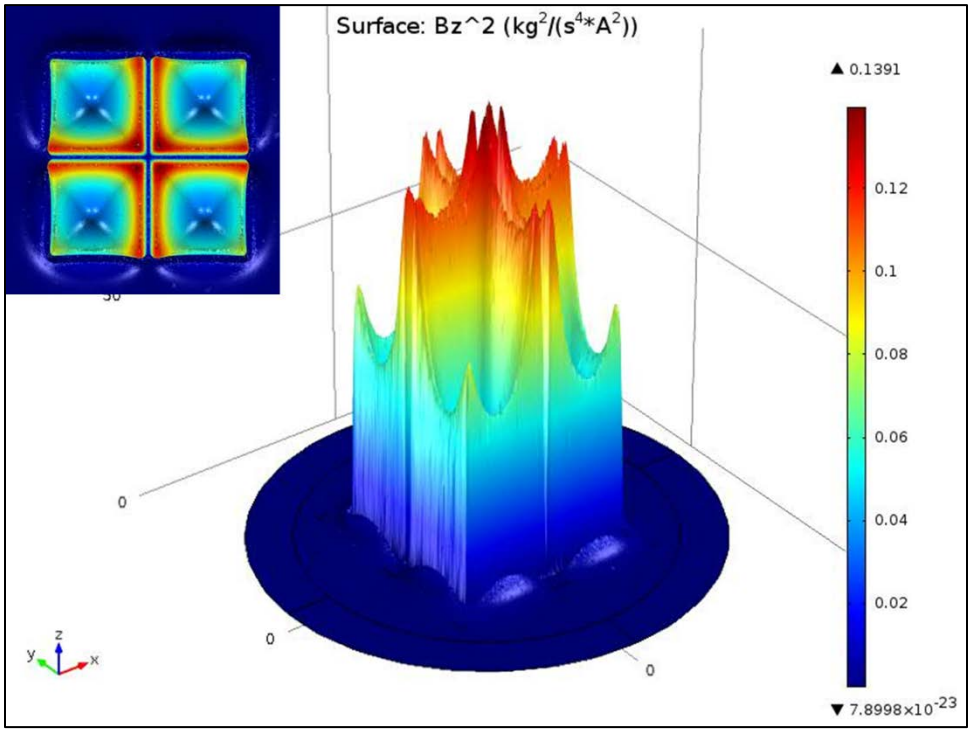


Figure 6.10 Simulation B_z^2 at d=0.6mm above the magnets for ONP configured N=1 layer of magnets. Inset illustrates the arial view of the magnets.

The equation 6.6 was used to simulate the potential energy of l =10 mm, t = 1mm proof mass over the volume by varying angle from 0 to 90º. As seen in Figure 6.11, the minimum potential energy is given when the angle is 45º. This verifies that the graphite oriented itself to the energy minimum position. The simulated torque of the graphite along the x- direction also gives the lowest value at 45º as illustrate in Figure 6.12 . It is worth noticing that the calculated gravitational potential energy (*mgh*) at this point is 2.2 μJ, taking the surface of the magnet as the potential energy zero level. One can clearly see the gravitational potential energy value closely matches the potential energy obtained by the magnetic dipole method.

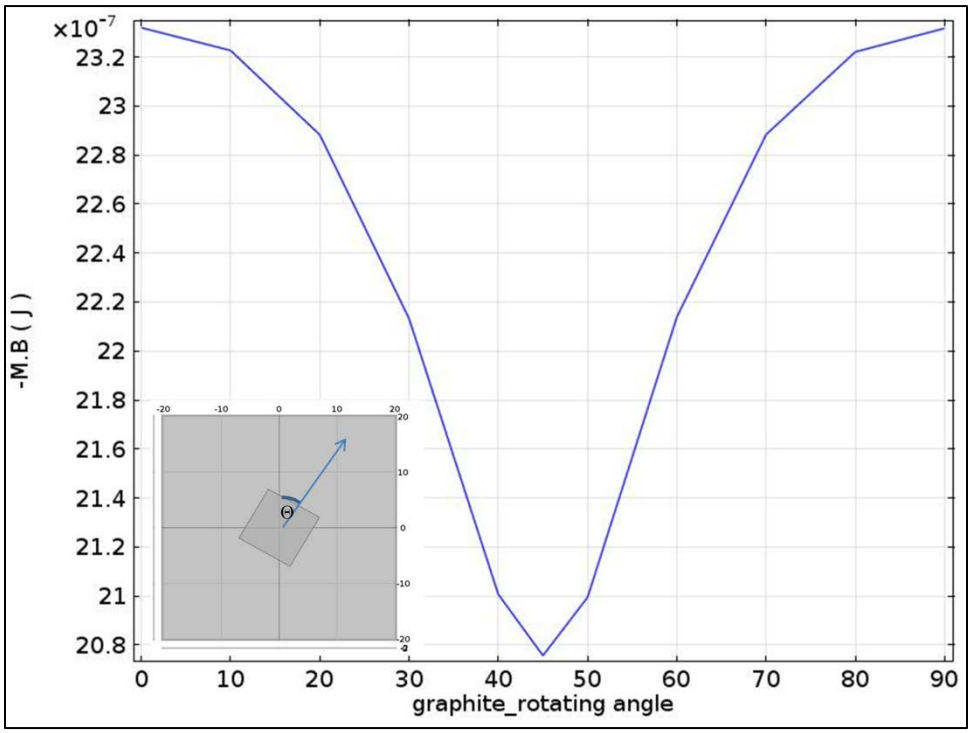


Figure 6.11 Simulated potential energy for l=10 mm, t= 1.0 mm graphite proof mass at d_a= .4952mm (air gap) by rotating angle from 0 to 90 under N=1 magnet layer influence.

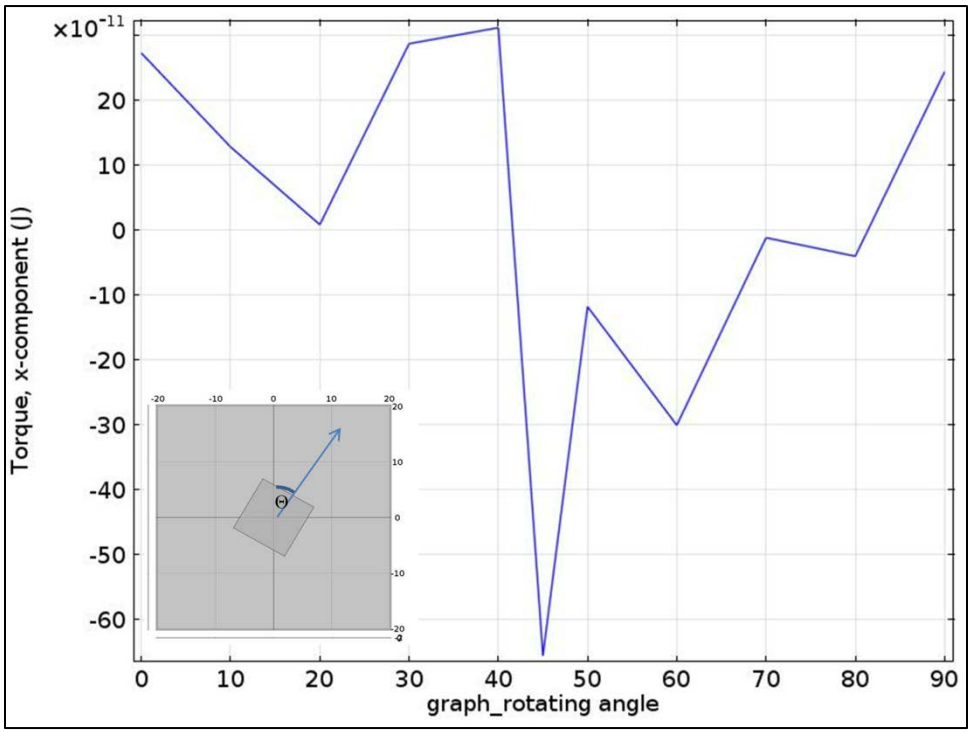


Figure 6.12 Simulated x direction torque of l=10 mm, t= 1.0 mm graphite proof mass at d =0.4952 mm (air gap) by rotating angle from 0 to 90 under N=1 magnet layer influence.

CHAPTER 7

APPLICATIONS

Magnetic levitation can be useful in several potential applications. The main focused on this chapter is to evaluate the applicability of diamagnetic levitation in possible applications. In this work, we have mainly focus on energy harvester application. The other area of applicability of diamagnetic levitation is also presented.

7.1 Energy Harvester

The bottleneck of the vibrational base energy harvesting field is lowering the frequency of the harvester down to the range of natural environmental vibrations such as vehicles, machinery, human activities and building oscillations (1-500 Hz) while lowering the size. Most MEMS resonators' resonance frequencies are in the range above 10 kHz. Application of a large and heavy proof mass is a strategy uses in lowering the resonance frequency in MEMS devices; however they have their own limitations such as maximum withstand weight, dynamic range, and fatigue in addition to dimension increase. The most widely used vibration based energy harvesters are piezoelectric and the applicability of these harvesters is still limited to applications that allow large devices. For example, a commercially available piezoelectric cantilever energy harvester has a frequency range of 26-110 Hz; however it has large dimensions of 63.5 × 6.1 × 0.6 mm which limit its small scale applications (MIDE data sheet).

As seen in *Chapter 4*, the resonance frequency of diamagnetic material has a dependence on the magnetic force. In this approximate calculation, we have neglected the magnetic influence and use the equation developed for an attached system.

Resonance frequency (f_0) is given by,

$$f_0 = \frac{1}{2\pi}\sqrt{\frac{2Eh^2}{3l^4}} \tag{7.1}$$

Spring constant (k) for cantilever is given by,

$$k = \frac{3EI}{l^3} = \frac{Ebh^3}{4l^3} \tag{7.2}$$

Resonance frequency and spring constant relate by,

$$f_0 = \frac{1}{2\pi}\sqrt{\frac{k}{m}} \tag{7.3}$$

l, b, h are length, width and thickness of the cantilever, respectively [Santuria 2002]. Young's modulus (E) of pyrolytic graphite is 25 GPa. The resonance frequency of a similar size cantilever configuration was calculated using equations 7.1, 7.2 and 7.3. As shown in Table 7.1 and Table 7.2, the resonance frequency and stiffness of a magnetic levitating system has significantly lower values in comparison to calculated values of a similarly sized cantilever actuator: approximately 3-4 orders of magnitude lower resonance frequency and three orders of magnitude lower spring constant than the mechanically attached cantilever configuration. Apart from the lower resonance frequency, there are other advantages in employing magnetic levitation proof masses compare to cantilevers. One advantage of a magnetic levitating system is the fact that the entire area of the device undergoes maximum displacement whereas in a cantilever only the area closer to the tip deflects to the maximum while keeping the attached end

deflection minimal lowering the efficiency of the harvester. Another is the ability to fine-tune the harvester for the desired frequency. The aforementioned reasons make levitating systems a better candidate to be utilized in energy harvester applications.

Table 7.1 Comparison of f_0 and k of proof masses with varied lengths when utilized in cantilever form and magnetic levitating (maglev) form. The maglev results are for the two magnet layers (N = 2) influence.

Graphite Dimensions [mm^3]	**Resonance Frequency- f_0 [Hz]**		**Spring Constant- k [N/m]**	
	Cantilever	**Maglev**	**Cantilever**	**Maglev**
9 × 9 × 1	2.5×10^6	17.25	7.7×10^4	2.18
10 × 10 × 1	2.0×10^6	16.86	6.3×10^4	2.25
11 × 11 × 1	1.7×10^6	16.45	5.2×10^4	3.01
12 × 12 × 1	1.4×10^6	16.02	4.3×10^4	2.99
13 × 13 × 1	1.2×10^6	15.66	3.7×10^4	3.53
14 × 14 × 1	1.0×10^6	15.23	3.2×10^4	4.15
15 × 15 × 1	0.9×10^6	15.18	2.8×10^4	2.99
17 × 17 × 1	0.7×10^6	14.85	2.2×10^4	3.53
19 × 19 × 1	0.5×10^6	14.45	1.7×10^4	4.15

Table 7.2 Comparison of f_0 and k of proof-masses with varied thicknesses when utilized in cantilever form and magnetic levitating form. The maglev results are for the two magnet layers (N = 2) influence.

Graphite Thickness, t [mm] (l =10 mm)	**Resonance Frequency- f_0 [Hz]**		**Spring Constant- k [N/m]**	
	Cantilever	**Maglev**	**Cantilever**	**Maglev**
0.2603	0.5×10^6	17.1	6.3×10^4	0.6
0.5046	1.0×10^6	17.0	6.3×10^4	1.2
0.6917	1.4×10^6	16.8	6.3×10^4	1.7
0.8813	1.8×10^6	16.6	6.3×10^4	2.1
1.0479	2.1×10^6	16.7	6.3×10^4	2.5

7.1.1 Electrostatic Harvester

The application of levitating suspensions to energy harvesters is particularly promising for capacitive generators. In capacitive generators, the diamagnetic levitated

proof mass can be used as the movable armature of the variable capacitor that modifies its charge when subjected to vibrations. Furthermore, an electret material is deposited on the variable capacitive arm to improve power generation. Electret generators are variable capacitors with a charged embedded dielectric layer applied to one of the electrode armatures which can generate electric power output in the presence of vibrations. The schematic representation of a proposed prototype out-of- plane diamagnetically levitated harvester is shown in Figure 7.1. In the proposed magnetically levitated capacitive generator, the movable electrode corresponded to the graphite proof mass and the fixed electrode introduced above the graphite proof mass on a rigid support; the electret layer is applied to the upper surface of the proof mass. The permanent magnets situated in the bottom plane are able to levitate the central mass made with diamagnetic material. The magnetic suspension provides low stiffness and tunability to the harvesters. High throughput can be obtained from the magnetic levitation method compared to the cantilever method as the whole area of the vibrating electrode undergoes maximum amplitude. Additionally, the comb-drive electrodes layout can be introduced around the perimeter to increase the active surface of the capacitor.

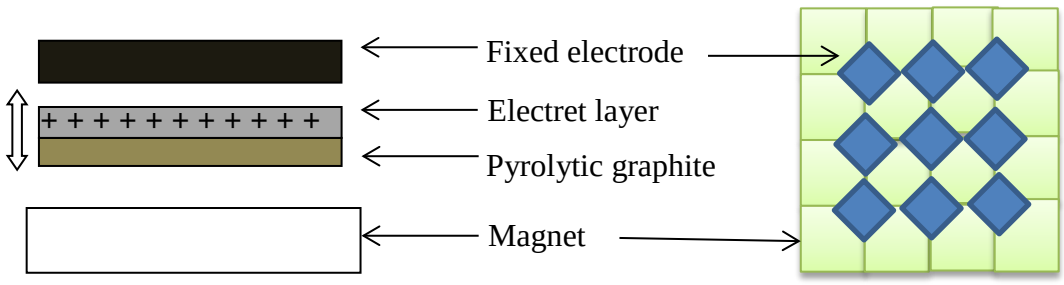


Figure 7.1 Magnetically suspended electret capacitive energy harvester based on out of plane kinematic strategy.

The harvester introduced by Edamoto (Edamoto *et al.* 2009) is based on the electret technology in which variable capacitor structural suspension support via Parylene high-aspect-ratio spring beams. This harvester was able to generate 12 μW at 21 Hz from a 300 mm^2 area of electrodes. The diamagnetic levitation suspension prototype described in this dissertation has resonance frequencies ranging from 14 to 19 Hz that provides low stiffness ranging from 2 to 5 N/m for a square shape graphite area varying between 81 and 196 mm^2 respectively (1 mm thickness). Considering the same power per cycle and per unit area of electrode verified by Edamoto, the present harvester is able to generate an output power ranging between 2.9 to 6.3 μW. As discussed earlier, the inter-digitized comb drive configuration can be introduced to the perimeter of both electrodes to increase overlapping active area of the device in order to further increase power output.

Since the power output is inversely proportional to the natural frequency of the generator for a given acceleration, it is preferable to operate at the lowest available fundamental frequency [Beiber 2006].

7.1.2 Piezoelectric and Capacitive Hybrid Harvester

A proposed hybrid power generation is expected to generate from two sources:

(1) Capacitance change due to the movement of the graphite

(2) PZT flexible cantilever bend due to the movement of the PG proof mass.

Figure 7.2 shows a schematic of a proposed prototype hybrid harvester. A PG proof mass contributes energy by the capacitive harvesting method and the anchoring cantilevers contribute by the piezoelectric means to the harvester. The PZT cantilever attachments may increase the stiffness of the system higher than non-attached systems. As the graphite is self-suspended, the PZT cantilever attachment can be made from a

flexible substrate. This strategy can reduce the effect that may cause by the attachments to the movement of the graphite. These attachments are also useful as a means to exploit the energy from a graphite capacitive generator to the outside world.

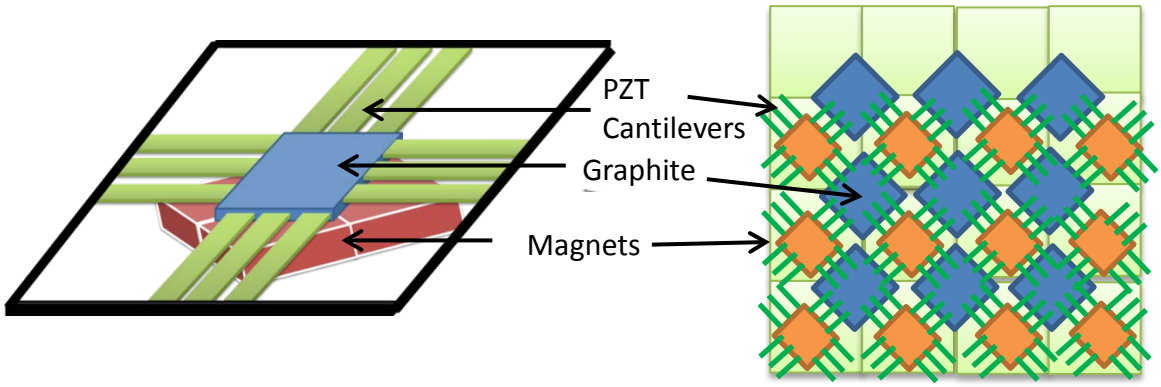


Figure 7.2 Hybrid harvester.

7.2 Other Applications

If an imperfection in the fabrication affects to the performance, the platform can be easily replaced with the right dimension platform rather than throwing out whole chip. Chip recyclability is also enabled by the levitation technique. If the levitation part is used for the sensor application, only that part can be replaced while using the other part of the device.

7.2.1 Lab on a Chip

Electrostatic micro actuators are difficult to utilize in liquid or humid medium due to the stiction problem. Also electrostatic devices have a *PULL- IN* problem [Senturia 2002]. Maglev devices are compatible with virtually all chemical environments because the magnetic field sources and manipulators can be coated with protective material. Unlike electrostatic fields, magnetic fields can penetrate chemical environments without interacting with them. Magnetic devices can be applicable from micron scale to several

centimeter scale, however electrostatic forces are more appropriate for larger scales. As the majority of substances that make up living organisms are carbon compounds, graphite which is a form of carbon is of great interest in the medical field. Pyrolytic graphite has been used in mechanical heart valves due to its blood compatibility, physical and mechanical properties and durability [Ratner 2004]. These factors make permanent magnetic levitation an attractive method in *Lab on a chip* application. Recyclability is an added advantage provided by the levitation method. It allows replacing the used levitation flat form while reusing the other part of maglev system as it is not mechanically attached. Another very attracting feature, especially for lab on chip applications is the ability for levitation parts to be manufactured separately. A major problem faced in bioMEMS device fabrication is fabricating thermal mismatch materials as it often involved with thermo sensitive polymer and organic compounds. It is difficult to realize a high temperature processing material after depositing a thermo sensitive material. Application of diamagnetic levitation can be foreseen in biomedical applications such as,

- Use as a mass sensor by functionalizing the graphite surface with materials such as antigen and used as specific target sensor.
- Use of diamagnetism of target specimen to separate, diagnosis or distinguish the material of interest.
- Use of array of micro-magnets to transport the specimen on the graphite floating stage to a subsequent analysis station. This is an alternative approach for microfluidic approaches of the *Lab on chip devices*. This method also provides contamination free and liquid free environment for

devices. The bio compatibility of graphite is a major advantage compared to the material presently use in MEMS devices.

7.2.2 Carbon Nano Tube Aligning and Graphene Devices

Koshino *et al.* has found a large diamagnetism in odd-layers of multilayer graphene due to the existence of the Dirac-like band [Koshino 2007]. Since carbon nanotubes are diamagnetic, they can be levitated on an array of patterned magnets.

CHAPTER 8

CONCLUSIONS

8.1 Summary

A prototype of the levitating system, based on pyrolytic graphite and permanent magnets in the *opposite neighboring poles* (ONP) configuration, was fabricated and employed to investigate the behavior of diamagnetic levitation. The geometrical parameters and magnetic flux density influence on static levitation height investigated by experimental methods and useful relations were drawn from the results. The same parameter influences on dynamic response were investigated and hence the magnetic stiffness and resonance frequency of levitation systems were experimentally obtained. The experimental results of dynamic levitation systems were modeled analytically similar to the small signal oscillator. FEM models were developed for NdFeB magnets and diamagnetic levitation. The validity of the models was tested using experimental results obtained for both magnets and magnetic levitation systems. The magnetic force applicable for diamagnetic levitation was established with the help of experimental and simulation results. The advantages of the magnetic levitation in comparison to mechanically attached systems were identified. A resonance frequency and spring constant of diamagnetic levitating proof masses were compared against similar sized cantilever configuration. This research work contributed to three areas of static and dynamic diamagnetic levitation: 1) Theory, 2) Experiments and 3) FEM modeling.

8.2 Mathematical Relation for Static and Dynamic Levitation

(1) There are two formulations, developed from *current model* and *charge model* are present in literature to obtain magnetic force of diamagnetic objects as discussed in *Chapter 3*. There are some examples in literature where the force expressions give entirely different forces. The magnetic force applicable for the diamagnetic levitation by permanent magnets, were established with the help of experimental and modeling data. The results showed a good agreement with the force obtained by *current model* ($\boldsymbol{F_m = \nabla(M \cdot B)}$**)** while a significant deviation from the force from *charge model* ($\boldsymbol{F_m = (M \cdot \nabla)B}$).

(2) Analytical equation for dynamic response based on Duffing equation.

8.3 Experimental Observation, Measurements and Derivation

(1) The dependence of the static levitating height on the size and the thickness of the diamagnetic levitating object.

It was observed that the levitation height has a linear dependence on the thickness of the levitating object and a nonlinear dependence on the area of the object that can be approximated to a third order polynomial equation. Further, it has been observed that when the size of the diamagnetic levitating object increases, the increment of the magnetic force acting on it from the underlying permanent magnets is larger than the increment in its gravitational force from an increase in its dimension (i.e. $\Delta F_{m,z} \geq \Delta F_g$). This necessity condition is useful in modeling to obtain the maximum levitable size of the diamagnetic object.

Also it was noted that the levitation height increases when the underlying permanent magnets are attached to a magnetizable material (e.g. Steel) as opposed to a non-magnetizable material (e.g. Plastic). Attachment to magnetizable material also allows the system to slightly increase the maximum levitable size of the object.

(2) Dependence of levitating height on the magnetic field.

When the magnetic flux density increases, the levitating height of the diamagnetic levitating object also increases.

(3) Resonance frequency characteristics of the diamagnetic levitating systems.

Just as in a mechanically attached system, the resonance frequency decreases with an increasing floating mass. However, the dependence of the resonance frequency on the magnetic field was observed in contrast to a constant resonance frequency that is seen in mechanically attached systems. This can be explained by the increase in magnetic force on the diamagnetic material when experience higher magnetic field. Hence, the magnetic virtual spring value is varying unlike a mechanical spring attachments in which the spring is constant for a give size of the object.

Also it was observed that the levitating proof mass is vibrating in phase with the driving frequency for frequencies far away from its resonance frequency. As the driving frequency of the floating mass approaches the resonance frequency, the vibrations between the floating mass and the base becomes increasingly out of phase till they are 90 degrees out of phase at the resonance frequency.

(4) Mapping of the magnetic field distribution in the space above the Opposite Neighboring Pole (ONP) configuration in order to examine the accuracy of the FEM model.

(5) Measurement of diamagnetic susceptibility (χ) of low cost commercially available pyrolytic graphite by *M-H* measurement using the *Physical Property Measurement System* (PPMS).

8.4 Finite Element Modeling

(1) Finite element model was developed for NdFeB permanent magnet using COMSOL software and experimentally verified against measurement data.

(2) Magnetic flux in the space above the ONP configuration was simulated using the framework of one magnet model and compared against the experimental data.

(3) Developed a model for diamagnetic levitation. The influence of both area variation and thickness variation of graphite were modeled in static levitation condition and compare against measurements. Additionally, the model can use to find the magnetic force generated on diamagnetic material when it placed in different heights above the magnets.

(4) Validation of $\mathrm{mg} = \nabla(\mathbf{M} \cdot \mathbf{B})$ at equilibrium levitation point in diamagnetic levitation. This method can be used to obtain the static levitation height of any magnetic system by knowing the physical and magnetic parameters.

(5) The potential minima were able to obtain by simulation for ONP configuration. This simulation can use to predict the levitating orientation for different size and shape of diamagnetic materials.

There have been various demonstrations related to diamagnetic levitation by permanent magnets that can be seen in various media publications. However, there has not been much scientific investigation done to establish/ verify relations or the parameter dependence regarding passive diamagnetic levitation. To the best of our knowledge we are the first ones to investigate the dynamic behavior of the passive levitated systems that consist of diamagnetic material and permanent magnets. The systematic investigation of size and thickness dependence of PGs in ONP configuration on static levitation height is also a novelty.

The knowledge gained from this study will be used in realizing energy harvester as a future endures of this research. There is also a scope of using fundamental relations developed in this work in other applications such as *lab on a chip* and micro-nano-manipulation system, which our group would like to subsequently explore.

REFERENCES

Akoun, G., & Yonnet , J. P. (1984). 3D analytical calculation of the forces exerted between two cuboidal magnets. *IEEE Transaction on Magnetics, Mag-20*, 1962–1964.

Alhamadi, M. A., Wang, R., & Demerdash, N. A. (1991). Vector potential 3d-finite element modeling of magnetic fields in permanent magnet devices. *IEEE trans. on Magnetics, 27*, 5016-5018.

Arkadiev , V. (1945). Hovering of a magnet over a superconductor," Vol. 9 No. 2, 1945. *Journal of Physics, 9*.

Azukizawa, T., & Morishita, M. (1989). A linear induction motor control system for a magnetically levitated carrier system. *IEEE Trans. Veh. Technology, 38*, 102–108.

Bahrdt, J. (2010). Permanent magnets including undulators and wigglers. *CERN*, 185-230. doi:arXiv:1103.1573v1.

Barrot, F. (2008). *Acceleration and Inclination Sensors Based on Magnetic Levitation. Application in the Particular Case of Structural Health Monitoring in Civil Engineering.* Lausanne (Switzerland): Dissertation, EPFL.

Berry, M. V., & Geim, A. K. (1997). Of flying frogs and levitrons. *European Journal of Physics, 18*, 307-313.

Bleuler, H. (1992). A survey of Magnetic Levitation and Magnetic Bearing types. *JSME international journal, Series III, 35*, 335-342.

Bonsor, K. (2009). *How Maglev Trains Work.* Retrieved from how stuff works: http://science.howstuffworks.com/transport/engines-equipment/maglev-train.htm

Boyer, T. H. (1987). The force on a magnetic dipole. *American Journal of Physics*(8), 688-692.

Caglar, E., & Khamesee , M. B. (2009). Design and implementation of a micromanipulation system using a magnetically levitated MEMS robot. *IEEE/ASME Trans. on Mechatronics, 14*, 434-445.

Campbell, M. (2011, October 20). *Superconducting disc locked in upside-down levitation*. (New Scientist TV) Retrieved from New Scientist Web site: http://www.newscientist.com/blogs/nstv/2011/10/levitating-disc-stays-locked-in-3d-space.html

Campbell, P. (1981). *Axial-Field Permanent Magnet Motors For Electric Vehicles.* California: University of Southern California. Retrieved from http://ntrs.nasa.gov/archive/nasa/casi.ntrs.nasa.gov/19810022491_1981022491.pdf

Campbell, P. (1982). A model of anisotropic Alnico magnets for field computation. *IEEE Transactions on Magnetics, 18*(3), 898 - 904.

Cansiz, A. (2008). Static and dynamic analysis of a diamagnetic bearing system. *Journal of Applied Physics, 103*, 034510-1-5.

Cansiz, A., & Hull, J. R. (2004). Stable Load-Carrying and Rotational Loss Characteristics of Diamagnetic Bearings. *IEEE Transaction on Magnetics, 40*, 1636-1641.

Chavanne, J., Meunier G, G., & Sabonnadihre , J. (1989). Non Linear permanent magnets modeling with the finite element method. *IEEE Trans. on Magnetics*(25), 3581-3583.

Chen, S. S., Zhu, S., & Cai, Y. (1995). On Unsteady-motion Theory of Magnetic Forces for Maglev Systems. *Journal of Sound and Vibration, 4*, 529-543.

Chetouani, H., Delinchant, B., & Reyne, G. (2007). Efficient modeling approach for optimization of a system based on passive diamagnetic levitation as a platform for bio-medical applications. *The Inter. Journal for Comp. and Math. in Elect. and Elec. Engineering, 26*(2), 345-355.

Chetouani, H., Jeandey, C., Haguet, V., Rostaing, H., Dieppedale, C., & Reyne, G. (2006). Diamagnetic levitation with permanent magnets for contactless guiding and trapping of microdroplets and particles in air and liquids. *IEEE Trans on Magnetics, 42*(10), 3557-3559.

Coey, J. M. (2011). Hard Magnetic Materials and prospectives. *IEEE Transactions on Magnetics, 47*, 4671-4681.

Cugat, O., Reyne, G., Delamare, J., & Rostaing, H. (2004). Novel magnetic micro-actuators and systems (MAGMAS) using permanent magnets. *Sensors and Actuators A, 129*(1-2), 265-269.

Cugat, O., Reyne, G., Delamare, J., & Rostaing , H. (2006). Novel magnetic micro-actuators and systems (MAGMAS). *Sensors and Actuators A, 129*, 265–269.

Damrongsak, B. (2009). *Development of a micro-machined electrostatically suspended Gyroscope.* Southampton: Dissertation, University of Southampton.

Dams, J. (2008, March). *magnetic innovations in Velocity sensing.* Retrieved from magnetic innovations: http://www.magneticinnovations.com/downloads/artikelmikronieknr32009.pdf

Dongna, S., Jung-Hyun, P., Jyoti, A., Song-Yul, C., Howard, W., & Dong-Joo, K. (2008). The design, fabrication and evaluation of a MEMS PZT cantilever with an Integrated Si proof mass for vibration energy harvesting. *J. Micromech. Microengineering*.

Earnshaw, S. (1842). On the nature of the molecular forces which regulate the constitution of the luminferous ether. *Trans. of the Cambridge Philosophical Society, 7*, 97-112.

Elbuken, C., & Khamesee MB, M. B. (2009). Design and implementation of a micromanipulation system using a magnetically levitated MEMS robot. *IEEE/ASME Trans. on Mech*(14), 343-445.

Enokizono, M., & Matsumura, K. (1997). Magnetic Field Analysis of Anisotropic Permanent Magnet Problems by. *IEEE Transactions on Magnetics, 33*, 1612-1615.

Enokizono, M., Takahashi, S., & Kiyohara, T. (2003). Magnetic field analysis of permanent magnet motor with magnetoanisotropic materials NdFeB," ., vol. 39, no. 3. *IEEE Trans. on Magnetics, 39*, 1373-1376.

Fishchbach, D. B. (1961). Diamagnetic Susceptibility of Pyrolytic Graphite. *Physical review, 123*(5), 1613-1614.

Furlani, E. P. (2001). *Permanent Magnet and Electromechanical Devices.* Academic Press.

Gao, R. W., Zhang, D. H., Li, W., Li, X. M., & Zhang, J. C. (2000). Hard magnetic property and δM(H) plot for sintered NdFeB magnet. *Journal of Magnetism and Magnetic Materials, 208*, 239-243.

Garmire, D., Choo, H., Kant, R., Govindjee, S., Sequin, C. H., Muller, R. S., & Demmel, J. (2007). Diamagnetically levitated MEMS accelerometers. *Int. Conf. on Solid-State Sensors, Actuators and Microsystems*, (pp. 1203-1206). Lyon (France).

Geim, A. (2009, January 21). Secret of levitation. (BCC, Interviewer) UK. Retrieved May 12, 2010, from http://www.youtube.com/watch?v=r7MYWfM-opk&NR=1

Geim, A. K., Simon, M. D., Boamfa, M. I., & Heflinger, L. O. (1999). Magnet levitation at your fingertips. *Nature, 400*, 323–324.

Goll, D., & Kronmüller, H. (2000). High-performance permanent magnets. *Naturwissenschaften, 87*, 423–438.

Griffiths, D. J. (1999). *Introduction to Electrodynamics.* New Jersey: Prentice-Hall Inc.

Hinchliffe, A., & Munn, R. W. (1985). *Molecular Electromagnetism.* Manchester, UK: John Wiley & Sons Ltd.

High field magnetic laboratory. (2009). Retrieved from Radboud University Nijmegen: http://www.ru.nl/hfml/research/levitation/diamagnetic/

Hoque, M., Takasaki, M., Ishino, Y., & Mizuno, T. (2006). Development of a Three-Axis Active Vibration Isolator Using Zero-Power Control. *IEEE/ASME Transacations on Mechatronics, 11*, 462-470.

Houlihan, R., & Kraft, M. (2002). Modelling of an accelerometer based on a levitated proof mass. *Journal of Micromechanics and Microengineering*, 495-503.

Inoue, T., & Ishida, Y. (2008). Nonlinear forced oscillation in a magnetically levitated system: the effect of the time delay of the electromagnetic force. *Nonlinear Dynamics, 52*, 103–113.

Ishigaki, Y., Ueda, H., & Agatsuma, K. (2009). Accurate Position Control of Active Magnetic Levitation Using Sphere-Shaped HTS Bulk for Inertial Nuclear Fusion. *IEEE Transaction on Applied Superconductivity, 19.*

Jackson, J. D. (1977). *The Nature of Intrinsic Magnetic Dipole Moments.* Geneva: CERN European Organization of Nuclear Research.

Jayawant, B. V. (1988). Review Lecture. Electromagnetic Suspension and Levitation Techniques“, Vol. (Apr. 8, 1988), pp. *Mathematical and Physical Sciences. 416*, pp. 245-320. London: Proceedings of the Royal Society of London. Series A.

Jones, W. (1980). Earnshaw‘s theorem and the stability of matter. *Eur. J. Physics*, l 85-188.

Judy, J. W. (2001). Microelectromechanical systems (MEMS): fabrication, design and applications. *J. Smart Materials, 10*, 1115–1134.

Katter, M. (2005). Angular Dependence of the Demagnetization Stability of Sintered Nd–Fe–B Magnets. *IEEE Transactions on Magnetics, 41*, 1-3.

Kauffmann, P., Dempsey, N., O’Brien, D., Combe, S., Schaack, B., Haguet, V., & Reyne, G. (2010). Diamagnetic trapping of cells above micro-magnets. *IEEE Conference on Electromagnetic Field Computation (CEFC).* Chicago ,United States: IEEE.

Koshino, M. (2011). *Orbital Magnetism of Graphenes.* Open access publisher.

Koshino, M., & Ando, T. (2007). Diamagnetic response of graphene multilayers. *Physica E*.

Kustler, G. (2007). Diamagnetic Levitation- Historical Milestones. *Rev. Roum. Sci. Techn. – Électrotechn. et Énerg., 52*, 265–282.

Lee, H.-W., Kim, K.-C., & Lee, J. (2006). Review of Maglev Train Technologies. *IEEE Transaction on Magnetics, 42*, 1917 - 1925 .

Lin, u.-M., Valdes-Garcia, A., Han, S.-J., Farmer, D. B., Meric, I., & Sun, Y. (2011). Wafer-Scale Graphene Integrated Circuit. *Science, 332*, 1294-1297.

Livingston, J. D. (2011). *Rising Force: The Magic of Magnetic Levitation.* Harvard University Press.

Lyuksyutov, F., Naugle, D. G., & Rathnayaka, K. D. (2004). On-chip manipulation of levitated femtodroplets. *Applied Physics Letters, 85*, 1817-1819.

Magnetics, A. (2012, January 14). *Neodymium Literature*. Retrieved from Arnold Magnetics : http://www.arnoldmagnetics.com/Neodymium_Literature.aspx.

Mann, B. P., & Sims, N. D. (2009). Energy harvesting from the nonlinear oscillations of magnetic levitation. *Journal of Sound and Vibration, 319*, 515-530.

McCaig, M., & Clegg, A. G. (1987). *Permanent Magnets in Theory and Practice", second edition, 1987.* (2 ed.). John Wiley & Sons.

McClure, J. W. (1956). Diamagnetism of Graphite. *Physical Review, 104*, 666-670.

Nakahata , Y., Todaka, T., & Enokizono, M. (2011). Magnetization process simulation of NdFeB magnets taking the demagnetization phenomenon Into Account. *IEEE Trans. on Magnetics, 47*, 1102-1105.

Nakahata, Y., Takashi, T., & Enokizono, M. (2007). Development of three-dimensional VMSW method. *Journal of Magnetism and Magnetic Materials, 310*(2), 2644-2646.

Niarchos, D. (2003). Magnetic MEMS: key issues and some applications. *Sensor and actuators A*, 166- 173.

Pelrine, R. E. (1995, March 7). *Patent No. US5396136.* United States.

Pelrine, R. E. (2004). Diamagnetic Levitation: Known since the 1930s, a simple technique for suspending objects magnetically is just now finding practical application. *American Scientist, 92*, 428-435.

Pelrine, R. E., & Heim, J. R. (2002, July 11). *Patent No. Patent US2002/0090287.* United States.

Profijt, H. B., Pigot, C., Reyne, G., Grechishki, R. M., & Cugat, O. (2009). Stable diamagnetic self-levitation of a micro-magnet by improvement of its magnetic gradients. *Journal of Magnetism and Magnetic Materials, 321*, 259–262.

Ratner, B. D. (2004). *Biomaterials Science: An Introduction to Materials in Medicine.* Elsevier Academic Press.

Roundy, S., & Wright , P. K. (2004). A piezoelectric vibration based generator for wireless electronics. *Smart Materials and Structures, 13*, 1131–1142.

Sagawa, M., Matsuura , Y., & Egawa. (1984). New Material for Permanent Magnets on a Base of Nd and Fe. *Journal of Applied Physics, 55*(6), 2083-2087.

Savin, S. F., D'yachkov, L. G., Vasiliev, M. M., Petrov, O. F., & Fortov, V. E. (2009). Clusters of charged diamagnetic particles levitating in non-uniform magnetic field", EPL, 88 64002, 2009. *epl, 88*, 64002-p1-p6. doi:10.1209/0295-5075/88/64002

Schenck, J. F. (1992). Health and physiological effects of human exposure to whole-body four-tesla magnetic fields. *MRI Ann. Acadamy of Science*, 285–301.

Schmidt, R. (2001, March 1). *Diamagnetic levitation: The invisible force.* Retrieved from Sensors: http://www.sensorsmag.com/articles/0301/30/main.shtml

Sci/Tech. (1998, September 30). *Rollercoaster ride into space*. Retrieved July 13, 2010, from http://news.bbc.co.uk/: http://news.bbc.co.uk/2/hi/science/nature/183377.stm

Seager, S. L., & Slabough, M. R. (2010). *Chemistry for today: General , Organic and Biochemistry.* NJ, USA: Cole Pub Co.

Senturia, S. (2002). *Microsystem Design.* Kluwer Academic Publishers.

Shen, D., Jung-Hyun, P., Jyoti , A., Song-Yul, C., Howard, W., & Dong-Joo, K. (2008). "The design, fabrication and evaluation of a MEMS PZT cantilever with an Integrated Si proof mass for vibration energy harvesting. *J. Micromech. Microeng*, 055017-1-7.

Simon, M. D. (2001). Diamagnetically stabilized magnet levitation. *American Journal of Physics, 69*(6), 702-713.

Simon, M. D., & Geim, A. K. (2000). Diamagnetic levitation:Flying frog and floating magnets. *Journal of Applied Physics, 87*, 6200-6204.

Stohr, J., & Siegmann, H. C. (2006). *Magnetism :from Fundamentals to Nanoscale Dynamics.* Springer. Retrieved from http://www.scribd.com/doc/62903500/Magnetism-from-Fundamentals-to-Nanoscale-Dynamics.

Stoner, E. C., & Wohlfarth, E. P. (1948). A Mechanism of magnetic hysteresis in heterogeneous alloys. *Phil. Trans. of the Royal Society of LondonMath. and Phy. Sci., 240,* 599-642.

Takagi, T., Tani, J., Matsubara, Y., & Mogi, I. (1995). Dynamic behavior of fusion structural components under strong magnetic fields. *Fusion Engineering and Design*, 481-489.

Takashi, M. (2005). Our manned maglev system attains maximum speed record of 581 km/h. *railway Technology Avelanche,* p. 41.

Tanaka, Y., & Horie, T. (2001). Characteristics of the forced vibration with magnetic damping", International. *Journal of Applied Electromagnetics and Mechanics, 13*(1-4), 45-51.

Teranishi, Y., Ueda, H., Tsuda , M., & Ishiyama, A. (2002). Static and Dynamic Characteristics in Levitating X–Y Transporter Using HTS Bulks. *Ieee Transactions On Applied Superconductivity, 12*, 911-914.

Transrapid. (2004, 12 29). Retrieved from Wikipedia: http://en.wikipedia.org/wiki/File:Shanghai_Transrapid_002.jpg.

Verma, S., Kim, W.-j., & Gu, J. (2004). Six axis nano positioning device with precision magnetic levitation technology. *IEEE/ASME Transaction on Mechatronics, 9*, 384-391.

Vische, D., & Bleuler, H. (1993). Self-sensing Active Magnetic Levitation. *IEEE Transactions on Magnetics, 29*, 1276-1281.

Waldron, R. (1966). Diamagnetic Levitation Using Pyrolytic Graphite. *Review. Of Scientific Instruments, 37*, 29-35.

Walther, A., Marcoux, C., Desloges, B., & Grechish, R. (2009). Micro-patterning of NdFeB and SmCo magnet films for integration into Micro-Electro-Mechanical-Systems. *Journal of Magnetism and Magnetic Materials,* 590–594.

Wang, C., Chang, L. H., Chang, C. H., Lin, M. C., Hwang, C. S., & Chen, J. R. (1998). Effects of magnets with non-unit magnetic permeability on an elliptically polarizing undulator. *Journal of Synchrotron Radiation, 5*, 478-480.

Wu, X., Chen, W., Zhao, X., & Zhang, W. (2006). Development of a mechanicahined rotating gyroscope with electromechanically levitated rotor. *Journal of Mechanics and Microengineering, 16*, 1993-1999.

Xiao-fan, G., Yong, Y., & Xiao-jing, ,. Z. (2004). Analytic expression of magnetic field distribution of rectangular permanent magnets. *Applied Mathematics and Mechanics, 25*(3), 297-306.

Yates, R., Williams, C., Shearwood, C., & Mellor, P. (1996). Levitation of a micromachined rotor for application in a rotating gyroscope. *Silicon Fabricated Inertial Instruments . 2882*, pp. 1845 - 1846 . London, UK: IEEE Explore.

Yousefi, M., Rouhollahi, A., Hadi , M., & Mohammad, F. (2006). Electrochemical performance of a pyrolytic carbon film with the anisotropic microstructure. *Proceeding of the IEEE internationa* (pp. 627-630). Zhuhai, China: IEEE.

Zhang, W., Chen, W., Zhao, X., Huang , X., Shao,, S., & Wu, X. (2006). The study of an electromagnetic levitating micromotor for application in a rotating gyroscope. *Sensor and actuators A, 132*, 651-657.

Zhu, Z. Q., Howe, D., & Chan, C. C. (2002). Improved Analytical Model for Predicting the Magnetic Field Distribution in Brushless Per.-Magnet Machines. *IEEE Trans. on Magnetic, 38*, 229 - 238.

Zienkiewicz, O. C., Emson, C., & Bettess, P. (1983). A novel boundary infinite element. *Int. J. Num. Meth. Engineering*(19), 393-404.

Zienkiewicz, O. C., Taylor, R. L., & Zhu, J. Z. (2005). *The Finite Element Method: Its Basis and Fundamentals.* SAN FRANCISCO, USA: Elsevier Butterworth-Heinemann.

APPENDICES

Appendix A: List of Symbols and Acronyms

μ_0	Permeability of free space
μ_{perp}	Relative permeability perpendicular to magnetic easy axis
μ_r	Relative permeability
μ_{par}	Relative permeability parallel to magnetic easy axis
ε_r	Permittivity of the medium
$F_{m,z}$	Magnetic force in z direction
f_0	Resonance frequency
k_m	Magnetic stiffness
$\boldsymbol{F_c}$	Damping force
$\boldsymbol{F_g}$	Gravitational force
$\boldsymbol{F_i}$	Magnetic force on a magnetic dipole
$\boldsymbol{F_m}$	Magnetic force
$\boldsymbol{F_m}$	Total force
$\boldsymbol{F_s}$	Force of the shaker
ε_0	Permittivity of the free space
μ	Permeability
$\boldsymbol{B}$	Magnetic flux density
B_z	Magnetic flux density in z direction
C	Capacitance
c_m	Magnetic damping
c_v	Viscous damping
d_a	Air gap
Dv	Differential volume
h	Height
H_c	Coercivity
H_{ci}	Intrinsic coercivity
H_{cb}	Coercivity of induced magnetic field
J_m	Volume current density
$\boldsymbol{M}$	Magnetic dipole moment or dipole
M	Mass
Mg	Weight of the PG proof mass
$\boldsymbol{R}$	Position vector
t_m	Thickness of the magnets
W	Magnet width
x, y, z	Co-ordinate system
Θ	Angle of rotation
Φ	Magnetic flux
X	Volume susceptibility
Ω	Angular frequency
A	Amplitude
Br	Remanence
E	Young modulus

Appendix A: (Continued)

$\boldsymbol{H}$	Magnetic field
N	Number of magnet layers
U	Potential energy
V_m	Scalar potential
d	Distance from the magnets to the PG
f	Frequency
g	Gravitational acceleration
k	Spring constant
l	Length of the graphite
t	Thickness of the pyrolytic graphite
$\boldsymbol{M}$	Magnetization
γ	Bandwidth
ζ	Damping ratio
ψ	Scalar potential at a point
DOF	Degree of freedom
FEM	Finite element modeling
CM	Center of mass
NdFeB	Neodymium Iron Boron
ONP	Opposite neighboring poles
PG	Pyrolytic graphite
PM	Permanent magnet

Appendix B: Maglev Trains

There are three main categories of maglev train systems found in use: Electromagnetic Suspension (EMS) in which levitation is accomplished based on the magnetic attraction force between a guide-way and electromagnets, Electro-dynamic Suspension (EDS) uses repulsive force for the levitation between electrically powered railway and permanent magnet or super conductor attached apartments. In Hybrid Electromagnetic Suspension (HEMS), permanent magnets are partly used to reduce electric power consumption. The Maglev train offers numerous advantages over the conventional wheel-on-rail system: 1) speed is much higher (approx. 5 times) than other ground transportation system 2) elimination of wheel and track wear providing a consequent reduction in maintenance costs, 3) owing to its guide-way, a Maglev train will never be derailed, 4) the absence of wheels removes much noise and vibration, 5) accomplishes acceleration and deceleration quickly [Lee 2006]. There are draw backs to these system such as both propulsion and braking forces should provide by electromagnetic interaction and it consume high power, difficulty in switching or branching and not suitable for freight. Also the effect on human and their health and safety is still a controversy.

Appendix C: Sintered Magnets

The Sumitomo Company in Japan developed the fabrication process for sintered rare earth magnets in 1984 [Sagawa 1984]. The process starts with mixing various ingredients (Nd, Fe and B) according to the right ratio under argon gas atmosphere, and then melting to cast it into macroscopic pieces. The pieces are crushed in a nitrogen atmosphere and then milled in several steps down to particle sizes of a few micrometers (~ 3μm). The domains of highly reactive powders are aligned in the presence of a high field and pressed. This makes a magnet made in this method anisotropic. The pressed pieces are sintered at temperatures of around 850°C, which melts the surfaces of the grains (liquid phase sintering) [Sagawa 1984]. The quality of the magnet depends on the direction of pressing against the applied magnetic field. Sintered magnets are either isostatically pressed (IP), transversally pressed (TP), or axially pressed (AP). The highest remanence is achieved with isostatic pressing.

Appendix D: Bonded Magnets

In 1984 General Motors developed the bonded magnet technique. The rapid quenching or melt spinning method, commonly referred to as Magnequench, is used to make the bonded method magnets. In this process the NdFeB alloy is melted and forced under argon (Ar) pressure through a small orifice onto the surface of a water-cooled revolving metal wheel. This yields rapidly quenched thin ribbons later milled and annealed and then blended with an epoxy resin. The compound is pressed into a desired shape and then oven cured. The finished magnets are isotropic due to the random orientation of the NdFeB grains within the platelets. There are three grades of Magnequench known as MQ I, MQ II, and MQ III. MQ III has the highest energy product among the three grades [Fulani 2001].

Appendix E: Copyright and Permissions

E.1 Permissions for Figure 2.1

---------- Forwarded message ----------
From: **Mia Evans**
Date: Wednesday, November 21, 2012
Subject: Request to use image for dissertation
To: "Smith, Andrew M." <dsmith@usf.edu>

Permission is kindly granted. This permission is for one-time educational use only. If you need further assistance please feel free to contact me.

Mia B. Evans
Coordinator of Editorial Operations

-----Original Message-----
From: Drew Smith [mailto:dsmith@usf.edu]
Sent: Tuesday, November 20, 2012 4:37 PM
To: Mia Evans
Subject: Request to use image for dissertation

I am writing on behalf of a doctoral student, Chamila Siyambalapitiya, at the University of South Florida.

As part of her non-commercial dissertation, she would like to use the image shown as Figure 5 on the following page:

http://www.americanscientist.org/issues/issue.aspx?id=941&y=2004&no=5

Regards,

Drew Smith
Assistant Librarian
Academic Services, USF Tampa Library
dsmith@usf.edu
813-974-3492

Appendix E: (Continued)

---------- Forwarded message ----------
From: **lijnis**
Date: Thursday, November 22, 2012
Subject: Request to use image for dissertation
To: "Smith, Andrew M." <dsmith@usf.edu>
Cc: HFML Secretariaat <hfmlsecr@science.ru.nl>

Dear Drew Smith,

You can use the levitating frog photo.
As credits you should use: "High Field Magnet Laboratory, Radboud University, Nijmegen, the Netherlands".

There is a high resolution version of the photo available for download at:
ftp://ftp.science.ru.nl/pub/hfml/photos/levitation-HR/frog.tif

Regards,

Lijnis Nelemans
High Field Magnet Laboratory
Radboud University Nijmegen
the Netherlands

-------- Original Message --------
Subject: Request to use image for dissertation
Date: Tue, 20 Nov 2012 16:38:55 -0500
From: Drew Smith <dsmith@usf.edu>
To:<hfmlsecr@science.ru.nl>
References:<CALSepZZnbQWgrt3KRAijK5NL0-r-oSgcYo83891dFyg1TAzmZg@mail.gmail.com>

I am writing on behalf of a doctoral student, Chamila Siyambalapitiya,
at the University of South Florida.

As part of her non-commercial dissertation, she would like to use the
image shown as captioned "Why Frogs?" on the following page:

http://www.ru.nl/hfml/research/levitation/diamagnetic/

Regards,

Drew Smith
Assistant Librarian
Academic Services, USF Tampa Library
dsmith@usf.edu
813-974-3492

...